ABSTRACT

Title of thesis: MECHANISMS OF VORTEX-INDUCED PARTICLE TRANSPORT FROM A MOBILE BED BELOW A HOVERING ROTOR

Jaime Reel, Master of Science, 2014

Thesis directed by: Professor J. Gordon Leishman
Department of Aerospace Engineering

A study has been conducted to examine rotor-generated blade tip vortices that pass near to a ground plane covered with mobile sediment particles and to explore whether they induce a pressure field that may affect the problem of rotor-induced dust fields. It was hypothesized that fluctuating pressures lower than ambient at the ground could potentially affect the processes of sediment particle mobilization and uplift into the flow. To investigate the relationship between the vortex wake characteristics and the motion of the mobilized sediment particles, single-phase and dual-phase (particle) flow experiments were conducted using a small laboratory-scale rotor hovering overing a ground plane. Time-resolved particle image velocimetry was used to quantify the flow velocities in the rotor wake and near the ground plane, and particle tracking velocimetry was used to quantify the particle velocities. Measurements were also made of the unsteady pressure over the ground

plane using pressure transducers that were sensitive enough to resolve the small induced pressures. Time-histories of the measured responses showed significant pressure fluctuations occurred before, during, and after the rotor wake impinged upon the ground. While it was not possible to separate out the effects of pressure forces from other forces acting on the particles, the present work has shown good evidence of vortex-induced pressure effects on the particles in that particle trajectories significantly deviated from the directions of the surrounding flow in the immediate presence of the vortices. The characteristics of the pressure responses produced at the ground by vortices passing nearby was also predicted using a model based on unsteady potential flow theory, and was used to help interpret the measurements. The vortex strength (circulation), height of the vortex above the ground, and the vortex convection velocity, were all shown to affect the pressures at the ground and were likely to affect particle motion.

Mechanisms of Vortex-Induced Particle Transport from a Mobile Bed below a Hovering Rotor

by

Jaime Lynn Reel

Thesis submitted to the Faculty of the Graduate School of the
University of Maryland, College Park in partial fulfillment
of the requirements for the degree of
Master of Science
2014

Advisory Committee:
Professor J. Gordon Leishman, Chair/Advisor
Associate Professor James Baeder
Professor Roberto Celi
Senior Research Scientist Nail Gumerov

Dedication

I proudly dedicate this degree to my whole family, who inspired me to prove that tobacco farmers and oilfield workers can be rocket scientists too.

Acknowledgments

I chose to study rotorcraft at the University of Maryland because I wanted to be a part of their prestigious Aerospace Engineering Graduate Program, and because I specifically wanted to work under the guidance of Dr. J. Gordon Leishman. That dream was not immediately realized, but through hard work, perserverance, and a little help, I was able to achieve this and many other goals along the way. I want to sincerely thank Dr. Leishman for giving me the opportunity to prove my worthiness.

I would also like to thank Dr. James Baeder, Dr. Roberto Celi, and Dr. Nail Gumerov for their contributions and for serving as members of my thesis committee.

A special thanks goes to the members of the Aerospace Department staff. I give thanks to Erika Aparakakankanange for believing in me and helping me to find my way, and to Thomas Hurst for pushing me, supporting me, and regularly feeding me homemade soup with a side of stand-up comedy.

Perhaps the best part of this whole experience was the amazing friends I've made. It was so much fun to work alongside Nate Doane, Ajay Baharani, Monica Syal, and David Mayo. Thanks to Natalie Jones, Andrew Lind, and Mark Glucksman-Glaser for always exchanging cat tales with me, and thanks to my kitties themselves, Lexi Boots and Kai-Kai Bug, for spending the endless allnighters by my side! Friend is not even a strong enough word for some. Anish Sydney and Joseph Milluzzo have been more like brothers to me. While I thoroughly enjoyed the company of all Team Leishman members, past and present, the most deepest sense of gratitude that I can possibly express goes to Bharath Govindarajan. He has been an unbelievably patient and selfless

mentor to me throughout. I learned so much from him, not just about engineering, but about life, outlook, and moral integrity. As I always tell Bharath, I want to be just like him when I grow up.

Last but not least, I have to thank my loving family. I owe everything to my parents, Bob and Barbara Reel, who worked so hard to make sure they could give me a better education than they received. They have always supported me and my varied interests unconditionally. I would be nothing without them. My brother, Bobby, has driven me to be the very best person I can be, because I know he is watching. I hope I have been a good role model for him. I just wish I could share this acheivement with the family members to whom I have already said goodbye, especially my much-loved Grandma Burnem who passed this year. They raised me to be strong and independent, but I know I couldn't have done this alone. To all who helped me get here, I do not take your sacrifices lightly, and I only hope I've made you proud.

Table of Contents

List of Tables ix

List of Figures ix

Nomenclature xvi

1 Introduction 1

1.1 The Problem of Brownout 1

1.2 The Physics of Brownout 6

1.2.1 Representative Rotor Flows in Ground Effect Operation 7

1.2.2 Sediment Particle Dynamics 10

1.3 Prior Work 14

1.3.1 Sediment Entrainment Mechanisms 15

1.3.2 Vortex-Wall Fluid Dynamic Interactions 16

1.3.3 The Aeolian Sciences 18

1.3.4 Models of Particle Motion 20

1.3.5 Rotor Wake/Surface Interactions 23

1.4 Objectives of the Present Work 26

1.5 Organization of Thesis 27

2 Description of the Experiments 28

2.1 Experimental Setup 28

2.1.1 Description of the Rotor 29
2.1.2 Flow Measurements 30
2.1.3 Pressure Measurements on the Ground Plane 33
2.2 Experimental Techniques 37
2.2.1 Time-Resolved Flow Visualization (TR-FV) 37
2.2.2 Pressures on the Ground Plane 37
2.2.3 Time-Resolved Particle Image Velocimetry (TR-PIV) 38
2.2.4 Particle Tracking Velocimetry (PTV) 41
2.3 Region of Interest (ROI) 43
2.4 Rotor Operating Conditions 44
2.5 Technical Challenges 48
2.5.1 Flow Visualization (FV) 48
2.5.2 Surface Pressures on Ground Plane 48
2.5.3 Particle Image Velocimetry (PIV) 50
2.5.4 Particle Tracking Velocimetry (PTV) 52
2.6 Error and Uncertainties 53
2.6.1 Particle Image Velocimetry (PIV) 54
2.6.2 Particle Tracking Velocimetry (PTV) 56
2.7 Summary 56

3 Results 58

3.1 Rotor Wake Behavior 58

3.2 Identifying Event Signatures 63
3.3 Description of the Condensed Test Matrix 68
3.4 Flow Visualization Results 71
3.5 Unsteady Pressure Measurements 74
3.6 Understanding the Pressure Responses 80
3.6.1 Time-Averaged Pressure Responses 80
3.6.2 Blade Passage Effect 84
3.6.3 Effect of Vortex Passage on Ground Plane Pressure 86
3.7 Method of Synchronizing Data 96
3.7.1 Vortex Frequency 98
3.7.2 Vortex Tracking 98
3.7.3 Synchronization of the Measurements 99
3.8 Analysis of Measured Results 104
3.8.1 Particle Concentrations Near Vortices 104
3.8.2 Fluctuating Velocity and Pressure Effects on Particle Uplift 110
3.8.3 Particle Fluxes 119
3.8.4 Influence of the Vortices on Particles 123
3.8.5 Particle/Flow Deviations 127
3.8.6 Scaling the Effects 132
3.9 Summary 135

4 Conclusions 136

4.1 Summary 136

4.2 Specific Conclusions 137

4.3 Suggestions for Future Work 140

Appendix A: The Unsteady Flow Model 143

A.1 Derivation of Unsteady Flow Model 143

A.1.1 Potential Field – Uniform Velocity 144

A.1.2 Potential Field – Vortex 144

A.1.3 Net Velocity and Potential Field 146

A.1.4 Evaluation of Ground Pressure 147

References 148

List of Tables

3.1 Table summarizing the rotor operating conditions for the condensed test matrix. . . 74

3.2 Table summarizing the inputs and results for the problem scaling analysis. 134

List of Figures

1.1 A helicopter encountering brownout conditions during a landing. (Photo is courtesy of Optical Air Data Systems LLC.) 2

1.2 A landing helicopter with the formation of a more favorable ring or toroidal shaped dust cloud that forms away from the immediate landing zone. 5

1.3 Schematic showing the different modes of sediment particle motion and the resulting dust field generated by the rotor wake from a helicopter hovering over a surface covered with loose material. 7

1.4 Example of the downstream wake of a rotor operating out of ground effect. 9

1.5 Example of the downstream wake of a rotor operating in ground effect. 9

1.6 Schematic showing the forces and the pressure distribution acting on a stationary particle on a sediment bed. 11

1.7 Schematic of the forces and pressure distribution acting on an airborne particle. . . 12

1.8 Schematic illustrating the various sediment transport mechanisms that may occur below a helicopter rotor when it is operating over a mobile sediment bed. 17

1.9 The relationship between threshold friction velocity and particle diameter. 23

2.1 The small-scale rotor with its mounting, motor, and configurable teetering hub. . . 30
2.2 Schematic showing the overall experimental setup. 31
2.3 Schematic of the orientation of the system components used for the flow measurements. 32
2.4 Schematic of the sealed plenum housing the sensors, which was on the back of the ground plane. 34
2.5 Schematic of the pin in/out and the Wheatstone bridge nature of the pressure sensors. 35
2.6 Diagram of the circuit used to remove DC voltage offset from the pressure transducer output signals. 35
2.7 Schematic of the pressure measurement system. 36
2.8 Visual representation of the algorithm used in the PIV analysis. 39
2.9 Visual representation of particle identification in the PTV. 42
2.10 Schematic showing the region of interest (ROI) for all experiments, as well as the locations of the pressure measurements. 43
2.11 Schematic comparing the general nature of the one-bladed and two-bladed rotor wake flow fields. 44
2.12 The inverted rotor orientation and grounded aluminum shroud that was used to minimize noise from the electric motor while recording the pressure measurements. 49
2.13 Methods to minimize surface reflections of the laser sheet at the ground plane. . . . 50
2.14 FV image showing the deflation and dune regions that can form on the sediment bed after the rotor has been in operation for some time. 51

2.15 Processed image showing the "holes" that can result from separation of the particle (dispersed) phase from the carrier phase. 52

2.16 Dual-phase FV image showing image over-saturation caused by too many uplifted and suspended particles. 53

3.1 Schematic showing the behavior of the rotor wake as it impinges on the ground plane. 59

3.2 FV images used to define the location of the three vortex impingement zones for the one-bladed rotor while operating at various conditions, including three heights above the ground plane and at two rotational frequencies. 61

3.3 FV images used to define the location of the three vortex impingement zones for the two-bladed rotor while operating at various conditions, including three heights above the ground plane and at two rotational frequencies. 62

3.4 A FV image defining the locations of the three phases of vortex impingement. The phase-averaged responses show the characteristics of their corresponding pressure signatures. One-bladed rotor operating at 0.5 z/R and 130 Hz. 65

3.5 A FV image defining the location of the three phases of vortex impingement. The phase-averaged pressure responses show the characteristics of their corresponding pressure signatures. One-bladed rotor operating at 1.0 z/R and 130 Hz. 67

3.6 A FV image defining the location of the three phases of vortex impingement. The phase-averaged pressure responses show the characteristics of their corresponding pressure signatures. One-bladed rotor operating at 1.5 z/R and 130 Hz. 69

3.7 Single-phase FV images for z/R = 1.0 and 130 Hz. 72

3.8 Dual-phase FV images for z/R = 1.0 and 130 Hz. 73

3.9 Carpet plots of the time-history of the ground surface pressure. One-bladed and two-bladed rotors operating at 1.0 r/R and 130 Hz. 76

3.10 Detailed view of ground surface pressure carpet plots. One-bladed and two-bladed rotors operating at 1.0 r/R and 130 Hz. 77

3.11 Contour plots of the time-history of the ground surface pressure. One-bladed and two-bladed rotors operating at 1.0 r/R and 130 Hz. 78

3.12 Detailed view of the ground surface pressure contour plots. One-bladed and two-bladed rotors operating at 1.0 r/R and 130 Hz. 79

3.13 Schematic of the simplified model used for momentum theory analysis of the rotor flow field. 81

3.14 Estimates of the velocity and pressure distribution along the ground below a hovering rotor obtained using momentum theory. 82

3.15 Plots of the mean $C_p{}'$ values along the ground and the variation from the mean calculated from the pressure measurements. 83

3.16 Contour plots of the time-histories of the pressure measurements showing evidence of the blade passage effect. 85

3.17 Schematic of the unsteady flow model. 87

3.18 Predicted results from the unsteady flow model showing a vortex convecting parallel to the ground. 88

3.19 Determining values for the unsteady flow model inputs from the experimental data. 89

3.20 The pressure predictions from the unsteady flow model for three induced velocities. 90

3.21 Pressure predictions from the unsteady flow model for three induced velocities and two vortex spacings. 92

3.22 Outlining the sensitivity of the pressure response to vortex height above the ground. 93

3.23 Outlining the sensitivity of the pressure response to vortex convection speed along the ground. 94

3.24 Outlining the sensitivity of the pressure response to vortex strength. 95

3.25 Each of the FV images show a vortex near the sensor at 1.47 r/R, and the pressure response for that sensor measured a vortex signature near each of the corresponding wake ages. 97

3.26 The FV images track the progress of a single vortex as it passes three sensor locations. 100

3.27 Locating a datum within the pressure responses that contains signatures corresponding in phase to the flow events, such as blade or vortex passage, as observed in the one-bladed reference FV image. 101

3.28 Locating a datum within the pressure responses that contains signatures corresponding in phase to the flow events, such as blade or vortex passage, as observed in the two-bladed reference FV image. 103

3.29 Maps of particle concentration for the one-bladed rotor at 1.0 z/R and 130 Hz. . . . 106

3.30 Detailed maps of particle concentration for the one-bladed rotor at 1.0 z/R and 130 Hz. 107

3.31 Maps of particle concentration for the two-bladed rotor at 1.0 z/R and 130 Hz. . . . 108

3.32 Detailed maps of particle concentration for the two-bladed rotor at $1.0z/R$ and 130 Hz. 109

3.33 Explanation of the method used to extract the time-history of the velocity components for given point in the flow field. 111

3.34 Explanation of the method used to extract the time-history of sediment height above the ground for a given radial location. 112

3.35 Time-history of v- and u-velocities for one-bladed rotor. 113

3.36 Time-history of v- and u-velocities for two-bladed rotor. 114

3.37 Time-history of v-velocity and particle uplift for one-bladed rotor. 115

3.38 Time-history of v-velocity and particle uplift for two-bladed rotor. 116

3.39 Time-history of v-velocity and pressure at 1.51 r/R for one-bladed rotor. 117

3.40 Time-history of v-velocity and pressure at 1.51 r/R for two-bladed rotor. 118

3.41 The total particle flux in the r-direction and the z-direction for the one-bladed rotor. 120

3.42 The total particle flux in the r-direction and the z-direction for the two-bladed rotor. 120

3.43 The phase-averaged particle flux for in the r-direction and the z-direction for the one-bladed rotor. 121

3.44 The phase-averaged particle flux for in the r-direction and the z-direction for the two-bladed rotor. 122

3.45 Method of comparing the proximity of vortices to the ground and the height of uplifted sediment particles beneath each vortex. 124

3.46 The relationship between the proximity of vortices to the ground and the height of uplifted sediment beneath each vortex. 125
3.47 Instantaneous tip vortex locations grouped by wake age. 126
3.48 Distribution of particles over the range of deviation angles for each rotor. 128
3.49 Examples of large particle/flow deviations for the one-bladed rotor. 129
3.50 Examples of large particle/flow deviations for the two-bladed rotor. 130
3.51 Schematic of a particle assuming constant pressure distributions over its top and bottom surfaces and considering only the effects of pressure and gravitation forces. 133

A.1 Schematic depicting the potential flow model based on a train of vortices. 144
A.2 Schematic depicting a vortex along with the reference coordinate system. 145

Nomenclature

A	Rotor disk area, m^2
A_p	Cross-sectional area of particle, m^2
c	Blade chord, m
$C_p{}'$	Nondimensional pressure coefficient, $= 100\,(P - P_\infty) \,/\, \left(\frac{1}{2}\right) \rho (\Omega R)^2$
C_T	Thrust coefficient, $= T / \rho \pi \Omega^2 R^4$
d_p	Particle diameter, μm
$F_{\Delta \mathrm{P}}$	Pressure lift force, N
$F_{\Delta \mathrm{P}} / W_p$	Pressure force-to-particle weight
F_D	Aerodynamic drag force, N
F_G	Gravitational force, N
F_i	Inter-particle force, N
F_L	Lift force, N
F_M	Magnus lift force, N
M	Aerodynamic moment, N m
N_b	Number of rotor blades
N_v	Number of vortices
P	Pressure measured at the ground below the rotor, lb ft^{-2}
P_∞	Ambient pressure, lb ft^{-2}
r	Radial distance from the axis of rotation, m
R	Rotor radius, m
Re_{tip}	Reynolds number, $= \rho V_{\mathrm{tip}} c / \mu$
r_p	Particle radius, μm
T	Thrust, N
V_{ind}	Velocity induced at the ground below the rotor, m s^{-1}

V_h	Hover induced velocity, $= \sqrt{T/2\rho A}$
V_∞	Freestream velocity, m s^{-1}
V_s	Convection velocity of vortex along the ground, m s^{-1}
V_{tip}	Rotor tip speed, $= \Omega R$
w	Rotor induced velocity, m s^{-1}
W_p	Weight of particle, N
z	Vertical distance above the ground plane, m
Z_0	Distance from the camera lens to the object, m
z_i	Distance from the camera lens to the image, m
Z_v	Vortex height above the ground, m
Z_p	Particle height above the ground, m

Greek Symbols

Γ_v	Vortex strength, $= 2\,(C_T/\sigma)\,\Omega R c$
ΔP	Differential pressure, $= P - P_\infty$
ΔP_{min}	Minimum differential pressure required to lift the weight of a particle, lb ft^{-2}
Δt	Time delay between image pairs, μs
Δr	In-plane displacement in the radial direction, m
Δz	In-plane displacement in the vertical direction, m
Δy	Out-of-plane displacement, m
$\partial\phi/\partial t$	Unsteady pressure term, where ϕ is the velocity potential
ε	Relative error from perspective of image
ζ	Wake age, $= \Omega t$
η	Fluid viscosity, kg m^{-1} s^{-1}
θr	r-angle for a position in the field of view, degrees

θ_z	z-angle for a position in the field of view, degrees
ρ	Air density, kg m^{-3}
ρ_p	Mass density of particles, kg m^{-3}
σ	Rotor solidity, $= N_b c/\pi R$
ψ	Blade azimuth angle, degrees
Ω	Rototational frequency of rotor, Hz
ω	Particle spin, Hz

Chapter 1

Introduction

1.1 The Problem of Brownout

The phenomenon of "brownout" occurs when rotorcraft (e.g., helicopters or tiltrotors) operate in arid environments over unprepared surfaces covered with dust or sand, a representative photograph of the phenomenon being shown in Fig. 1.1. As the rotor wake (or wakes in the case of multiple rotors) interacts with any loose material lying on the ground, a series of complex fluid dynamic uplift and mobilization mechanisms begin to mobilize and uplift the sediment particles, which can quickly produce a large dust cloud around the rotorcraft. The process starts when the impinging rotor wake on the ground subjects the initially stationary particles to aerodynamic forces that can become sufficiently large enough to mobilize and displace them from the sediment bed. The airborne particles may then move downstream and re-impact the bed and so collide with other stationary particles, a process called saltation. The saltation process produces a concentrated layer of suspended particles just above the bed, which is called a saltation layer. The flow velocities in the wake near the ground has signifiant upwash components, which soon uplifts mobilized particles away from the saltation layer and a dust cloud can then quickly develop around the rotorcraft.

One of the consequences of brownout is that it creates a degraded visual environment (DVE) for the pilot. Having to maneuver an aircraft near the ground in DVE conditions poses very obvious dangers, i.e., the dust cloud can obscure visibility of the take-off or landing zone, depriving

Figure 1.1: A helicopter encountering brownout conditions during a landing. (Photo is courtesy of Optical Air Data Systems LLC.)

the pilot of important visual cues needed for safe flight operations. Normally, the pilot relies on views of the horizon, nearby objects or structures, or even the textures of the ground surface, to establish spatial orientation of the aircraft, so there is little latitude for error when flying near the ground. The relative motion of the swirling dust cloud can cause the pilot to experience not only DVE conditions but issues such as vection illusions (i.e., apparent motion sensations) become of concern. As a result, the pilot could experience spurious sensory cues and execute inappropriate flight control inputs, and if these occur close to the ground then the aircraft could crash into nearby obstacles or the ground itself. Indeed, brownout conditions are the leading cause of human factor-related mishaps for military rotorcraft operations [1]. Civilian helicopters can also experience brownout, especially during MEDEVAC or other rescue efforts that involve operations from unprepared landing zones [2].

There are also other consequences of brownout. The copious quantities of dust particles up-

lifted during brownout conditions can also accelerate the wear of mechanical components on the rotorcraft and shorten their life spans. For example, in some cases the rotor blades can be abraded such that they become unairworthy in just tens of flying hours, and engines may need to be overhauled in just a few hundred hours of service. The need for expensive repairs and more frequent maintenance drives up the operating costs for the rotorcraft and reduces its mission readiness. The swirling clouds of dust creates a harsh environment not only for the vehicle but for personnel working on the ground, especially for sling-load operations. Therefore, ground operations can be hindered or limited by the occurrence of brownout out of concern for the safety of the ground support crew.

Because the operation of rotorcraft in brownout conditions poses a safety of flight risk, developing some means by which to mitigate the formation and severity of a dust cloud is important. Thus far, mitigation efforts have centered around the use of sensors, avionics, and the adoption of certain operational strategies, i.e., appropriate flight path management by the pilot. Sensor technologies are designed to penetrate the dust cloud and allow the pilot to "see through" it with the aid of advanced avionics displays. These displays provide information about the surroundings to replace the loss of important visual cues [3–5]. Flight path management such as modified take-off maneuvers and landing approaches have also been used as a means of mitigating brownout [6]. One method is to outpace the developing dust cloud by flying at faster airspeeds nearer the ground. The time in flare and hover before landing can also be reduced to potentially stir up less dust. Alternatively, the rate of descent during landing can be increased in an attempt to land before the dust cloud has time to fully evolve. However, operationally mitigating the effects of brownout with

landing and/or takeoff tactics has only met with limited success because the degree of mitigation from such strategies depends on many factors. For example, the severity of brownout will be affected by the weight of the rotorcraft, the density altitude at which it is operating, as well as the characteristics of the loose material on the ground. Furthermore, the required brownout mitigation maneuvers can themselves introduce an elevated risk to flight safety because of the increased airspeeds and rates of descent that are often used near the ground.

Recognizing that brownout is a complex, dual-phase, fluid mechanics problem, consideration should be given to mitigation strategies that target the problem at its source. Available evidence suggests that the characteristics of the resulting brownout cloud can vary significantly from rotorcraft to rotorcraft. Some dust clouds produced by certain rotorcraft are more toroidal in shape, expanding more radially away from the rotor(s) than vertically above it. This type of dust cloud is often considered more preferable because it maintains a region of better ground visibility for the pilot, as suggested by the photo in Fig. 1.2. Other helicopters can produce large, dome-shaped clouds that rise above the height of aircraft, with the suspended dust often being reingested through the rotor disk and being bombarded back onto the ground at high velocity. To try to explain why some rotorcraft have been observed to generate different brownout signatures, Milluzzo and Leishman [7] have subjectively characterized brownout severity from photographs of rotorcraft in brownout conditions and have attempted to relate the severity to certain geometric characteristics of the vehicle (e.g., rotor radius, number of blades, etc.) as well as the operating conditions (e.g., rotor disk loading).

Because brownout results from the interaction of the vortical rotor wake with loose sediment

Figure 1.2: A landing helicopter with the formation of a more favorable ring or toroidal shaped dust cloud that forms away from the immediate landing zone.

particles on the ground, understanding the details of this process is a prerequisite to brownout mitigation. The spatial extent, concentration, and rapidity of development of brownout clouds can vary significantly with rotor blade design, the number of blades, the number of rotors, the disk loading, etc. These rotorcraft design parameters influence the characteristics of the vortical laden rotor wake, such as its geometry and flow velocities. Moreover, the main feature of the wake, which are the trailed blade tip vortices, is also affected by the rotorcraft design and operating conditions, which determine vortex strength, vortex spacing, vortex height above the ground, and the location of wake impingement on the ground. It is important to appreciate, though, that even the same rotorcraft performing the same flight maneuvers can produce differing brownout conditions because the severity of the problem also depends on the type of surface sediment, its size, compactness, moisture content, etc. In light of the wide range of factors that can influence brownout, computational modeling [4, 5, 7] is one approach that has been used to help understand the different effects produced by combinations of these rotorcraft design parameters.

1.2 The Physics of Brownout

The fundamental cause of brownout lies in the mechanisms of fluid dynamics. Brownout is a dual-phase flow problem, i.e., the carrier phase describes the three-dimensional, unsteady flow of the rotor wake, while the dispersed phase consists of a nonuniform concentration of sediment particles that have been uplifted from the ground under the action of the rotor wake. The dual-phase nature of brownout makes it a complex problem to measure, understand, or to model. To compound this complexity, these flow phases are intrinsically coupled, which means each can influence the other through transfers of momentum and energy, and particle collisions further compound the complexity of the dual-phase flow.

Figure 1.3 is schematic showing some of the fluid mechanisms and sedimentology (or aeolian) processes that may be involved the formation of a brownout cloud. The impingement of the rotor downwash and its embedded vortical flow on the ground induces an unsteady velocity and pressure field above the sediment bed. If the velocity or pressure exceed some critical threshold levels, the loose particles that are at rest on the bed can be mobilized. Once the particles have been mobilized, they will either fall back to the bed under the action of gravity or other forces will cause them to be entrained into the flow. For example, vortices that are passing over the bed will create strong upwash velocities, which means they can trap and lift mobilized particles into the flow. Once airborne, they can remain suspended, impact other airborne particles, or be re-ingested by the rotor. Reingested particles often attain much higher velocities such that when they collide with the ground they will dislodge many more particles that can then be entrained by the flow; this cascading nature of brownout leads to a rapid increase in the total quantity of airborne particles [8].

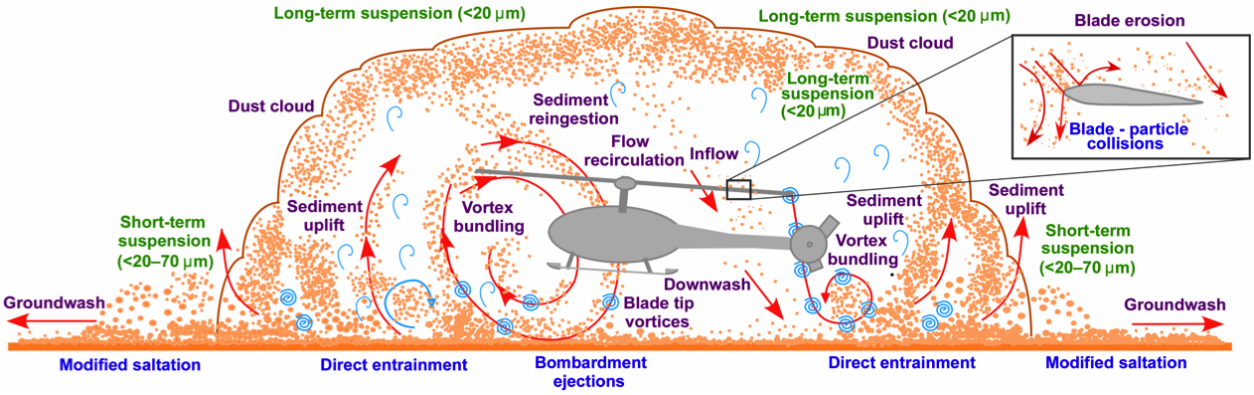

Figure 1.3: Schematic showing the different modes of sediment particle motion and the resulting dust field generated by the rotor wake from a helicopter hovering over a surface covered with loose material.

1.2.1 Representative Rotor Flows in Ground Effect Operation

From a performance rather than fluid dynamics perspective, rotors operating in ground effect have already been extensively studied [9–15]. Results have shown the advantage of a rotor thrust increase for a given power when operating a rotorcraft in ground effect, i.e., less power is required to generate the same thrust. This result occurs because the induced velocity decreases as compared to operating out of ground effect at the same rotor thrust.

The presence of a ground surface beneath the rotor also influences its developing wake structure. While the near-ground flow below a rotorcraft is not fully understood, some prior fluid dynamic studies have been undertaken. Lee et al. [16] examined the stretching and straining of a vortex filament trailed from a small-scale rotor when operated at various heights above the ground. Milluzzo et al. [7] looked at the effect of blade tip shape on swirl velocities in the flow and how they persisted in the near-wall region at the ground. Obviously a better understanding of the interactions of vortical flow and turbulence with the ground plane and loose surface material is crucial to the understanding of brownout.

The flow visualization (FV) images in Figs. 1.4 and 1.5 have used smoke particles illuminated by a laser sheet to trace the flow for a rotor operating out of ground effect and also in ground effect, respectively. As the blade passes through the light sheet, the smoke particles reflect the light and helicoidal vortex filaments becomes visible. These vortex filaments are rendered visible in the FV images by means of the darker circular regions that demarcate the inner region of the vortex cores. Comparing the two wakes, it is evident that the wake contracts earlier and closer to the rotor tip-path-plane (TPP) for out of ground effect operation; see Fig. 1.4. The vortex cores for this wake are also more laminar, as evidenced by the smooth flow near their cores. The action of turbulence and viscosity cause significant diffusion of the vortices after only 2–3 rotor revolutions. Further downstream, the adjacent turns of the helical vortices begin to pair with each other, which can also lead to a form of wake instability.

The initial contraction of the wake in ground effect operation is followed by an outward or radial expansion as it approaches the ground. The radial expansion and the turning of the rotor flow creates a turbulent wall-jet like flow along the ground that initially thins and then thickens as it develops further downstream over the surface. The flow expansion also causes the vortex filaments to undergo stretching, which results in a reintensification of their vorticity. Because of this reintensification, the process of diffusion is slowed, allowing the vortices to persist to later wake ages in the flow (4–5 rotor revolutions). The stretching action of the vortex filaments as they near the ground will influence sediment mobilization because it also causes the swirl velocities there to increase. The flow physics of rotors operating in ground effect are explained in more detail in Refs. [7, 8, 16, 17].

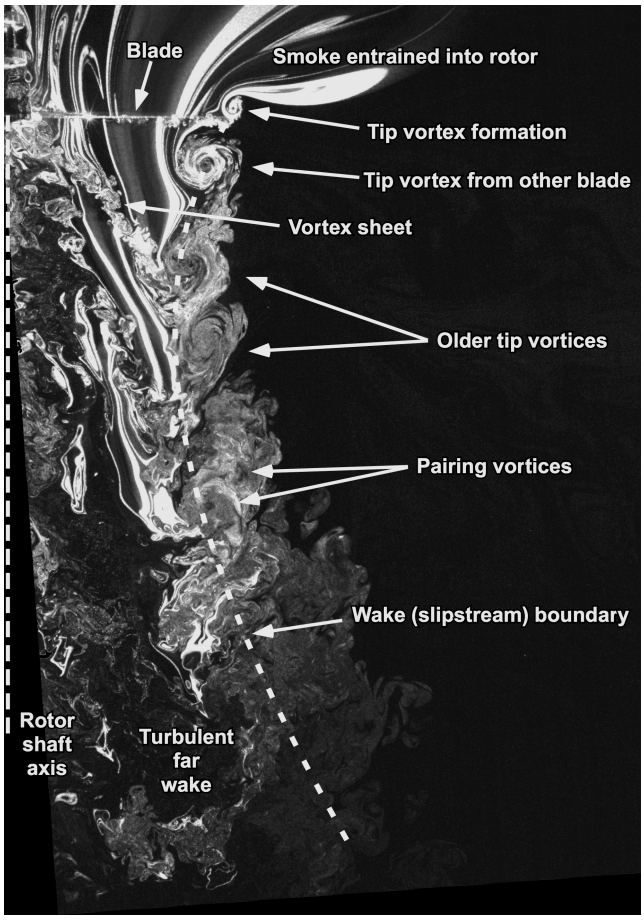

Figure 1.4: Example of the downstream wake of a rotor operating out of ground effect.

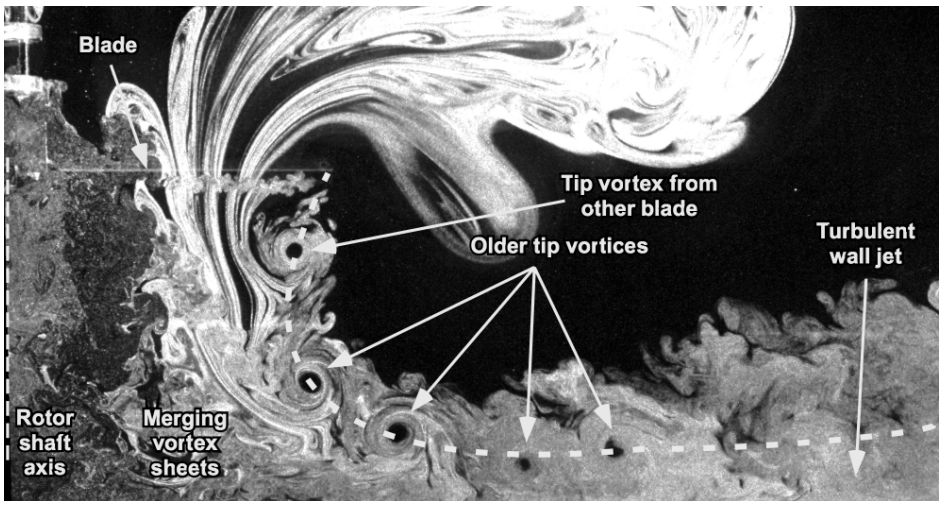

Figure 1.5: Example of the downstream wake of a rotor operating in ground effect.

Of course, brownout is not restricted to the case of steady hover. It is also a problem that rotorcraft encounter during take-off and landing operations, i.e., what would be classified as a flight maneuver. The flow field in this case is more complex than that for hover because of changes in rotor height and velocity near the ground. These changes can produce localized regions of the flow which can affect the transport of sediment particles. There are two characteristic flow regimes that are seen during these flight maneuvers [18]. As forward speed builds, the vortex filaments bundle and roll together, swelling into a "ground vortex" just ahead of the rotor. If there are loose particles here, then they would be uplifted recirculated through the rotor disk by this ground vortex. If this recirculation occurs through the front of the rotor disk, then the pilot's view of the surroundings can be obscured. These flow regimes will also affect particle mobilization and entrainment during take-off and landing operations [13, 18, 19].

1.2.2 Sediment Particle Dynamics

The science of sediment transport, the crux of the brownout problem, is a an expansive field of research in of itself. This field can be divided into two main categories: One being wind-driven particle transport like that seen with desert sands (i.e., aeolian physics) and the other being hydrodynamic particle transport, which can occur in river or coastal environments. While there are many rotorcraft-specific factors that can influence particle motion and potentially contribute to the formation and intensity of brownout clouds, including rotor parameters (such as disk loading, blade loading, rotor design, and tip shapes), the flight path of the helicopter, the helicopter configuration and wake-fuselage interaction, the sediment properties also have a key role in brownout. The

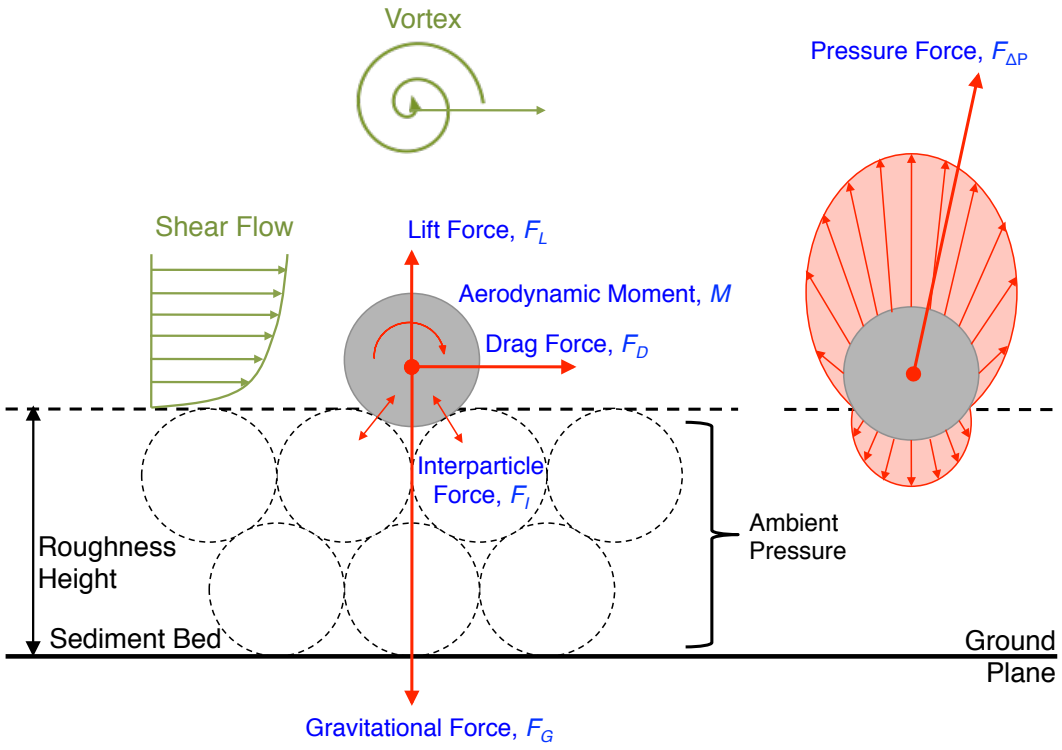

Figure 1.6: Schematic showing the forces and the pressure distribution acting on a stationary particle on a sediment bed.

texture, composition, and land-surface characteristics (e.g., topology, moisture, and aerodynamic roughness height) can all potentially influence the severity of brownout.

To understand the interaction of the rotor wake with the sediment bed (and its various particle and other properties), consider how the particles respond to the flow. As fluid moves past them, they experience various forces. Figures 1.6 and 1.7 show schematics of the different forces exerted on a particle, for both the stationary case when a particle resting on the bed and then when a particle is airborne.

A stationary particle resting on a bed of other sediment particles is subjected to a gravitational force, inter-particle forces, and for the case in which there exists an external flow above the bed, the sediment particles also encounter fluid dynamic forces [20]; see Fig. 1.6. The external flow

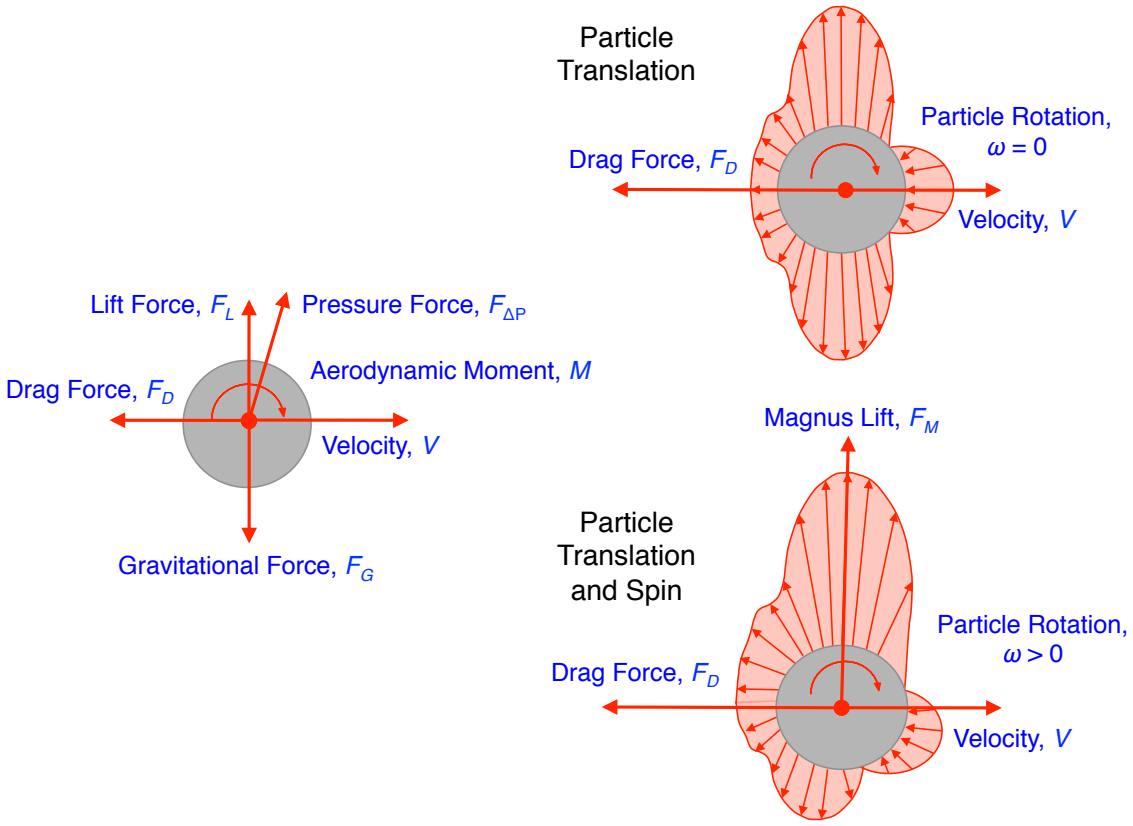

Figure 1.7: Schematic of the forces and pressure distribution acting on an airborne particle.

forms a boundary layer on the ground plane because of viscous effects. The shearing action of the boundary layer imparts an aerodynamic lift force on the sediment particles (perpendicular to the fluid flow direction) and an aerodynamic drag force (parallel to the fluid flow direction). These aerodynamic forces will vary with the square of the particle diameter, i.e., an area effect, as well as with Reynolds number. However, the magnitude of the drag force is also dependent on the geometry of the particles. For example, there will be less drag on a spherical particle than for a tetrahedral particle because the tetrahedral particle produces more complex regions of flow separation, a consequence of its more complex shape (i.e., separated flow will increase the pressure drag on the particle).

There are several sources of the lift forces acting on a particle. The Saffman force is lift generated when a velocity gradient exists across the dimensions of a particle, which creates a different pressure on one side of the particle compared to the other [21]. If the particle were to be spinning, its spin could produce an additional lift force called a Magnus force. In terms of their relative effects on particle motion, the Saffman force has small effects on the trajectories of saltating particles, while the Magnus force can have a more significant effect on the maximum saltation height and horizontal saltation distance. However, at low rates of particle spin, the Magnus forces are generally smaller than the Saffman force [22].

It has been hypothesized that the passage of a vortex over a sediment bed could produce a low pressure region of sufficient magnitude to actually lift particles up from the bed even in the absence of shear. The relatively strong pressure gradients present in vortical flow could produce a lift force on particles similar to the Saffman force, but it is likely to be a stronger and periodic force because in the case of a rotor wake it is associated with vortex passage above the bed. Much of the present work will focus on evaluating the potential influence of this "pressure lift force" on particle mobilization.

The gravitational force is a volumetric effect and varies with the cube of the particle diameter, whereas the various inter-particle forces will range in magnitude. These inter-particle forces are mostly cohesive, meaning that they stick together and resist uplift. Among them are Van der Waals forces [20], which scale linearly with particle size, and are actually a collection of forces that are produced from interatomic or intermolecular interactions, e.g., so-called dipole-dipole interactions. Electrostatic forces result from a difference in electric charge among neighboring

particles. There are many mechanisms for generating electrostatic forces, including an exchange of ions or electrons between particles in contact.

When the moment created by the aerodynamic lift and drag forces on a particle exceeds the gravitational and inter-particle forces it is experiencing, then that particle will begin to move, pivoting around its point of contact with other particles to follow the direction of the flow. In a steady boundary layer flow, this is the threshold condition for particle mobilization, and the effective flow velocity required to produce this initial motion, is often referred to as the threshold friction velocity, u_{*t}, where $u_{*t} = \sqrt{\tau_w/\rho}$. Once this threshold has been reached and particle motion has been initiated, the lifted particles first follow ballistic-like trajectories, which are primarily determined by the relative balance of gravitational and aerodynamic drag forces.

There can also be secondary forces that act upon an airborne particle and affect its trajectory; see Fig. 1.7. Inertial forces such as centripetal and Coriolis forces can have an affect in the case where airborne particles are moving through a fluid with a large flow curvature, e.g., as in a vortical flow. The forces experienced by a particle during the collision with another particle can also influence its trajectory. Furthermore, there is some evidence that electrostatic forces [20] can increase particle concentrations and affect the particle trajectories.

1.3 Prior Work

The physics of the two fluid phases (air and sediment) that comprise the problem of brownout have been described separately, but it is the physics of the interaction of those phases that is of significance. When the rotor wake comes into proximity of a mobile sediment bed, the interactions

result in sediment uplift and the formation of a particle or dust cloud. To explain the means by which sediment is mobilized by the rotor wake, particle entrainment mechanisms and vortex-wall fluid dynamics interactions will be summarized. Recognizing that the transport of sediment is a broad field of study in of itself, work from the aeolian sciences will be discussed to supplement the understanding of the resulting particle dynamics. Attempts at modeling the behavior of mobilized dust will also be reviewed. Lastly, because pressure effects have been hypothesized to participate in the onset of brownout conditions, and because there exist no previous measurements of ground pressure beneath a rotor, studies of surface pressure distributions as a result of rotor wake/body interactions will be reviewed.

1.3.1 Sediment Entrainment Mechanisms

Particle motion under the action of an external or carrier flow is comprised of three main processes: (a) mobilization, which is marked by the incipient mobilization of particles by the external flow, (b) entrainment, which involves processes responsible for uplift of sediment particles from the bed under the influence of the fluid flow, and (c) transport, which governs the trajectory followed by a sediment particle after it is entrained into the flow field. Experimental studies of the wake of a small-scale rotor interacting with a mobile sediment bed have identified multiple sediment entrainment mechanisms simultaneously at work on the particles [8], which are illustrated in Fig. 1.8.

Direct aerodynamic entrainment occurs when the aerodynamic forces exceed the gravitational and inter-particle forces on the particle. Entrainment of the particles by means of unsteady

pressure effects has also been hypothesized, which is the main subject of the present study. The rolling motion of particles along the sediment bed is called creep. Creep manifests when the forces acting in the vertical direction are not sufficiently large to uplift the particles, either because of large particle size or low vertical flow velocity in the region. The bouncing and jumping motion of particles across a surface is called saltation. Saltation has been identified as the principal mechanism involved in the transport of sand particles in unidirectional flows, like the wall-jet region at the ground below the rotor. Strong vortex-induced regions of upwash can entrain particles that are in saltation. Entrained particles can be uplifted and suspended for long-term or short-term durations. Particles in the range of 20 μm $\leq d_p \leq$ 70 μm can remain suspended for hours, but very small dust particles ($d_p \leq 20$ μm) can remain suspended for several hours or even days. These suspended particles can be re-uplifted by regions of concentrated vorticity or by means of recirculation through the rotor disk. Entrained particles can impact the bed below the rotor with higher momentum, introducing many more particles into the flow by means of bombardment ejections. The ejected particles are now more easily entrained into the flow. The continuous cycle of mobilized particles generating newly mobilized particles, which could be entrained and eventually create their own bombardment ejections of additional particles, explains why a large dust cloud can rapidly engulf a rotorcraft when it is landing or taking off.

1.3.2 Vortex-Wall Fluid Dynamic Interactions

One aspect of wake-ground interactions that has a profound effect on sediment mobilization is the event of wake impingement, during which the vortex filament comes close to the ground and

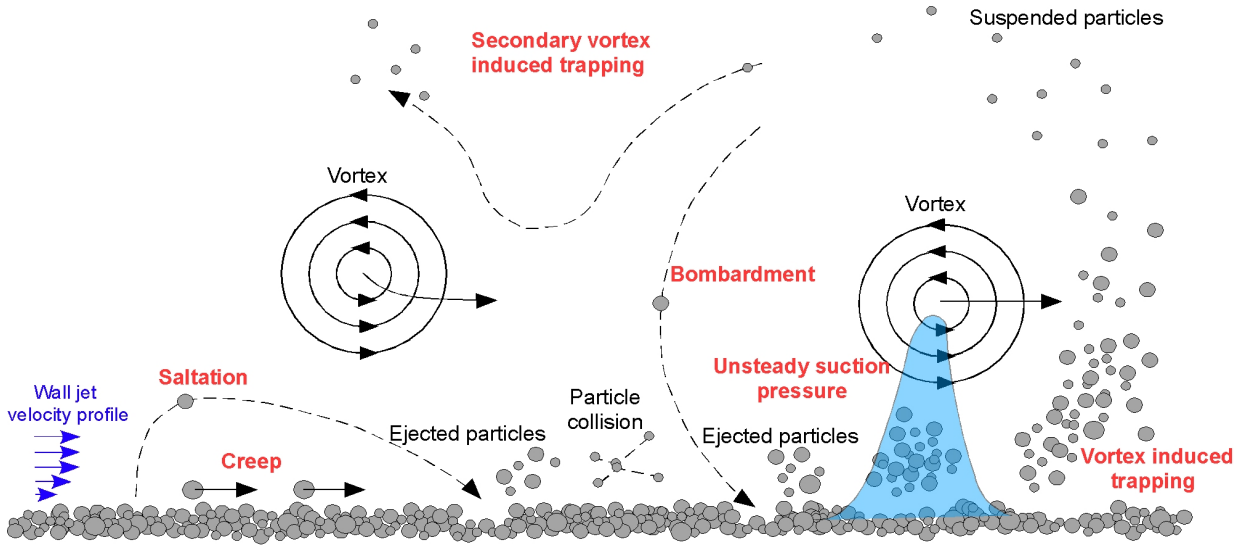

Figure 1.8: Schematic illustrating the various sediment transport mechanisms that may occur below a helicopter rotor when it is operating over a mobile sediment bed.

interacts with it. Insight into this specific event can be seen from the more idealized case of the interaction of a vortex ring with a wall. Experiments by Doligalski and Walker [23, 24] showed that the convection of a vortex near a solid wall induces a viscous response in the near-wall flow. Unsteady flow separation develops because of an adverse pressure gradient. A period of explosive boundary-layer growth culminates in an abrupt eruption of the flow from the surface. This eruption usually leads to the formation of a secondary vortex structure, i.e., in this case a ring, attached to the wall and with circulation opposite to the primary vortex. Interactions between the primary and secondary vortex can sometimes induce the formation of a third vortex ring near the wall.

Factors that can influence sediment uplift are particle diameter and bed permeability, which have interrelated effects. Bethke [25] studied a vortex ring interacting with a particle layer in a dual-phase flow. In that work, it was suggested that a secondary flow passing through the porous bed may affect the growth and detachment of the boundary layer. This means that particle uplift

may be affected in that particles may be convected upward by the fluid leaving the particle bed. Bed permeability may also affect the quantity of particles that are displaced. For a loosely-packed bed (or a bed of particles large in diameter) the vortex ring penetrated more deeply into the layer and was stretched less radially. Conversely, for a densely-packed bed of small diameter particles, the vortex ring barely eroded the layer, an indication of more shallow penetration, but was stretched more noticeably than for the densely packed bed. It is also known that vibrations can affect the inter-particle forces with a packed bed. Thus, the intermittent presence of the blade tip vortices, vortex sheets, and secondary vortical structures near the bed in a rotor-induced flow field may influence the inter-particle forces [26].

1.3.3 The Aeolian Sciences

To further understand the processes of sediment transport, computational and experimental work from the field of aeolian science was reviewed. A detailed study of the mobilization and convection of sediment particles by the action of air was first conducted by Bagnold [27]. This work, which studied the aerodynamic drag and gravitational forces acting on particles, introduced the concept of a threshold friction velocity and a model for sediment mobilization. Similar studies by Greeley and Iverson [28] used Bagnold's concept of threshold friction velocity, but also incorporated inter-particle forces. This amended model was later simplified by Shao and Marticorena [29, 30] to give a physical representation of the effects of different forces associated with sediment motion.

Lu and Shao [31] developed a model which captured bombardment ejections, which is

known to be an important mechanism in the formation of dust clouds. Saltating particles were modeled to impact the bed, and with each collision, a volume of dust was removed, forming a crater. The improvement over previous models was that the microphysics of this process could be estimated, i.e., it provided an estimate of the volume of dust ejected by each impact. However, the model was based partly on the concept of a plastic pressure, a bed property that is difficult to measure. Shao [32] later developed a more general form of the model to address this limitation, in which the plastic pressure of the bed varied with particle velocity as the particle plowed through the bed.

Sutherland [33] examined the entrainment of sediment particles in turbulent flows. The outcome was an entrainment hypothesis covering the following points. First, sediment motion is initiated when turbulent eddies disrupt the viscous sublayer, which occurs when the local shear stresses increase beyond critical values. Second, turbulent eddies, with their swirling motion, exert a drag force on the particles. Consequently, the particles roll over their neighbors if the vertical velocities in that region are sufficient to lift particles from their stationary positions on the bed.

Laboratory simulations of dust entrainment by tornados or "dust devils" were performed by Greeley and Iverson [34–37] by using a vortex generator. This study examined the threshold conditions for the entrainment of sediment. It was observed that, below a vortex core the region of low pressure induced by vortical flow can generate extra lift forces on the particles. If these additional lift forces overcome inter-particle forces, then the threshold conditions for sediment mobilization are affected. The contributions of pressure forces in vortical flows were shown to be significant for the entrainment of smaller-sized or dust particles. The particles in this size range are

usually fairly cohesive and are generally difficult to entrain by the action of shear stresses alone. Furthermore, studies conducted to understand the fluidization of packed beds have shown that the pressure differences on the bed can also affect the inter-particle forces and, therefore, affect the entrainment of small dust particles.

In addition to developing models of sediment transport, Shao [38] experimented with the entrainment of small dust particles via saltating particles over wind-blown surfaces. An upstream bed of sand was used to start the saltation process, and saltating sand particles then bombarded a downstream bed of dust particles. Saltation bombardment, not the direct (shearing) action of the aerodynamic forces, was found to be the principle entrainment mechanism of dust, and the resulting ejections were suggested to be an important contributor to the formation of dust clouds. A dust flux emission model was developed, which balanced the particle binding energy and kinetic energy of saltating particles.

1.3.4 Models of Particle Motion

It is important to the understanding and eventual mitigation the problem of brownout that simulations are developed that accurately model the sediment transport mechanisms that control the very genesis of the dust cloud. Most existing models of particle motion can be divided into two types: Eulerian-based particle entrainment and dispersion (PED) models and models utilizing a Lagrangian-based methodology. Ryerson et al. [39] resolved the in ground effect flow field, solving the RANS equations with a momentum-source representation for the rotor blades. The advection-diffusion equations were used to solve for particle concentrations in space and time,

and a logarithmic boundary layer profile was assumed near the ground. This model was limited, however, by its inability to represent the localized effects of the blade tip vortices that are known to entrain dust particles.

Haehnel et al. [40] coupled the PED model with with an unsteady incompressible flow solver [41–43]. A surface vorticity confinement method preserved vorticity in the tip vortices, and a logarithmic boundary layer profile was again assumed near the ground. While this model was able to model the effects of the blade tip vortices, it still did not incorporate the important mechanism of bombardment ejections and particle/ground interactions that are now known to be fundamental to the brownout problem.

A model by Phillips and Brown [19] used an Eulerian particle transport method similar to the PED model. The mass transport (vorticity) equations were used to analyze the dust convection problem in an Eulerian reference frame, while also employing the expression for threshold friction velocity developed by Shao [29]. The advantage of this model was that it was able to model the mechanism of saltation with a source model.

Models using a Lagrangian-based type of methodology, where the particle equations of motion are solved in the Lagrangian frame, include that of Wachspress [44]. This model used a constant vorticity contour (CVC) based on the free vortex method (FVM) [44–46]. Particles were entrained based on a threshold friction velocity [29]. Because the threshold velocity predicted by this model was too high for smaller-sized particles, which are predominant in brownout clouds, ad hoc modifications were made to the coefficients of the model to commensurately reduce the threshold velocity. Also, a computational savings was gained by convecting the particles in clusters.

A Lagrangian-based brownout simulation methodology, similar in structure to the previous model, was developed by D'Andrea [47–50]. The rotor flow was modeled using a full-unstructured panel method and was coupled with a time-accurate free-vortex wake model (based on the CVC approach). The particle entrainment was again based on the threshold friction velocity expression of Shao.

Up to this point, all the existing brownout simulations methodologies described herein [19, 39, 40, 44, 47] were based on threshold models that consider only boundary layer shear effects and inviscid rotor wake solutions. Therefore, such models cannot represent the details of fluid and sediment particle interactions in the near-wall region. These models often utilize simplifications that neglect particle-particle collisions and the transfer of momentum from the particles to the fluid (i.e., assuming one-way coupling). Pressure effects and bed permeability were also not modeled. Yet, these phenomena are important, as evidenced in study by Morales and Squires [51], who examined the detailed particle dynamics in a turbulent boundary layer under the action of vortices. This latter study indicated that vortices affect the boundary layer flow, which agrees with aforementioned conclusions from the vortex-wall interaction studies, and also suggests that the effects of particle collisions may be more significant in the near-wall region.

Recent work by Syal [52] proposed a new threshold entrainment model that is more appropriate for vortex dominated flow fields. This model explored the inclusion of the explicit effects of pressure forces. It was shown that the value of the threshold friction velocity decreases with a reduction in pressure over the bed. This decrease is clearly significant for intermediate-sized particles, which are neither too cohesive nor too heavy. The presence of wall-normal stresses, produced

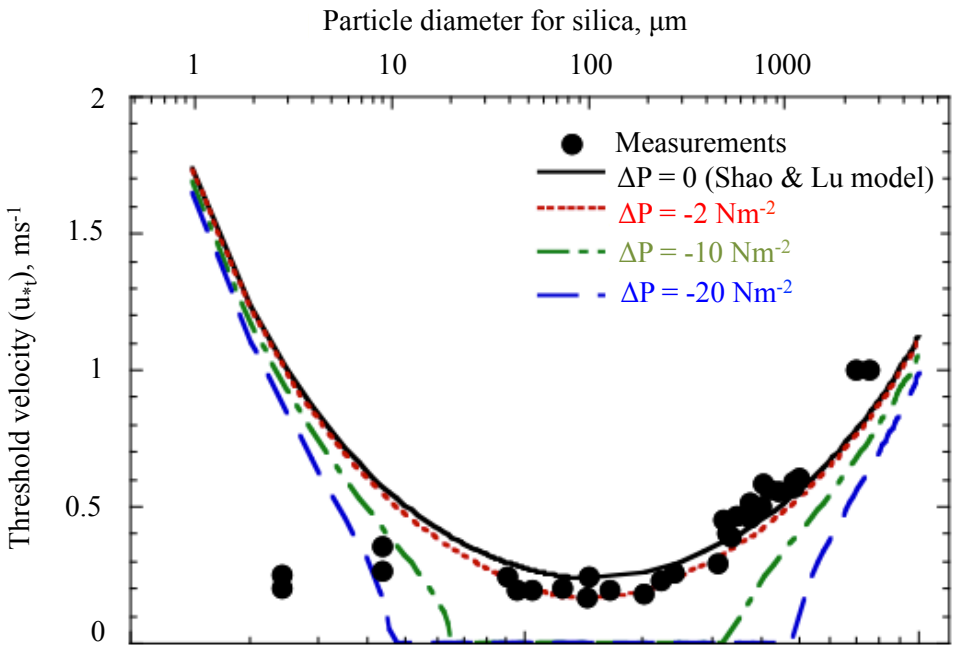

Figure 1.9: The relationship between threshold friction velocity and particle diameter.

by pressure effects, can reduce the threshold shear stresses that are required to mobilize and entrain a particle. In fact, if the pressure difference over the bed becomes large enough, particles could be mobilized even in the absence of shear. For very large or very small particles, a much larger decrease in pressure will be required to achieve mobilization; see Fig. 1.9.

1.3.5 Rotor Wake/Surface Interactions

There have been no previously documented experiments that have measured the distribution of unsteady pressure on a ground plane below a hovering rotor. However, there have been measurements that have documented the unsteady loads on bodies and other surfaces exposed to vortical flows. From a review of previous research in the field of rotor wake/body interactions [53–55], a vortex convecting over a surface can produce a significant negative pressure pulse and an associ-

ated large adverse pressure gradient. The nature of the pressure response has been found to exhibit some sensitivity to the properties of the vortex as well as the vortex convection speed and its location relative to (i.e., above) the surface. The impingement of a rotor wake on a ground plane will likely produce a suction pressure as well, and the pressure response will also be dynamic, changing as the wake approaches the ground, turns, and accelerates radially outward away from the rotor.

Brand et al. [56, 57] as well as Bi et al. [55] both performed experiments to study the interactions of a rotor wake with geometrically simplified airframe shapes. Three prominent periodic interactions were observed on the airframe surface, namely a blade passage effect, tip vortex impingement, and vortex sheet effects. Characteristic pressure signatures associated with the blade passage and the vortex impingement were identified. The passage of a blade over the fuselage caused a large pressure excursion, which is related to the lift produced on the blade. The blade passage effect was sharply reduced by increasing the separation distance between the rotor and the airframe. The largest excursions from the time-averaged pressure were seen to occur along the top of the body at the edges of the wake-impingement zone. The impingement of a vortex on the airframe produced a large suction peak, which persisted even after the vortex was no longer coherent enough to be clearly identified in the flow visualization. The effect of the tip vortex was also noted to continue to affect the pressures on the body downstream of the impingement zone. It was concluded that the vortex flow may dominate the instantaneous (time-dependent) pressure signature, rather than the blade passage effect. Bi et al. [55] further divided the process of tip vortex interaction with a body into three regimes: close tip vortex/body interactions, vortex/surface impingement, and post-vortex/surface impingement. The pressures at points on the body were found

to exhibit a high sensitivity to the tip vortex parameters, such as the vortex convection speed and vortex location relative to the body.

In many cases, it has been found that these observed surface pressures can be adequately modeled with the use of a potential flow analysis. This information implies that modeling may also provide some insight into the problem of pressure induced on a ground plane below a rotor. Two separate models, a vortex ring wake and a planar surface model for the body and a prescribed wake with an unsteady panel representation of the body, were introduced by Crouse et al. [58]. Because viscous interactions can play a strong role in the wake/body impingement, the pressure response associated with this process was not so easily predicted with a potential flow model. However, unique pressure signatures were still identified and correlated to specific flow events. From prior experiments, the main types of pressure signatures were concluded to be the result of blade passage, close wake/body interactions, and the impingement of the wake upon a surface.

Affes and Conlisk [53] modeled rotor wake/body interactions using an idealized tip vortex as a single three-dimensional vortex tube and a fuselage that was modeled as an infinite circular cylinder. The motion of the vortex was found to induce a strong axial adverse pressure gradient on the cylinder directly below the vortex. This event resulted in a very strong negative pressure pulse, which has also been observed in similar experimental work. In later work, Affes and Conlisk [54] used experimental results to validate their model of a tip vortex approaching a cylindrical airframe. Both the position and magnitude of the suction peak induced on the airframe were found to be adequately predicted from a potential flow analysis until just before the impingement of the vortex on the airframe surface. In the case of wake impingement on the ground, the vortex filament never

completely impinges on the surface in the way that it does on a fuselage. While the inherent limitations of a potential flow model in predicting pressure at the actual impact of a vortex may compromise the ability to satisfactorily model the current problem, a simple model such as this could give insight into the expectations of the ground pressure responses below a rotor.

1.4 Objectives of the Present Work

To understand the significance of the vortex-induced unsteady pressure field in terms of sediment mobilization and uplift, a careful study of the pressure variations over a ground plane below a rotor is needed and this was a primary objective of the present work. As previously explained, various measurements exist that document the pressures along the length of a fuselage under the influence of a rotor wake, but ground surface pressure measurements are not available. After pressure measurements are obtained, it is possible they can be correlated to the flow field measurements to isolate the specific pressure response to each flow event, i.e., to vortex passage and/or wake impingement in the manner that has been done in previous rotor/airframe studies.

One of the specific goals of the present work was to dissect the complex flow field in the rotor wake near the ground into regimes that showed similar flow characteristics. If the relative magnitudes of pressure and representative pressure signatures can be identified for each regime, then the response of particles to the flow within each regime can be evaluated in terms of the flow velocities needed to initiate particle motion. The relationship between pressure fluctuations and the corresponding height of sediment uplift and flow velocity components could then be used to establish causation, e.g., large concentrations of particles can be identified and their positions

evaluated relative to the convecting vortices. Concentrations of particles that are found to occur in the proximity of vortices could provide evidence supporting the existence of a pressure lift force.

The main objectives of the present work were to better understand the effect of pressure fluctuations over a sediment bed on the thresholds for mobilization. The aim was to visualize and compare the flow field and the unsteady pressure field in an attempt to establish causation between the low pressure regions within and near to the vortical flow and the entrainment of particles from a stationary bed. Such findings would provide evidence for the existence of a pressure lift force, the significance of which could then be assessed to determine whether or not pressure effects can be important in brownout simulations.

1.5 Organization of Thesis

The phenomenon of rotorcraft brownout, and its causes and consequences, have been described in the current chapter. The published literature describing relevant previous experimental and computational research in the field of brownout have been discussed. A description of the experimental techniques used in the present work, such as particle image velocimetry (PIV) and particle tracking velocimetry (PTV), is described in Chapter 2. Also included in this chapter is a discussion of the technical challenges of data acquisition and their resolution. The results of a scoping study, a model for predicting unsteady pressures on the ground plane, and an analysis of the relationship between the rotor flow and the movement of the sediment particles are presented in Chapter 3. Finally, Chapter 4 gives the conclusions from the present work and proposes some possible directions for future research.

Chapter 2

Description of the Experiments

Experiments were performed to explore the flow environment created below a rotor that was operated in simulated hovering flight above a ground plane covered with a mobile particle bed. The goal was to better understand the possible effects of the fluctuating near-ground pressure field on the processes of particle mobilization and uplift. In this chapter, descriptions of the experimental setup, types of experiments performed, and the specific operating conditions for each test are described. The present chapter also contains a discussion of the technical challenges faced when performing these experiments, and explains the sources of uncertainties that are associated with the various measurements.

2.1 Experimental Setup

A small-scale rotor was used to study the flow produced in the rotor wake at the ground, as well as the trajectories of particles that were mobilized and entrained into the flow field by the rotor wake. Fluctuations of pressure over the ground plane below the rotor were also measured, which was a primary goal of the current work.

2.1.1 Description of the Rotor

The rotor hub was a freely teetering design, which could be operated in either a one-bladed or two-bladed configuration. The rotor had a radius of 84 mm (0.28 ft), as measured from the rotational axis to the blade tip. When operating in the one-bladed configuration, a counterweight was mounted in place of the second blade to achieve dynamic balance; see Fig. 2.1. The blades were made by layering carbon fiber sheets in a curved mold to create cambered plates. The blade sections had a thickness-to-chord ratio of 3%. The leading edge of the blade was sharpened, which is aerodynamically preferable for the low chord Reynolds numbers produced by this laboratory-scale rotor [59].

A brushless motor was used to power the rotor. Figure 2.1 shows the motor housed in the mounting structure, which consisted of four steel rods passing through three aluminum plates. This mount was affixed to a micro-balance to measure the thrust produced by the rotor. The balance itself was mounted upon a tripod so that the height of the rotor plane relative to the ground plane (discussed next) could be adjusted.

A Hall-effect sensor was installed on the rotor shaft to provide a trigger to measure the rotational frequency of the rotor. The motor was capable of spinning the rotor at rotational frequencies as high as 200 Hz, however the rotor frequency was limited to 130 Hz in the present work because this operating condition provided a compromise between creating measurable pressure signals and also sufficiently intense dust clouds that could also be measured, i.e., the cloud was not so dense with particles that the carrier flow driving the particles was not distinguishable.

A rectangular ground plane was securely seated upon tripods, the height of which could be

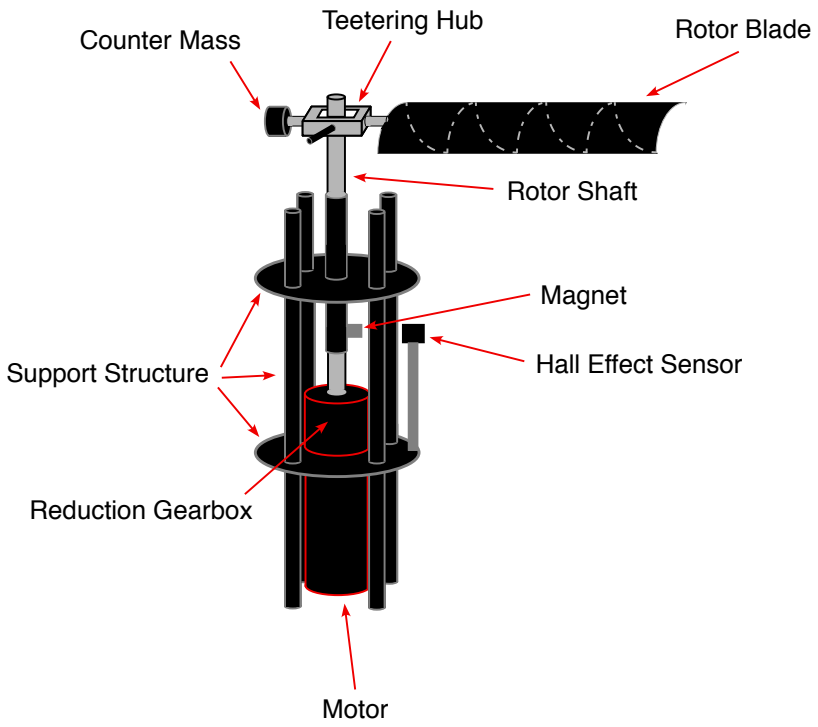

Figure 2.1: The small-scale rotor with its mounting, motor, and configurable teetering hub.

adjusted relative to the rotor plane. The size of the ground plane was 0.905 m $\times$ 0.61 m (2.97 ft $\times$ 2 ft) and was painted black to minimize laser light reflections. Behind the ground plane, along the wall of the dust chamber opposite of the laser, a black fabric was suspended to prevent stray laser reflections. The rotor was located at the centroid of the ground plane.

2.1.2 Flow Measurements

To safely conduct dual-phase flow experiments in which micron-sized particles would become airborne, a method of containment was necessary. Therefore, a ventilated dust chamber was used, as shown in Fig. 2.2. In addition to protecting the measurement apparatus from the dust particles, the Plexiglas walls also allowed unimpeded optical access for the laser and camera. The

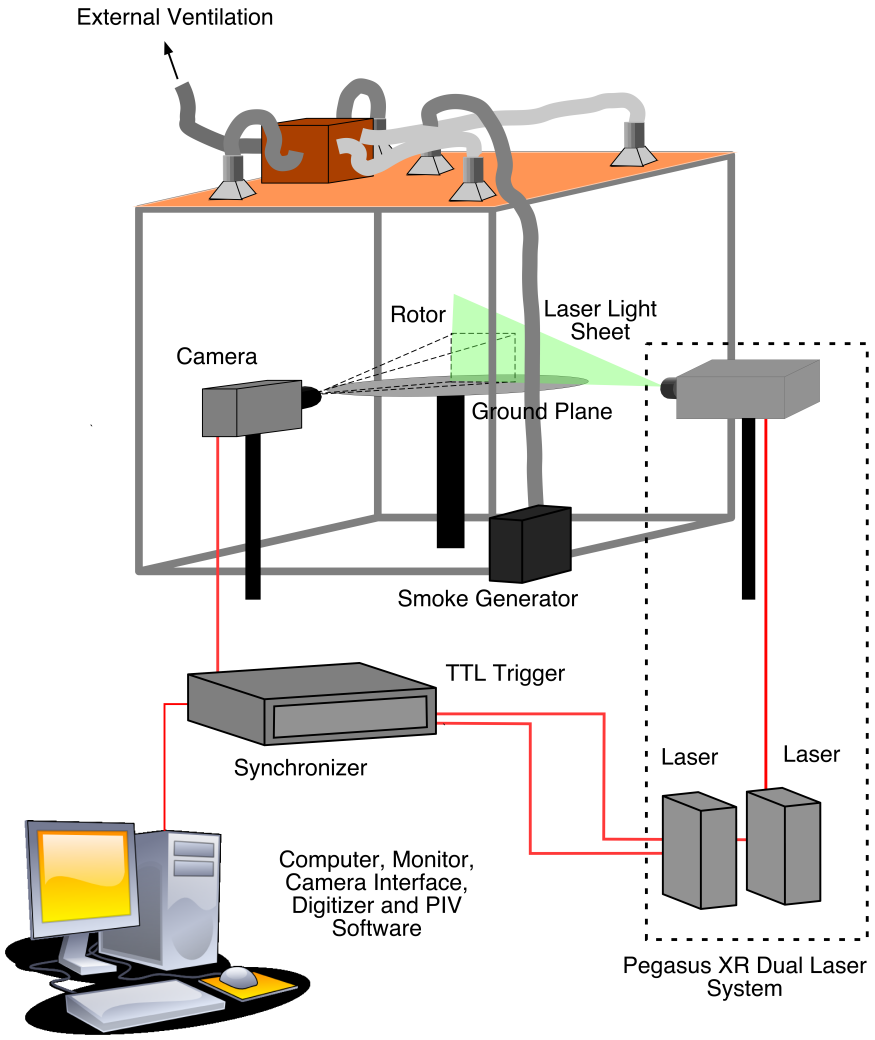

Figure 2.2: Schematic showing the overall experimental setup.

chamber was a cube of dimensions 2 × 2 × 2 m (6.5 × 6.5 × 6.5 ft), giving a rotor radius-to-chamber size ratio of 24, which was also large enough to prevent any significant flow recirculation effects in the chamber during the present experiments.

The flow visualization (FV), particle image velocimetry (PIV), and particle tracking velocimetry (PTV) measurements used a dual 10 mJ/pulse Nd:YAG laser. The laser beam was passed through a series of cylindrical lenses to convert the beam into a diverging light sheet, and then

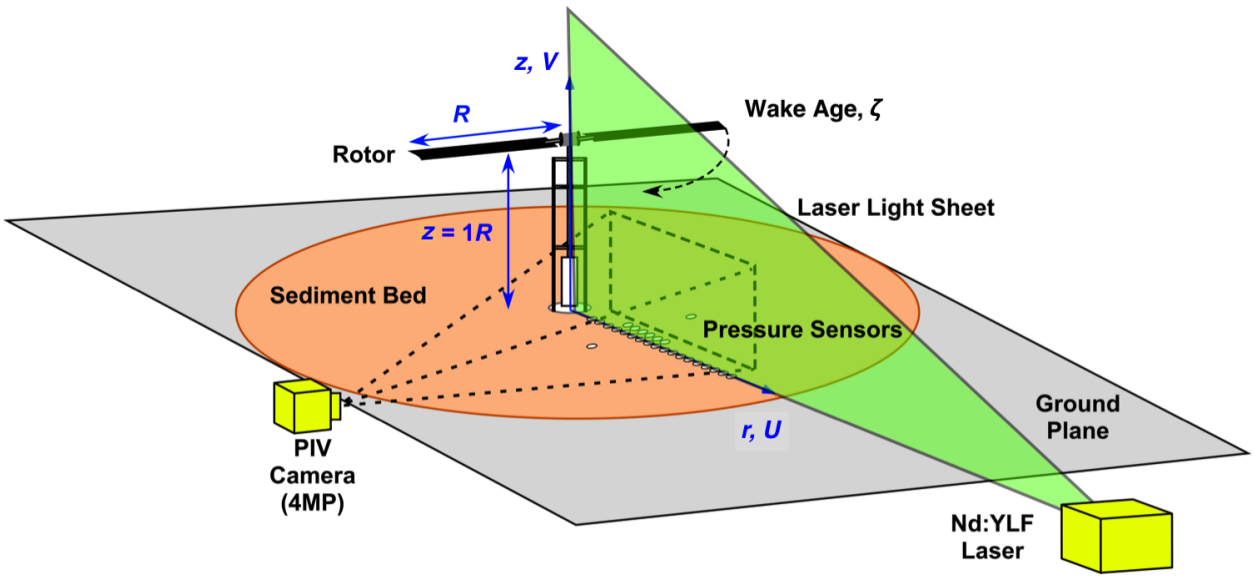

Figure 2.3: Schematic of the orientation of the system components used for the flow measurements.

through a spherical lens to thin the light sheet. A high-speed 4-megapixel CMOS[1] camera was oriented such that its viewing axis was orthogonal to the plane of the laser light sheet; see Fig. 2.3.

For the flow experiments, the air was seeded with submicron smoke particles to highlight and track the individual flow structures, as well as to visualize the flow field as a whole. The submicron seed particles were produced by a smoke generator. A calibration [60] determined that the seed particles had a nominal diameter of 0.2 μm, which was large enough to produce sufficient Mie scattering of the laser light, but also small enough to faithfully follow the rotor wake flow with the embedded vortices [61–63]. The seed was produced by vaporizing a mineral oil mixture under high pressure nitrogen. This vapor, upon mixing with cooler air after exiting the generator, created a dense white smoke containing the seed particles. Ducts were used to route the smoke to an input vent in the ceiling of the dust chamber, where the seed particles passed through a plenum and honeycomb vanes to help to remove turbulence before the flow entered into the test section.

[1] Complementary Metal Oxide Sensor.

Dual-phase flow experiments were performed by using a bed of soda-glass microspheres distributed over the ground plane. These particles were well characterized with respect to their size (45–63 μm in diameter) and mass density (1,300 kg m^{-3}) [64]. The particles were loosely deposited over the ground plane to a thickness of 12.7 mm (0.5 in), and the surface was leveled using a scraper. The particle bed needed to be sufficiently thick to ensure that any erosion produced by the rotor wake would not significantly deplete the bed within the short duration of the tests.

2.1.3 Pressure Measurements on the Ground Plane

Measurements of the surface pressures on the ground plane beneath the hovering rotor required that the plane be fitted with pressure transducers. These sensors had to be sensitive enough to measure the relatively small pressures produced by the small-scale rotor (on the order of 50 N m^{-2}). In this case, a circular ground plane (plate) of 0.912 m (3 ft) radius was constructed. The plate was made from plywood and reinforced with wooden supports. Small holes of 2 mm (0.08 in) diameter were drilled along a radial line on the plate, below which differential pressure transducers were mounted. The row of 32 transducers extended from 0.6–4.1 R along the ground plane; see Fig. 2.4.

The spacing between pressure sensors was 13 cm (0.15 R), which was the minimum possible spacing when placing the transducers flush and adjacent to each other. A staggered arrangement was used to reduce the spacing of the sensors to 7 cm (0.08 R) to give greater spatial resolution in the 1–2 r/R region of the ground plane, which is where the impingement of the rotor blade tip vortices was expected. Because differential transducers were used, a sealed plenum was installed

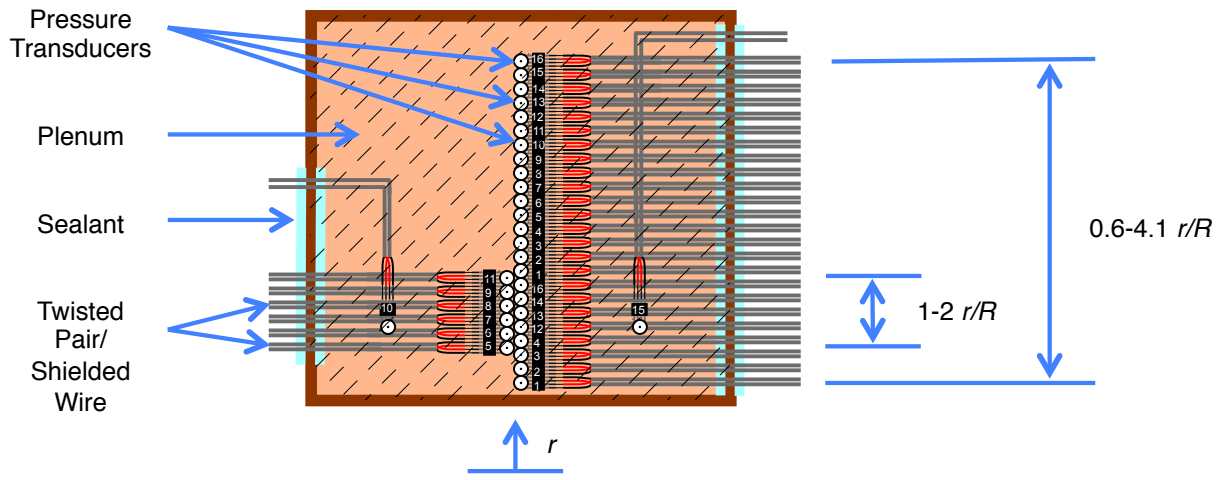

Figure 2.4: Schematic of the sealed plenum housing the sensors, which was on the back of the ground plane.

to enclose the entire row of transducers and reference one side to ambient pressure conditions. To avoid confusion with the rectangular ground plane used for the flow measurements, this second ground plane will hereafter be referred to as the "pressure plate."

The pressure transducers required 12 Volts of excitation, which was provided by a DC voltage source powered by an uninterruptable power supply (UPS) to minimize the introduction of 60 Hz electrical noise that is inherent in the mains power. A terminal block distributed the power to multiple sensors simultaneously. Twisted and shielded pair wires were utilized throughout the system to reduce signal crosstalk and noise. The signal wires were routed from the appropriate pins on each transducer, through the plenum to the terminal blocks; see Fig. 2.5. The outputs from the transducers were connected to a bank of offset circuits, which was used to remove the DC voltage offset from each of the pressure signals.

Figure 2.6 shows a diagram of the offset compensation circuit, which utilized precision operational amplifiers to minimize electrical noise. The signal was then passed on to a Signal Con-

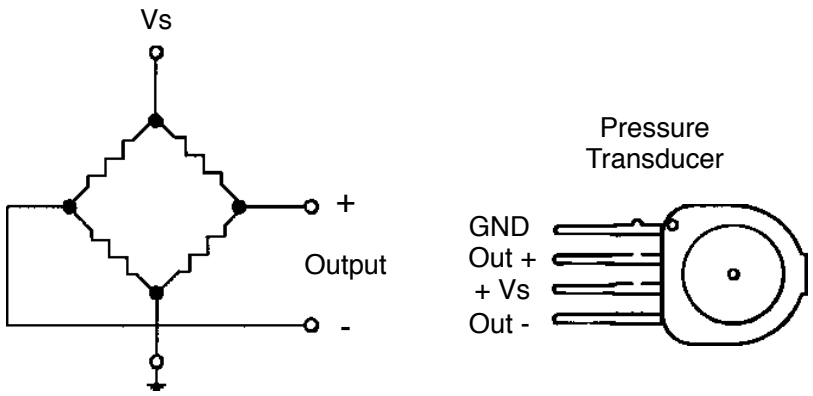

Figure 2.5: Schematic of the pin in/out and the Wheatstone bridge nature of the pressure sensors.

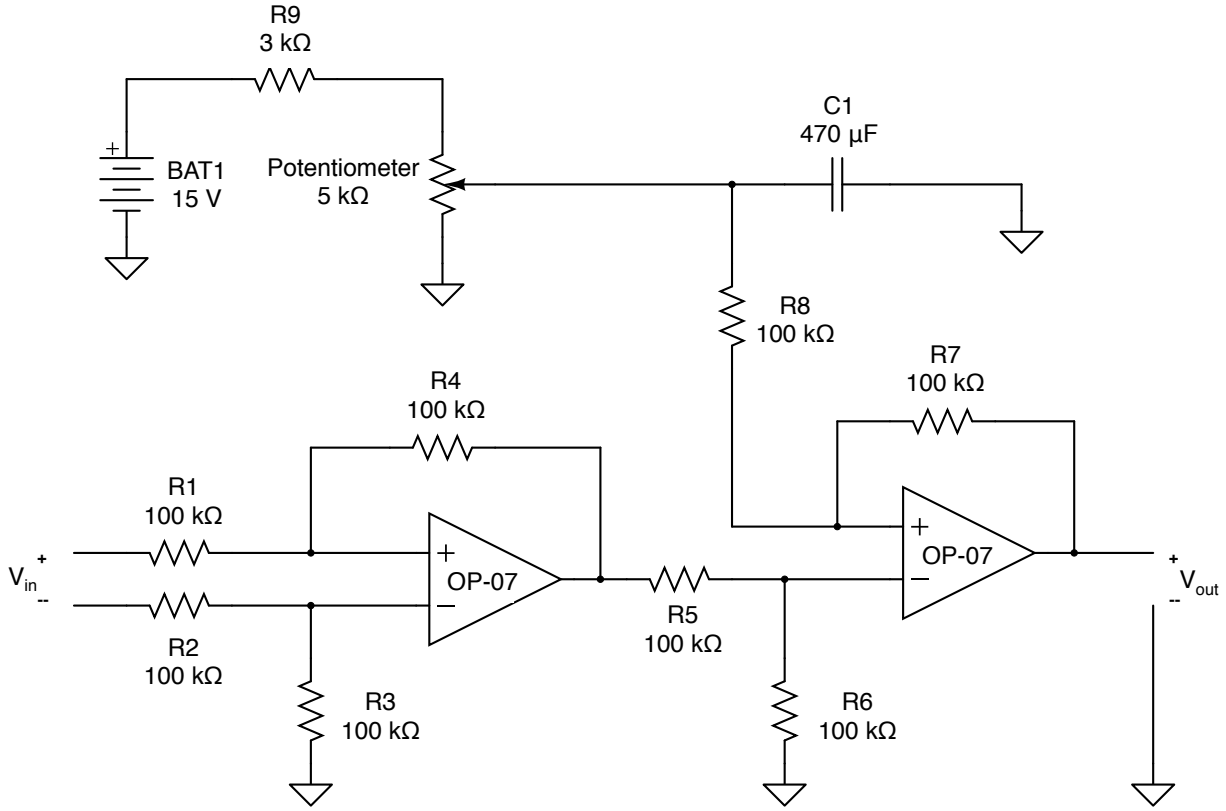

Figure 2.6: Diagram of the circuit used to remove DC voltage offset from the pressure transducer output signals.

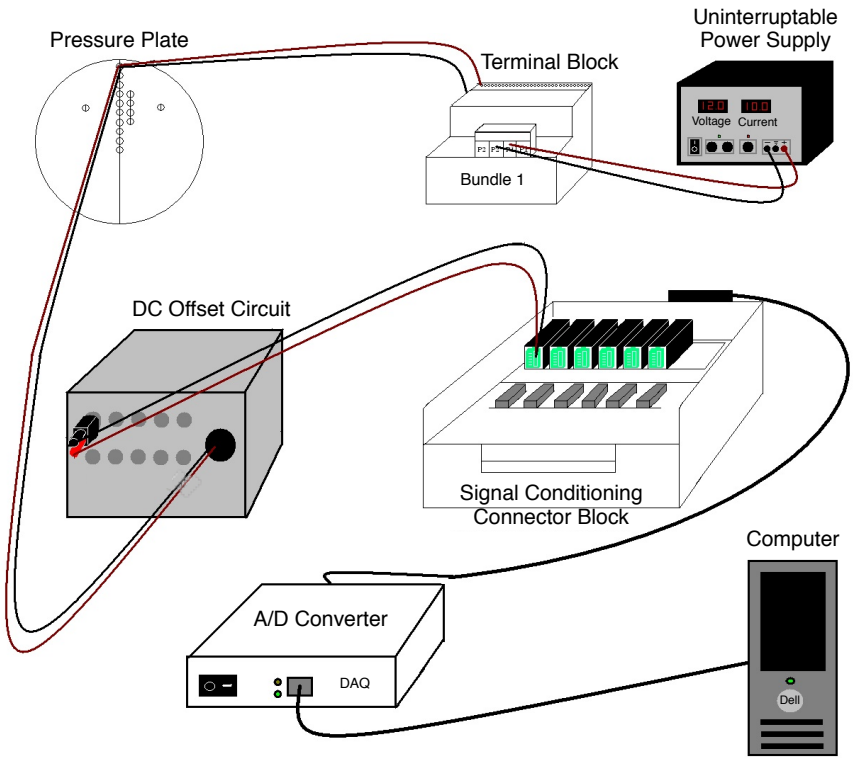

Figure 2.7: Schematic of the pressure measurement system.

ditioning Connector Block (SCCB), fitted with input modules. The full-bridge configuration of these modules provided a signal gain of 100 and amplified the small signal. Because the SCCB only featured 16 connections for the analog-input SCC modules, the 32 pressure transducers were separated into two bundles and so pressure measurements were obtained first for one bundle and then for the other. The analog signal was then converted to digital form via an analog-digital converter (A/D) on a Data Acquisition (DAQ) card.

The data acquisition process was conducted using a LabView™ virtual instrument (VI). The VI was written to trigger the data acquisition and to apply transducer-specific calibration factors to convert voltages to engineering units of pressure (lb ft^{-2}) before displaying data on the monitor and also writing it to a data file. Figure 2.7 summarizes the pressure measurement system.

2.2 Experimental Techniques

To evaluate any correlation between the vortex wake-induced pressure and particle mobilization, both the fluid dynamics of rotor wake-ground interactions and the time-history of the pressure field on the ground had to be measured. Such measurements could, unfortunately, not be conducted simultaneously and required a series of separate experiments.

2.2.1 Time-Resolved Flow Visualization (TR-FV)

Time-resolved flow visualization (TR-FV) was used to first to examine the processes of sediment mobilization and uplift from the ground and sediment bed under the influence of the blade tip vortices. The experiments were performed for both the single-phase and dual-phase cases, i.e., with and without sediment particles. The seed was introduced into the dust chamber and strategically routed via ducting to an area near the rotor where the small seed particles would be ingested and trace out the flow structures of the rotor wake. In this case, the laser sheet was pulsed at a relatively high frequency of 1,000 Hz to illuminate the flow field. Simultaneously, the high-speed camera captured a series of images to create a time-history of the evolving flow field. Image capturing was manually triggered after giving time for the smoke to travel to the chamber and for any transients in the flow to dissipate.

2.2.2 Pressures on the Ground Plane

Measurements of unsteady pressure on the ground plane for the same rotor operating conditions and flow conditions were then made. The transducers were powered-on for several hours

prior to taking any measurements to allow time for the transducers to reach their thermal equilibrium so as to reduce any thermal drift that could bias the output signals. To verify that thermal equilibrium had been reached, a zero test was performed before any data were recorded. This test involved triggering acquisition with the rotor stopped to record the outputs from the transducers. After having confirmed the zero had no drift, a relative zero test was performed. For this test, the motor was spinning but the blades were removed from the hub. The purpose of this test was to ensure that there were no changes in the signal from motor noise or from vibrations. The resulting zero tares were then subtracted from the subsequently recorded pressure measurements.

To obtain surface pressure measurements on the ground, the blade (or blades) were secured in the hub and were spun up to the desired rotational frequency. After allowing a few seconds for the frequency to stabilize, data acquisition was triggered via LabView™. This process was repeated to obtain ten data sets in succession, each having a one second duration (i.e., 110 or 130 rotor revolutions, depending on the rotor frequency). The entire process was then repeated for the other bank of 16 pressure transducers. The two data sets were then combined.

2.2.3 Time-Resolved Particle Image Velocimetry (TR-PIV)

To measure the evolving velocity field in the rotor wake, time-resolved particle image velocimetry (TR-PIV) was performed. This laser-based, non-intrusive method provided quantitative measurements of the instantaneous velocity field in the flow. For the present research, the air was seeded with tracer particles (as previously described) and illuminated by a thin laser light sheet, while a high-speed camera captured image pairs of the rotor wake at fixed intervals of blade rota-

tion ($\Delta\psi = 65^\circ$ in the present case) to provide a time-history of the flow field. This interval (65°) was the minimum $\Delta\psi$ resolution possible because of frame rate limitations of the camera (727 Hz) while recording image pairs.

To generate a velocity vector field from these image pairs, each frame was divided into a grid of equally-sized interrogation windows. A cross-correlation [65–67] was performed using windows from frames A and B to identify the displacements of the tracer particles. Combining this particle translation information with the known Δt between frames and the magnification factor of the camera lens, a single resultant velocity vector was calculated for each window; see Fig. 2.8. These individual velocity vectors were then plotted together to produce a realization of the entire velocity field.

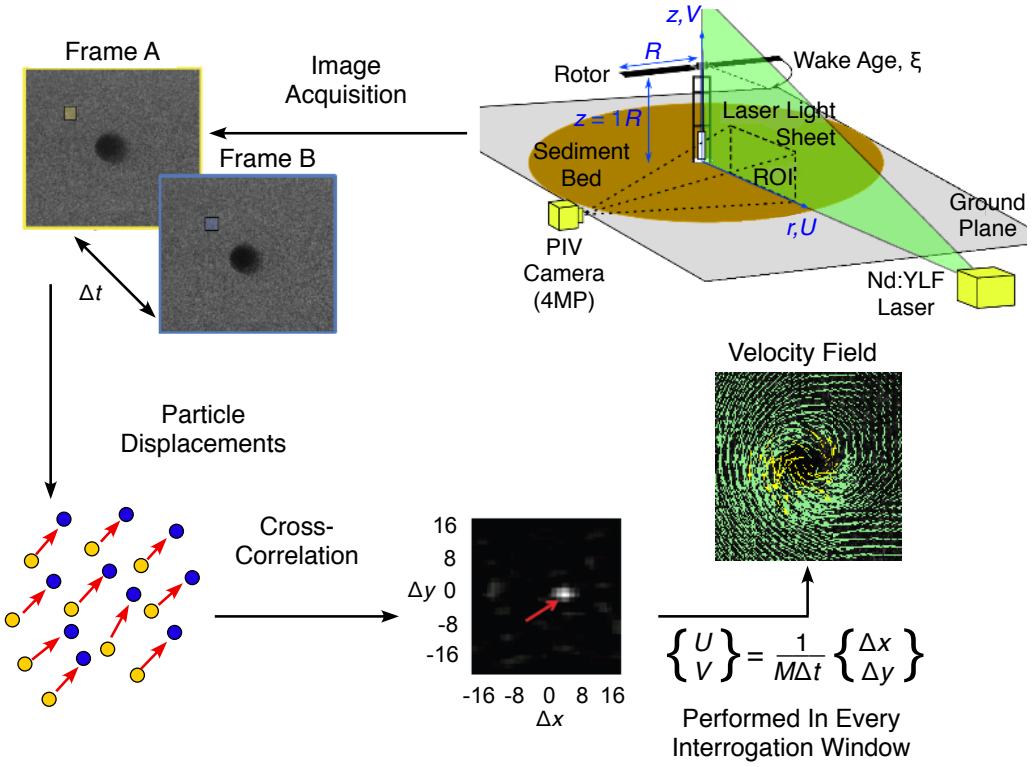

Figure 2.8: Visual representation of the algorithm used in the PIV analysis.

Because higher image density (more particles) yields a better signal-to-noise ratio (SNR), the size of the interrogation windows was chosen such that each window contained about 5–15 seed particles. The seed particles therein translated mostly in one direction from frame A to frame B, with in-plane displacements of approximately one quarter the window length and with out-of-plane displacements of less than one quarter the light sheet thickness [65]. The present work used a multi-pass method of processing in which the interrogation window size began using 32×32 pixels and then was decreased to 16×16 pixels. The windows had a 50% overlap, and equal weight was assigned to all pixels. From a spatial calibration image, which captured a scale positioned in the plane of the light sheet, a conversion factor from pixels to engineering units was obtained.

For each frame, the portion containing flow information was selected, and all vectors outside that region were forced to zero. In addition to reducing computational time, this process, called masking, suppresses spurious information introduced by laser reflections along the ground plane or sediment bed; see Fig. 2.13.

For the dual-phase experiments, an intensity threshold was used to first separate the reflections of the carrier phase (i.e., the tracer smoke or seed particles) from those of the dispersed phase (i.e., the mobilized particles from the bed). Pixel intensities that exceeded the threshold value were forced to zero, essentially subtracting the brighter sediment particles from the image while the carrier phase remained for further analysis.

Post-processing techniques, such as thresholding and filters, were also applied to the velocity vector field. A four-pass regional median filter was implemented for filter regions sized 3×3, the center vector of which was removed if its velocity differed by more than twice the root mean

square (RMS) of the velocities of its neighbors. A universal outlier detection was also enforced for the 3×3 filter regions, which rejected vectors with a residual greater than 2. Any empty space resulting from the removal of a deficient vector was filled by interpolating values based on neighboring vectors.

2.2.4 Particle Tracking Velocimetry (PTV)

To find the locations and velocities of the sediment particles, particle tracking velocimetry (PTV) was used. Because the dispersed-phase contained particle concentrations that were much less dense than that of the carrier-phase, a cross-correlation method could not be used. Instead, the translations of individually identified particles were tracked through the flow.

The isolation of the sediment particles from the background flow (also called phase separation) was achieved by imposing an intensity threshold for image binarization, i.e., pixels with intensity ≥ 1000 were considered to be part of the dispersed phase. Singular particles were restricted to a diameter range of 2–8 pixels. Clusters of pixels meeting or exceeding the intensity threshold were evaluated for 8-point connectivity, which grouped not only the neighboring pixels to the left, right, top, and bottom, but also any diagonal pixels of sufficient intensity, as shown in Fig. 2.9. The conditions for identification across the entire group of particles included a maximum distance of 30 pixels between particles and a maximum of 8 neighbors per particle.

To find the best-fit ellipse for an identified particle, the PTV algorithm considered the centroid of the pixel cluster, the mean grey value of all pixels in the cluster, the shape of the pixel cluster, and Feret's diameter (or the longest distance between any two points along the boundary

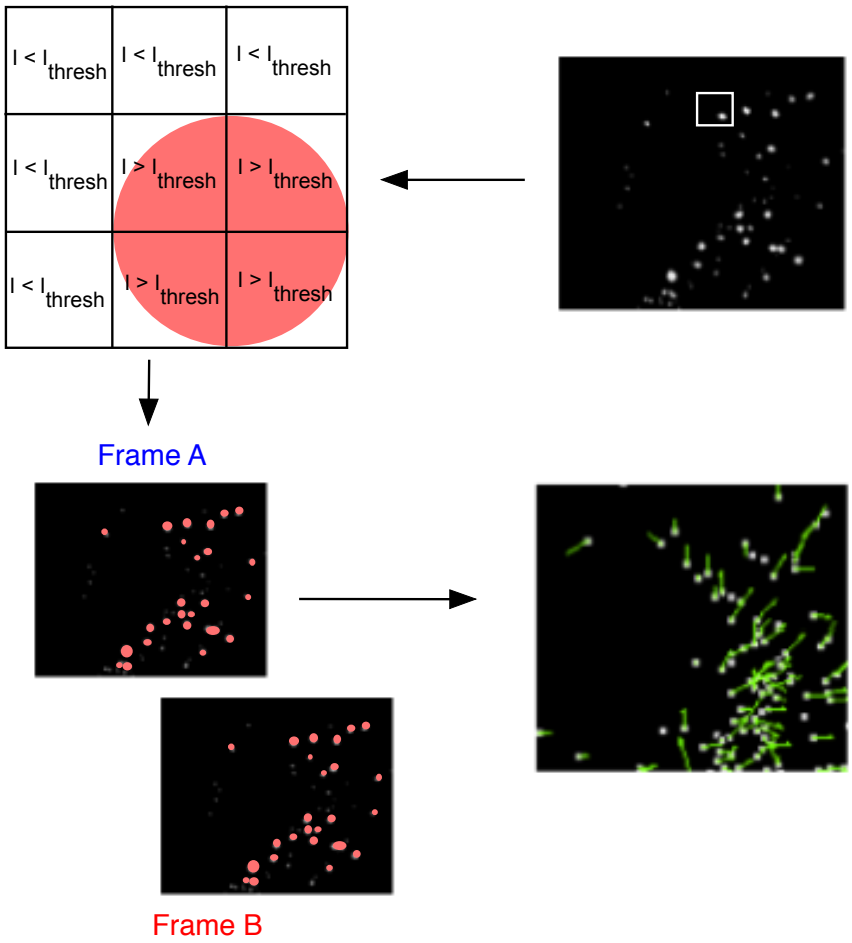

Figure 2.9: Visual representation of particle identification in the PTV.

of the pixel cluster). Each particle ellipse was defined by a major axis, a minor axis, and the angle between the major axis and the abscissa.

Once the particle identification was completed for a pair of images, the PTV algorithm attempted to locate each particle from frame A at its new location in frame B. Particles in frame B nearest to the original location of a frame A particle were considered as potential candidates for a match. Candidate particles were evaluated for percentage size differences, with a match requiring a size difference of 100% or less as compared to the original size of the particle in frame A.

Shifts of 3–4 pixels in either the horizontal or vertical direction were considered to be plausible translations of a particle location between frames A and B. Any particle from frame A that failed to be identified in frame B was considered to have moved out of the plane of the laser sheet. Such particles were assigned a zero in-plane velocity and were ultimately removed from the PTV data set during the post-processing.

2.3 Region of Interest (ROI)

All of the experiments described above were conducted for the same region of interest (ROI). The flow field was examined from 0.5–4.2 r/R over the ground plane, as shown in Fig. 2.10. The PIV and PTV experiments were conducted for a rotor height of one radius off the ground, while the FV experiments (part of the scoping study) were performed at three rotor heights of 0.5, 1.0, and 1.5 z/R.

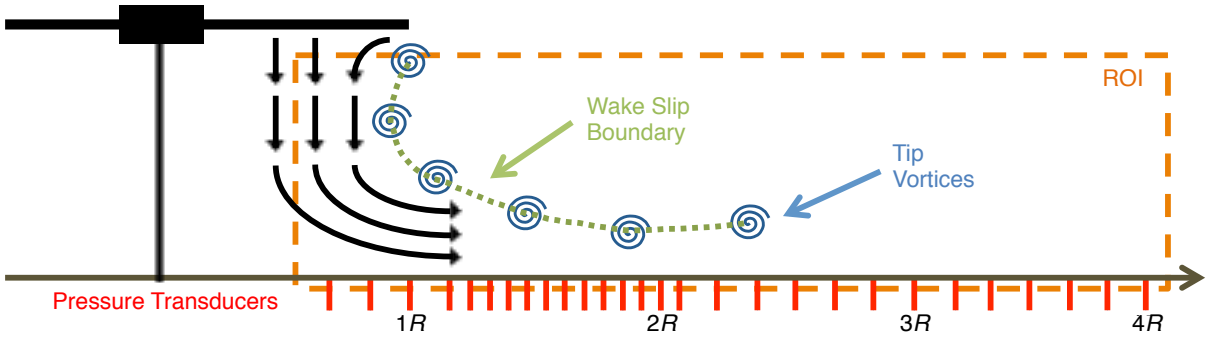

Figure 2.10: Schematic showing the region of interest (ROI) for all experiments, as well as the locations of the pressure measurements.

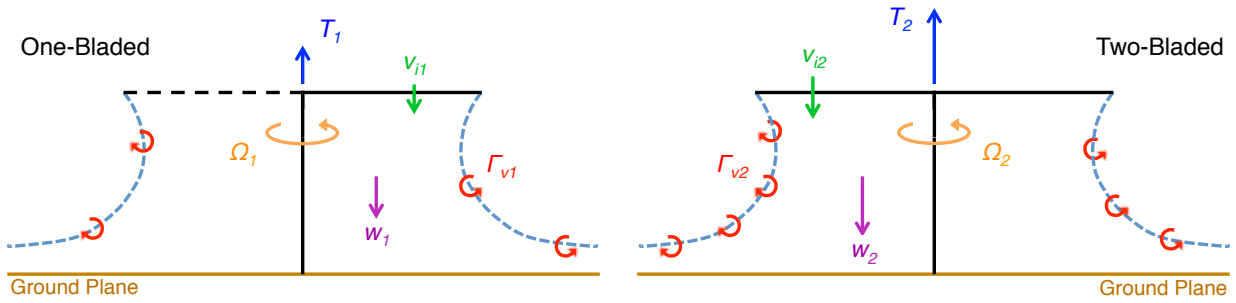

Figure 2.11: Schematic comparing the general nature of the one-bladed and two-bladed rotor wake flow fields.

2.4 Rotor Operating Conditions

Brownout is a dual-phase flow problem, so to better understand the problem both single-phase (carrier phase only) and dual-phase experiments (both the carrier and dispersed phases) were performed for all test conditions, with the exception of the pressure measurements on the ground plane. Pressure experiments were not possible with the sediment bed present because the small particles would fall into the pressure ports and affect the readings.

Experiments were performed in both the one-bladed and two-bladed rotor configurations. To facilitate a comparison between the flow measurements for each rotor, the blade loading coefficient (C_T/σ) was held constant for all experiments. To understand this decision, consider Fig. 2.11. The rotor slipstream velocity (w) depends on the thrust (T), the air density (ρ), and the rotor disk area (A). The air density and the rotor disk area are the same for both the one-bladed and two-bladed rotors. Therefore, the rotor slipstream velocity would only be different for each rotor if they were to be operated at different values of thrust, i.e.,

$$w = 2v_i = \sqrt{\frac{T}{2\rho A}} \tag{2.1}$$

The tip vortex strength (Γ_v) depends on the ratio of the thrust coefficient (C_T) to rotor solidity (σ), the rotational frequency (Ω), the rotor radius (R), and chord of the blade (c). All experiments were performed while operating the rotors at the same rotational frequency with blades of equal radius and chord. Therefore, the strength of the vortices [68] produced by each rotor will be equal unless C_T/σ varies, i.e.,

$$\Gamma_v = 2\left(\frac{C_T}{\sigma}\right)\Omega R c \tag{2.2}$$

The thrust coefficient, C_T, as used in the previous equation, depends on the rotor thrust, the disk area, the rotational frequency, and the rotor radius, i.e.,

$$C_T = \frac{T}{\rho A(\Omega R)^2} \tag{2.3}$$

As already stated, the radius and disk area are the same for both the one-bladed and two-bladed rotors, and they were operated at the same rotational frequency for all experiments. This means that the thrust coefficient would be directly proportional to any difference in thrust between the two rotors.

The rotor solidity, σ, is the ratio of rotor blade area to rotor disk area, i.e., for rectangular blades of chord c,

$$\sigma = \frac{N_b c R}{\pi R^2} = \frac{N_b c}{\pi R} \tag{2.4}$$

While the blades used for both rotors are identical in dimensions and the disk areas are the same, the two-bladed rotor has twice the blade area of the one-bladed rotor because it has twice the number of blades (N_b).

To allow for the comparison of measurements obtained from both rotors, each rotor must be operated at conditions that produce vortices of nominally equal strength, i.e., equal circulation, Γ_v. From the relationships described above, it is clear that rotors of different thrust cannot generate the same rotor induced velocity, or thrust coefficient. Because the vortex strength depends on the ratio of thrust coefficient to rotor solidity (C_T/σ), and because rotors having different numbers of blades with the same chord cannot have the same rotor solidity (σ), one way of achieving the goal of equal vortex strengths is to adjust the thrust of each rotor such that the change in thrust offsets the increase in blade number. Therefore, the decision was made to operate the two-bladed rotor at twice the thrust of the one-bladed rotor for the present research, i.e.,

$$C_{T2} = 2C_{T1} \tag{2.5}$$

Because the two-bladed rotor is operating at twice the thrust, its rotor slipstream velocity will be 41% higher than that of the one-bladed rotor, i.e.,

$$w_2 = \frac{1}{\sqrt{2}} w_1 \tag{2.6}$$

Now,

$$\sigma_2 = 2\sigma_1 \tag{2.7}$$

This outcome satisfies the desired relationship for rotor vortex strengths and facilitates the comparison of the measurements, i.e.,

$$\Gamma_{v2} \simeq \Gamma_{v1} \tag{2.8}$$

if ΩR is the same.

Initial flow visualization tests were conducted over a range of operating conditions, which included measurements at the three rotor heights, two rotational frequencies (110 Hz and 130 Hz or 6,600 rpm and 7,800 rpm), and also for the one-bladed and two-bladed rotors. For the lower rotational frequency, the tip speed ($V_{\text{tip}} = \Omega R$) was 58.1 m s^{-1} and the tip Reynolds number (Re_{tip}) was approximately 70,000. However, operating the rotor at the higher tip speed of 68.6 m s^{-1} meant Re_{tip} increased to just above 80,000. For the flow visualization, a total of 500 images were captured at a rate of 1,000 frames per second.

The FV measurements were repeated for both the one-bladed and two-bladed rotors operating at 130 Hz and a height of z/R = 1. Dual-phase FV experiments were also conducted for the same operating conditions. The higher rotational frequency increased flow velocities and strengthened the pressure response. For these tests, 1,000 images were recorded at 727 frames per second.

The surface pressure measurements on the ground plane induced by the one-bladed rotor were first taken at the three rotor heights above the ground and at the two rotational frequencies. Pressure measurements were also obtained for the two-bladed rotor at a height of $z/R = 1$ and for both rotational frequencies. The pressure signals were sampled at a rate of 95 kHz to give a total of 95,000 samples, which was the best attainable resolution as limited by the buffer of memory.

PIV and PTV were also conducted for the one-bladed and two-bladed rotors when operating at 130 Hz, again for a rotor height of $z/R = 1$. For these cases, a total of 1,000 images were recorded at 727 frames per second, which was the maximum frame rate of the camera while still being able to capture image pairs. In the PIV/PTV, image frames A and B were separated by 15 μs, and the time step between pairs was 1.4 m sec.

2.5 Technical Challenges

Each of the four types of experiments presented its own variety of technical challenges. This section describes the issues encountered and how each one was addressed.

2.5.1 Flow Visualization (FV)

To visualize all of the relevant flow structures, the smoke (seed) used for the flow visualization must be ingested far enough inboard along the rotor to seed the wake sheets but also far enough outboard to seed the center of the tip vortex. The ducting used to introduce the seed to the dust chamber was adjusted between tests to optimize the seed placement and entrainment into the rotor wake.

Another difficult process to master was the timing of image captures. A few seconds of delay between the manual triggering of smoke delivery and image capture was necessary to allow time for the smoke to be ingested by the rotor and to fully trace the wake flow structures. Too long a delay, however, caused the smoke to disperse, thereby producing less contrast in the FV images. With experience, the timing of these events could be optimized to produce the best possible FV results.

2.5.2 Surface Pressures on Ground Plane

One of the most challenging aspects of the present work was to resolve the small pressure measured by the sensors. Efforts to reduce electrical noise on the signals included using twisted pair and shielded wires, properly grounding all components, using an UPS in an attempt to avoid 60 Hz electrical noise, and installing low noise operational amplifiers in the electrical circuits.

Some electromagnetic interference from the magnet on the rotor shaft was discovered, as well as from the electric motor driving the rotor. Because the motor controller offered a speed-governing option via the supply current, the magnet could be removed after first being used to determine the electrical current needed to produce a given rotational frequency. The electrical noise was further reduced by creating a grounded shroud around the motor mount housing and by inverting the rotor assembly to increase the distance of the motor from the sensors; see Fig. 2.12. Finally, a digital low-pass filter, with a cut-off frequency of 1,500 Hz, was applied during post-processing to remove any remaining high frequency noise. This value for the cut-off frequency was sufficiently large so as to preserve the higher frequency harmonics produced by the rotor, while also suppressing very high frequency electrical noise that would otherwise obscure the nature of the measured waveform.

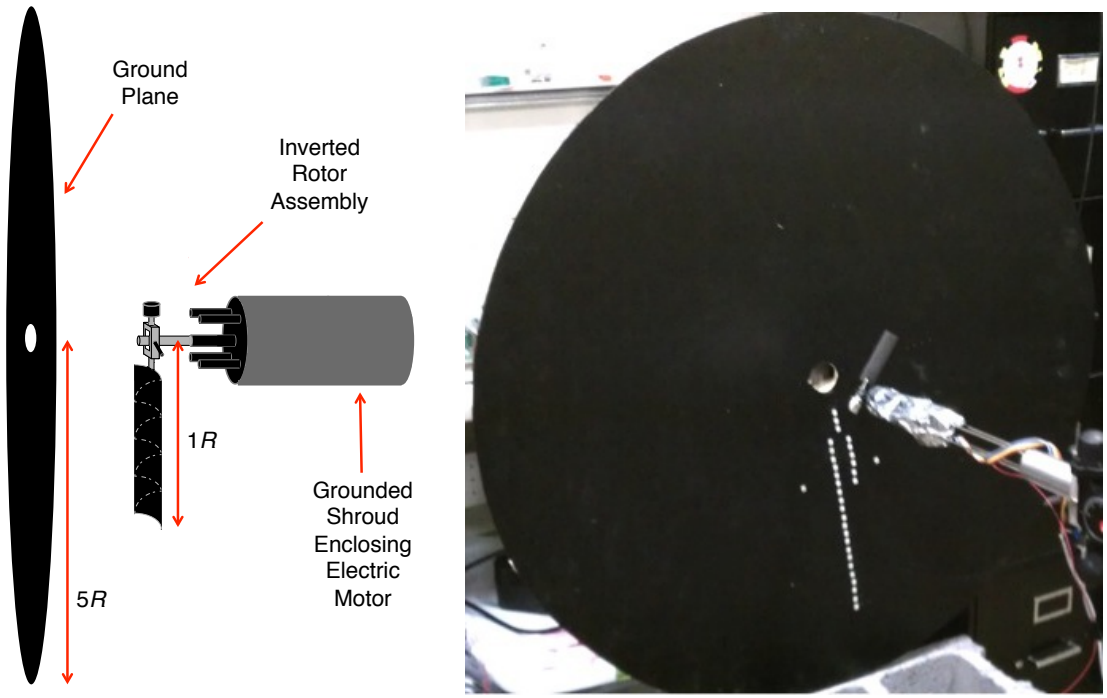

(a) Schematic, **not drawn to scale** (b) Actual setup

Figure 2.12: The inverted rotor orientation and grounded aluminum shroud that was used to minimize noise from the electric motor while recording the pressure measurements.

2.5.3 Particle Image Velocimetry (PIV)

Even though the ground plane and rotor mount were painted black, laser reflections remained an issue. Judicious alignment of the laser such that the light sheet just barely skimmed the ground plane in the ROI helped to minimize such reflections. However, some reflections were inevitable. Therefore, PIV post-processing techniques such as masking and background subtraction were needed to further reduce the reflections in the raw PIV images; see Fig. 2.13.

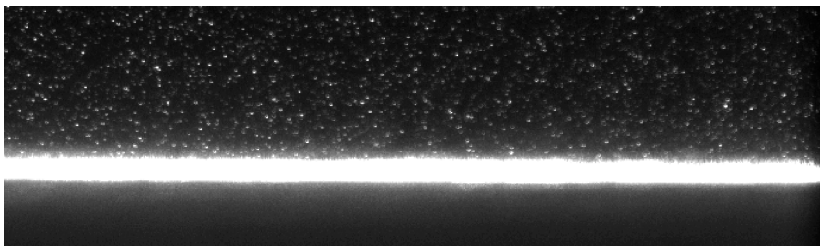

(a) Unaltered raw image.

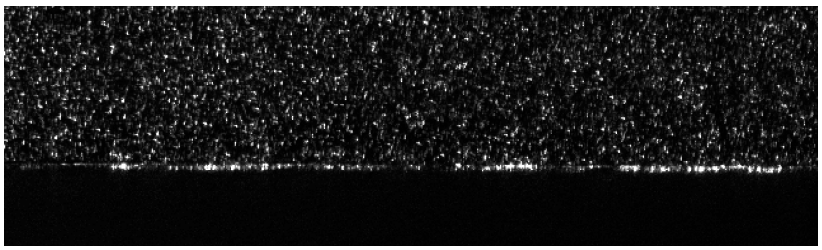

(b) Image taken after judicious laser alignment.

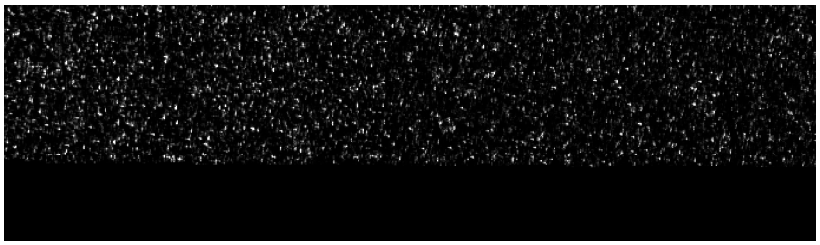

(c) Image after background subtraction and image masking.

Figure 2.13: Methods to minimize surface reflections of the laser sheet at the ground plane.

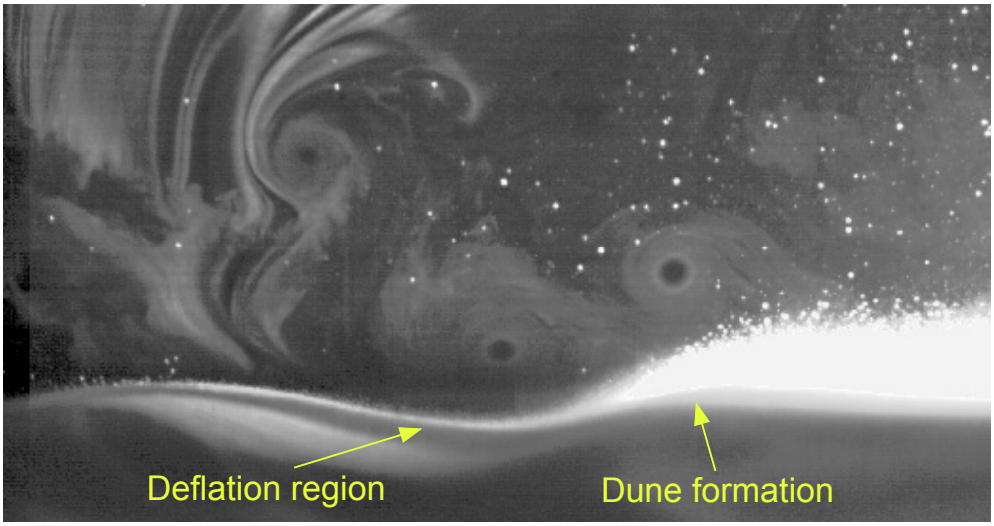

Figure 2.14: FV image showing the deflation and dune regions that can form on the sediment bed after the rotor has been in operation for some time.

The resolution possible with a 4-megapixel camera comes at the price of relatively large files sizes. Many large files were required to provide a time-history of a duration sufficient to study the unsteady nature of the rotor flow field. Data storage issues were resolved by periodically transferring data over the network to archival drive systems.

Processing large quantities of data can also be time-consuming. Some computationally less expensive processing settings were selected, such as using a cyclic FFT-based algorithm for the correlation function and by choosing a square 1:1 equal weighting of pixels. Also, the use of a geometric mask while processing saved computational time by forcing all flow velocities outside of the mask to be set to zero.

Figure 2.14 shows how the impingement of the rotor wake on the particle bed can erode the bed over time. For the duration of the experiments in the present work, a bed thickness of 1.3 cm (0.5 in) was found to be acceptable. Image capture was triggered after rotor spin-up, as soon as

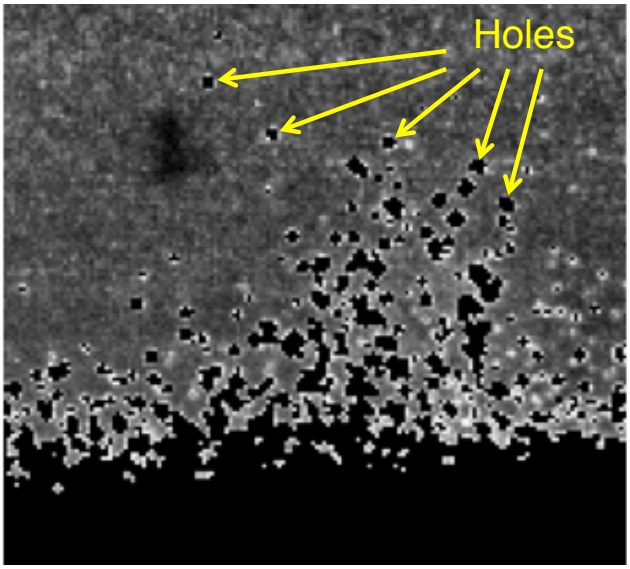

Figure 2.15: Processed image showing the "holes" that can result from separation of the particle (dispersed) phase from the carrier phase.

seeding conditions would allow, in an attempt to record all of the needed data before the surface topology of the particle bed was changed.

Another challenge was separating the dispersed (particle) phase from the carrier phase, which can leave "holes" in the image where information needed to calculate the velocity field for that region of the carrier phase is no longer present; see Fig. 2.15. To resolve this latter issue, a simple 3×3 interpolation grid was used to approximate missing data, which then allowed for successful cross-correlations of the carrier phase images.

2.5.4 Particle Tracking Velocimetry (PTV)

Performing PTV also requires addressing the challenges of laser reflections and bed erosion, besides the issue of sediment particle identification. Operating the rotor at high speed generated a dense cloud of airborne particles. Because of regions of particle over-saturation (see Fig. 2.16 for

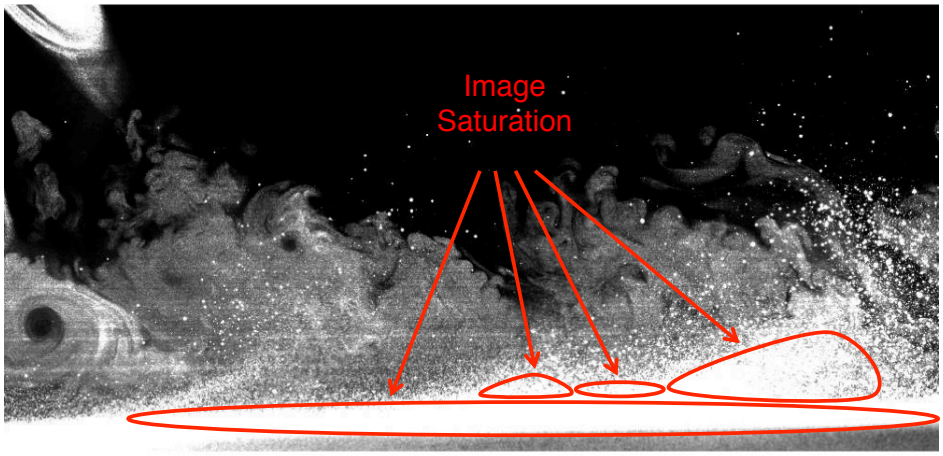

Figure 2.16: Dual-phase FV image showing image over-saturation caused by too many uplifted and suspended particles.

an example of this) and limitations of the particle identification algorithm, only particles near the periphery of the cloud were distinguishable and so able to be accurately tracked. Several iterations of the PTV processing were conducted to determine the best combination of algorithm settings (maximum number of neighbors, circularity, and Feret's diameter, etc.) so as to capture as many identifiable particles as possible, while also attempting to minimize false particle identifications within the bulk of the particle cloud.

2.6 Error and Uncertainties

While PIV and PTV are known to be able to accurately quantify the flow velocity fields, there are several potential sources of error and uncertainty. The experimental setup itself, or even the selection of processing parameters within the software algorithm, can decrease the accuracy of the measured data.

2.6.1 Particle Image Velocimetry (PIV)

While the smoke tracer particles used for this study were in the sub-micron size, the seed particles may sometimes slip or fail to trace the flow perfectly, which would manifest as error in the measured velocity. The path of the tracer particles may be altogether indistinguishable if the Mie scattering of laser light is insufficient to resolve the particle or too great as in the case of over-saturation. Over-saturated regions of the image obscure the tracer particle information and can lead to erroneous flow vectors.

The method of calibration can introduce some uncertainty in the measurements. The finite resolution of the camera limits the accuracy with which two points can be selected for spatial calibration. However, the error in velocity from the calibration is generally insignificant, so long as best practices are followed.

Uncertainty is produced from the magnification of particle images. Errors from magnification are proportional to the ratio of the distance from the lens to the image (z_i) and the distance from the lens to the object (Z_0), i.e.,

$$M_0 = z_i / Z_0 \tag{2.9}$$

Considering the laser light sheet to be a plane of finite thickness, the relative difference of the magnification on the back of the laser plane compared with the center of the laser plane provides an error that is proportional to the laser sheet thickness divided by the object distance [69]. This magnification error is usually very small, but can be significant if the laser sheet is more than 1 mm (0.04 in) thick. In the present work the laser sheet thickness was approximately 1mm thick.

Wide viewing angles of the flow field and the out-of-plane motion of tracer particles can

introduce perspective error. Perspective error is a relative error between the true displacement on the object plane and the apparent in-plane displacement, quantified by Prasad's equation [69], i.e.,

$$\varepsilon = \sqrt{\left(\frac{\Delta y}{\Delta r}\tan(\theta_r)\right)^2 + \left(\frac{\Delta y}{\Delta z}\tan(\theta_z)\right)^2} \tag{2.10}$$

where ε is the relative error from perspective, Δy is the out-of-plane displacement, Δr and Δz are in-plane displacements, and θr and θz are the respective angles for a position in the field of view, as referenced from center. Images obtained with a wide angle lens, as well as images obtained at high magnification, will have elevated perspective error, which is influenced by the camera distance from the laser sheet and the laser sheet thickness. In the present work, the light sheet was sufficiently thin and the camera was sufficiently close so as not to produce any significant perspective error within the measurements.

Finite resolution can also introduce errors as it affects the spatial averaging of the velocity fluctuations. Different fields of view can produce nearly identical mean velocities, but the fluctuation levels will be higher for smaller fields of view [69]. Within any field of view, care must be taken to choose an interrogation window size that is greater than or equal to the light sheet thickness. The laser pulse separation time, Δt, must also be carefully considered; too large an interrogation window and/or too much elapsed time between pulses can increase errors from flow curvature or shearing within a window. A Δt of 50 μs was selected from a range of tested values as a short enough laser pulse separation time to capture the translation of tracer particles without the flow curving substantially in the present experiments.

2.6.2 Particle Tracking Velocimetry (PTV)

In a similar manner to PIV, PTV errors can arise from magnification, calibration, and perspective. Other sources of error in PTV stem from the difficulties of particle identification. If a particle either fails to scatter enough light or is not located fully within the illumination of the laser light sheet, it may go undetected. When comparing image pairs, the algorithm used to search for the strongest correlation peak has a limited accuracy with which it can identify particles and their motion between frames. This issue causes an error in the image position. Parameters selected for the particle identification and tracking, such as maximum number of neighbors, circularity, and Feret's diameter [70], can also introduce errors. Thresholds are set manually for how dense the identified particle field is to be and where and at what rate the particles are moving. Because the requirements and restrictions by which the algorithm will confirm or reject pixel clusters as identified sediment particles are based on manual inputs, the algorithm output has a finite accuracy that is limited by its inputs. To obtain as accurate a result as possible, various values and combinations of these inputs were explored to achieve a PTV result that most satisfactorily identified the clearly visible particle clusters along the periphery of the dust cloud.

2.7 Summary

The present chapter has described the types of experiments that were performed in the present research. Details of the rotor model were described, as well as the ventilated dust chamber, and the ground plane that was fitted with the pressure sensors. The operating conditions for the rotor, as well as the use of the ground plane, laser light sheet, camera, seeding, and sediment particles

were explained for each of the four types of experiments: flow visualization, ground surface pressure measurements, particle image velocimetry, and particle tracking velocimetry. Parameters such as the number of blades (one versus two), height of the rotor disk plane above the ground plane, and the rotational frequency of the rotors were varied to explore their influence on the ground pressure and particle mobilization. An intensity thresholding approach for phase separation allowed the carrier and particle phases to be examined separately. Each experiment presented its own technical challenges, the most difficult being the measurement of the small unsteady pressure values that were induced on the ground plane by the rotor wake. Finally, uncertainties in the PIV were quantified, and sources of error for the PTV were discussed.

Chapter 3

Results

The results from the various experiments that were performed are discussed in the present chapter. The flow visualization (FV) images were first analyzed to understand the rotor wake behavior near the ground for different rotor operating conditions. Then, by comparing the unsteady pressure measurements over the ground plane in conjunction with the FV images, representative pressure signatures were identified that could be correlated to the locations of blade tip vortices before, during, and after their impingement on the ground. From the dual-phase flow results, concentrations of the sediment particles were observed to form in front of and below the cores of the vortices as they convected over the particle bed. To search for evidence of pressure effects on the particles, i.e., body forces, the trajectories of the mobilized particles were compared to the direction of the carrier flow to determine any significant particle deviations.

3.1 Rotor Wake Behavior

As the lifting rotor blades rotate in the hover condition, each blade trails a nominally helicoidal vortex filament. Taking a two-dimensional cut through the helicoidal wake, the vortex filaments appear as individual blade tip vortices, as shown in Fig. 3.1. For a rotor hovering in ground effect, each filament convects axially downward in the flow until it approaches and impinges upon the ground plane beneath the rotor. As the wake nears the ground, its direction changes from

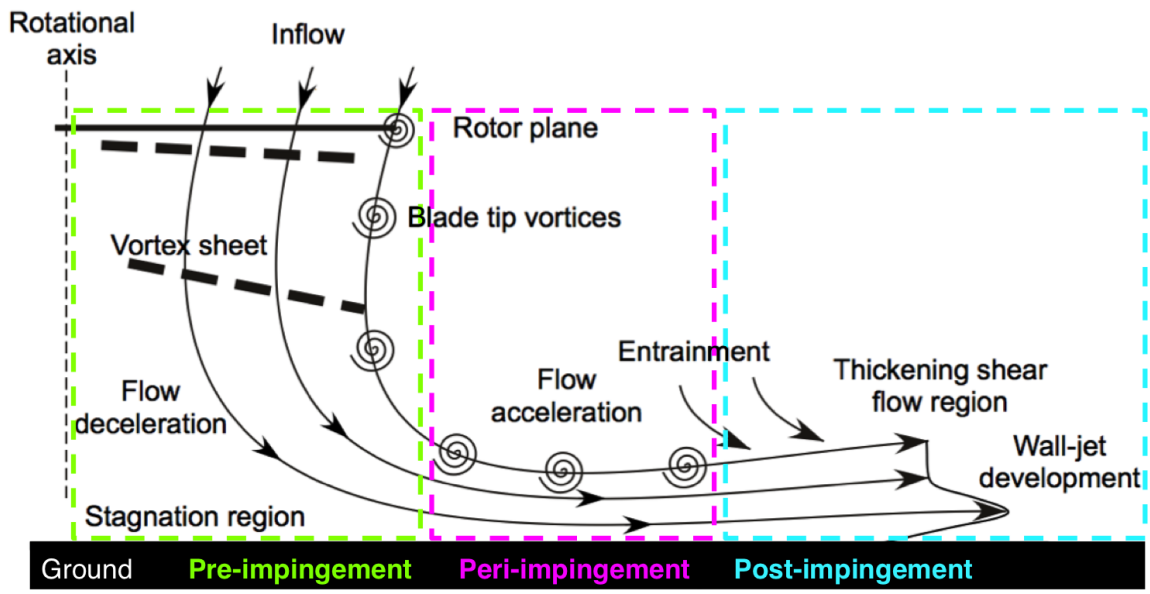

Figure 3.1: Schematic showing the behavior of the rotor wake as it impinges on the ground plane.

mostly downward below the rotor to outward over the ground plane, which causes the tip vortices to stretch radially along their lengths and to move radially outward away from the rotational axis. While the stretching initially causes some intensification of the vorticity within the vortex cores, the action of viscosity and turbulence near the ground soon causes the vortices to diffuse.

The convection of a rotor wake as it descends from the rotor plane and turns to travel along the ground plane can be divided into three phases, which have been termed pre-impingement, peri-impingement, and post-impingement, as shown in Fig. 3.1. To define the region of the flow field in which each of these phases occurred, the wake trajectories observed in the FV images were examined carefully.

The pre-impingement zone was defined as the region from the rotational axis of the rotor to the point at which the wake began to turn, transitioning from a mostly downward trajectory to an outward trajectory and the flow became more parallel to the ground. In the present case, this

transition appeared to occur when the rotor wake and the tip vortices had descended to a height of approximately 0.17–0.20 z/R above the ground. Beyond this point, the wake was considered to be the within the impingement (or peri-impingement) zone. Within the impingement zone, the vortices of the now radially expanding rotor wake were seen to convect very closely to the ground (or bed) but also travel fairly steadily and almost parallel to the ground.

Points beyond which the vortices could no longer be observed were considered to be within the post-impingement zone. One process that can alter the steady convection and persistence of the vortices in the flow is pairing and merging, a behavior associated with two or more vortices being convected closer together while orbiting around each other, which can sometimes result in the vortices merging into what may be called a "super-vortex." Another process is diffusion, in which viscosity and turbulence act to break down the laminar inner core of a vortex, causing the vortex to diffuse quickly into smaller scale eddies and turbulence.

The location of wake impingement on the ground, which is the point at which the wake trajectory transitions from mostly downward to mostly outward, is affected by the operating conditions of the rotor. To explore this behavior, a scoping study was performed in which FV was obtained for the one-bladed and two-bladed rotors at three rotor heights above the ground with the rotor operating at two rotational frequencies, the results from which are shown in Figs. 3.2 and 3.3. Comparing Fig. 3.2(a) to Figs. 3.2(c) and 3.2(e), it can be seen that as the height of the rotor above the ground is increased, the location of wake impingement is moved further outboard. Increasing the rotational frequency from 110 Hz (shown in Figs. 3.2(a), 3.2(c), and 3.2(e)) to 130 Hz (shown in Figs. 3.2(b), 3.2(d), and 3.2(f)) also moved the location of impingement farther downstream

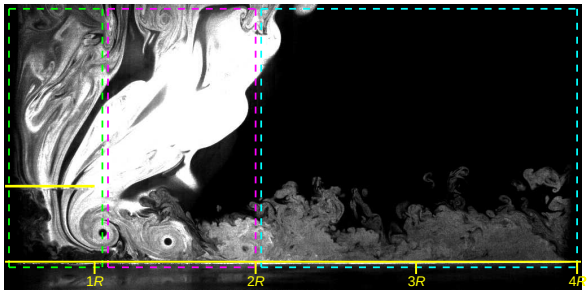

(a) $f = 110$ Hz and $z/R = 0.5$.

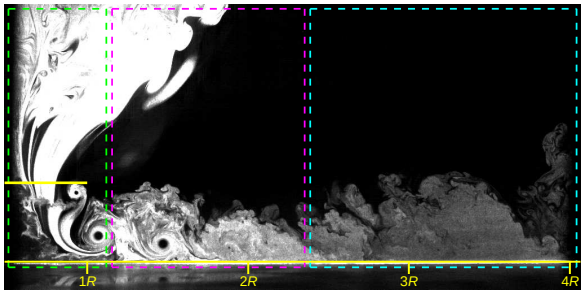

(b) $f = 130$ Hz and $z/R = 0.5$.

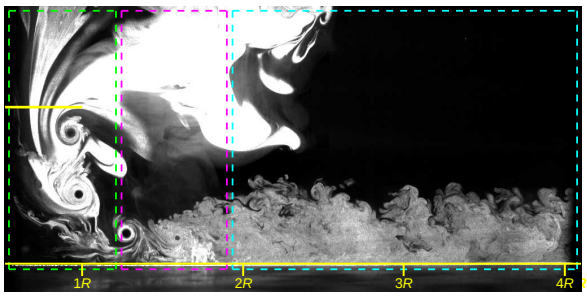

(c) $f = 110$ Hz and $z/R = 1.0$.

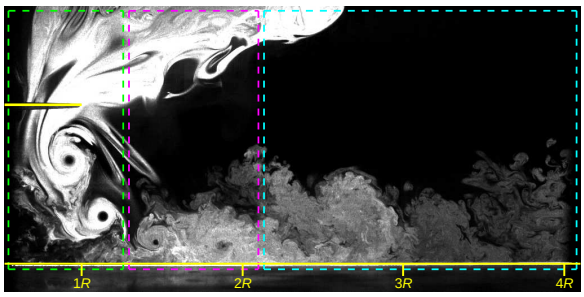

(d) $f = 130$ Hz and $z/R = 1.0$.

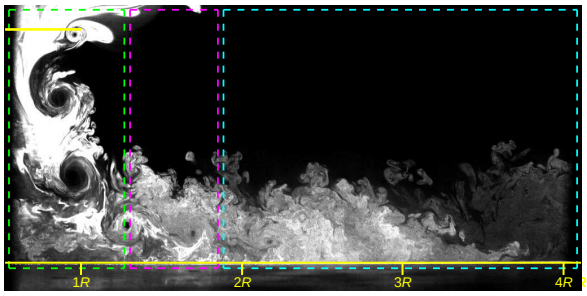

(e) $f = 110$ Hz and $z/R = 1.5$.

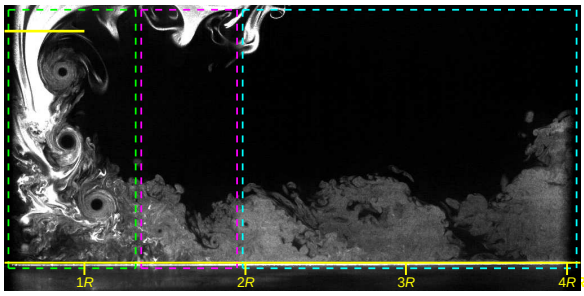

(f) $f = 130$ Hz and $z/R = 1.5$.

Figure 3.2: FV images used to define the location of the three vortex impingement zones for the one-bladed rotor while operating at various conditions, including three heights above the ground plane and at two rotational frequencies.

for a given rotor height. In addition to affecting the impingement location, the persistence of the vortices in the flow is also influenced by the rotor operating conditions. For example, as the rotor height off the ground is decreased (compare Fig. 3.2(c) to Fig. 3.2(a)) or as rotational frequency is increased (compare Fig. 3.2(a) to Fig. 3.2(b)), the vortices persist in the flow to older wake ages before diffusing.

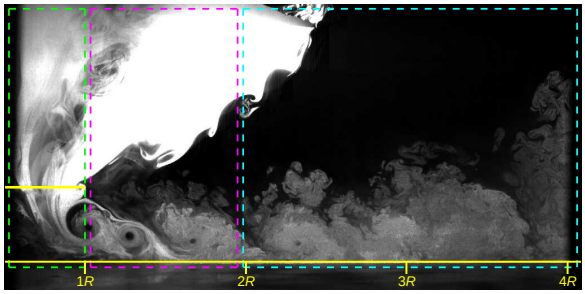

(a) $f = 110$ Hz and $z/R = 0.5$.

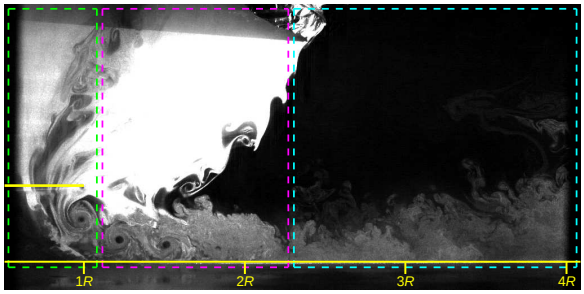

(b) $f = 130$ Hz and $z/R = 0.5$.

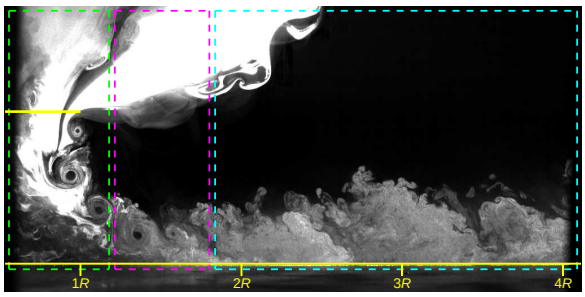

(c) $f = 110$ Hz and $z/R = 1.0$.

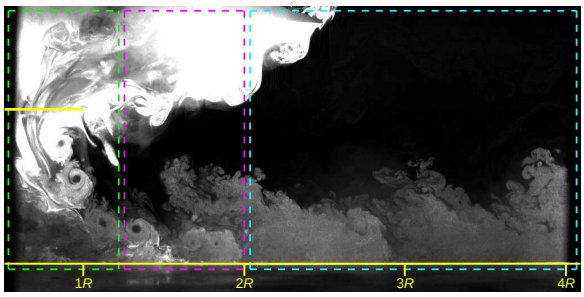

(d) $f = 130$ Hz and $z/R = 1.0$.

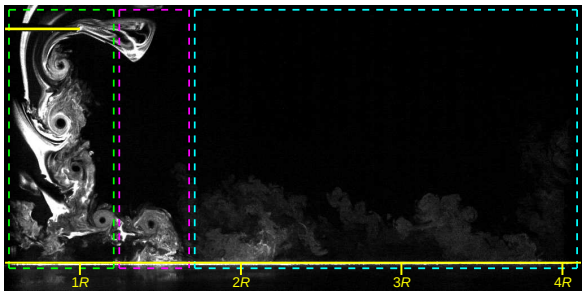

(e) $f = 110$ Hz and $z/R = 1.5$.

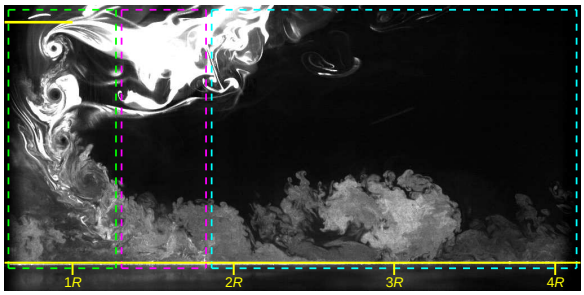

(f) $f = 130$ Hz and $z/R = 1.5$.

Figure 3.3: FV images used to define the location of the three vortex impingement zones for the two-bladed rotor while operating at various conditions, including three heights above the ground plane and at two rotational frequencies.

Figure 3.3 shows that for the two-bladed rotor the location of the wake impingement zone shifts in a similar fashion to variations in the height of the rotor above the ground and also the rotational frequency. However, when comparing the impingement zones for the same rotor height and rotational frequency for the one-bladed and two-bladed rotors, the wake of the two-bladed rotor impinges closer to the rotational axis; see Figs. 3.3(a) and 3.2(a). Because in this case the

two-bladed rotor is operating at approximately twice the thrust of the one-bladed rotor, as explained in Chapter 2, its inflow is greater by a factor of about 1.41, which convects the wake vortices closer to the ground before they begin to turn and expand outward, thereby causing the wake to impinge on the ground closer to the rotor. Using the two-bladed rotor increases the frequency of pairing and merging of the vortices, and the flow also exhibited more aperiodicity, i.e., the wake did not repeat its flow structure exactly from rotor revolution to revolution.

3.2 Identifying Event Signatures

Because the goal of the present research was to study the relationship between vortices passing over a sediment bed and the ground pressure fluctuations they produce, another scoping study was also performed. The initial tests utilized the one-bladed rotor because its wake is more periodic than the two-bladed rotor and discrete pressure signatures would be easier to identify. The one-bladed rotor, which trails only one tip vortex per revolution, produces a wake with greater spacing between adjacent turns of the helicoidal vortex, which reduces the frequency of vortex-vortex interactions such as pairing and merging. These wake characteristics were preferable because they produced cleaner pressure responses that could be used to determine the existence of a specific pressure signature corresponding to a specific flow event, such as the nearby passage of a vortex. However, tests with the two-bladed rotor were also performed to examine its effects on the pressure at the ground.

Pressure measurements were taken at the same three rotor plane heights above the ground. As the rotor height was decreased, the magnitude of the pressure responses increased. Again,

the rotor was operated at both the lower and higher rotational frequencies. The higher rotational frequency (130 Hz) produced pressure responses of larger magnitude. In general, the closer the rotor was operated to the ground and the higher the rotational frequency, the more clearly the pressure fluctuations could be observed. The pressure measurements in both cases were found to be similar in form and characteristics, but the two-bladed rotor produced twice as many events per rotor revolution.

After determining the locations of the three phases of rotor wake impingement on the ground, as was obtained from the FV scoping study, the pressure responses measured within these respective regions were examined for patterns that could be considered indicative of specific flow events. To characterize the the nature of the ground pressure measured at different radial locations, ensemble phase-averaging was performed on selected cycles. This process involved dividing the total signal period into cycles containing a fixed number of fluctuation peaks. All possible combinations of these cycle segments were then considered. A cross-correlation was performed on each combination of cycles to evaluate their similarity. A threshold was set for the minimum acceptable cross-correlation to identify cycles that were sufficiently similar in form. All cycle pairs with cross-correlation values that exceeded this threshold were then ensemble phase-averaged.

Figure 3.4 shows this results for the one-bladed rotor when it was operating at a rotor height of z/R = 0.5 and at a rotational frequency of 130 Hz. The regions of impingement are summarized by the results shown in Fig. 3.4(a). A radial location from each of the three impingement zones was selected, and a phase-averaged cycle for each of the locations is shown in Fig. 3.4(b) to describe the nature of the pressures that were measured there. Within the pre-impingement zone

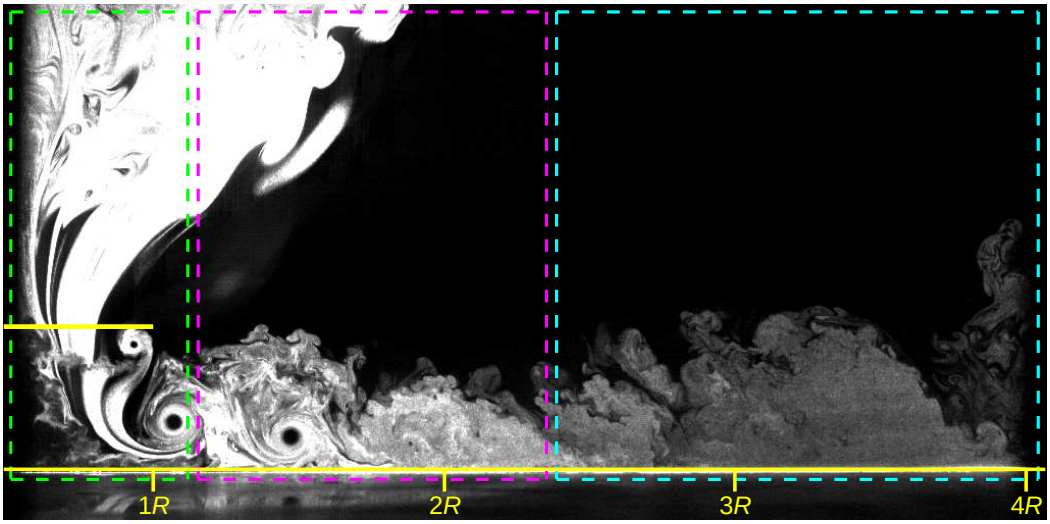

(a) A FV image outlining the pre-, peri-, and post-impingement zones.

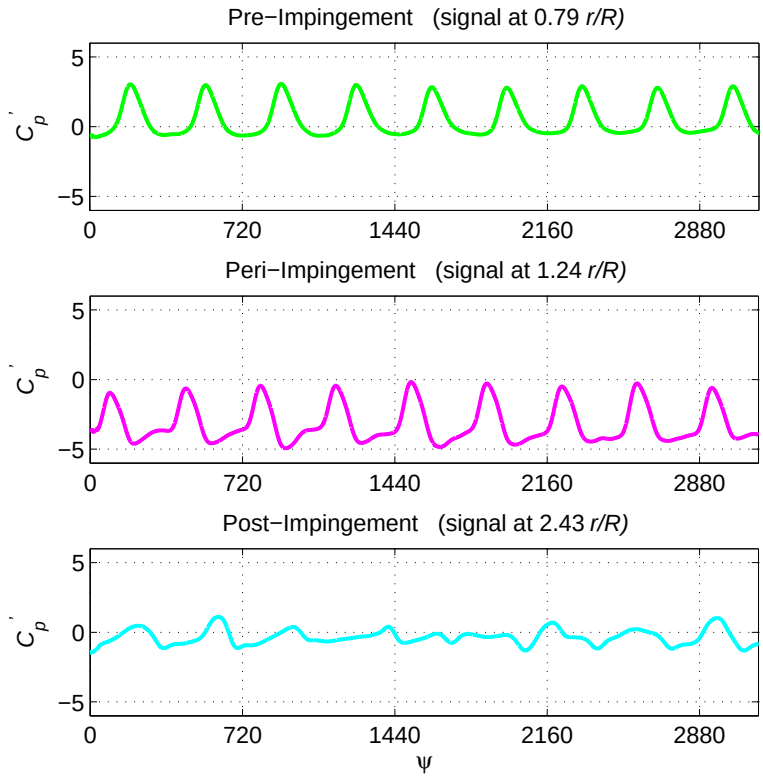

(b) Examples of phase-averaged pressure signatures from within pre-, peri-, and post-impingement zones.

Figure 3.4: A FV image defining the locations of the three phases of vortex impingement. The phase-averaged responses show the characteristics of their corresponding pressure signatures. One-bladed rotor operating at 0.5 z/R and 130 Hz.

at 0.79 r/R in this case, the unsteady pressure response exhibited smooth peaks that occurred at once-per-revolution (1/rev), with a maximum $C_p{}'$ value of approximately 3. Farther downstream at 1.24 r/R, the unsteady pressure measured within the peri-impingement zone also exhibited a 1/rev pattern but whose shape was more of a trough with an oblique, notched bottom. The unsteady pressures here were mostly negative, i.e., suction pressures. Within the post-impingement zone at 2.43 r/R, the unsteady pressure response was more irregular and the peak-to-peak magnitudes of the more random pressure fluctuations were seen to be considerably lower than for the other two zones. Pressure responses from within this zone can contain an occasional peak or peak-dip pair of significant magnitude, likely indicative of an aperiodic process of vortex pairing and/or merging.

A similar analysis of the results from the 1.0 z/R test are shown in Fig. 3.5. Again, the regions of impingement are summarized in Fig. 3.5(a), and the phase-averaged pressure cycles from each zone are presented in Fig. 3.5(b). The peaks within pre-impingement cycle, measured at 0.79 r/R in this case, were smaller but less smooth compared to those seen in the measurements obtained with the rotor operating at a height of $z/R = 0.5$. However, the pressure peaks still occurred at a frequency of 1/rev. The peri-impingement pressure response exhibited the trough shape with an oblique, notched bottom, but in this case the shape was perhaps less clear. The pressure did not become completely negative in this case but it does show decreases at a frequency of 1/rev. The features of the post-impingement cycle, measured at 2.13 r/R in this case, were less clear than for the other zones because the pressures here had much lower magnitudes. The small oscillations shown are likely to be the result of the turbulence that is present in the flow within that region near the ground plane.

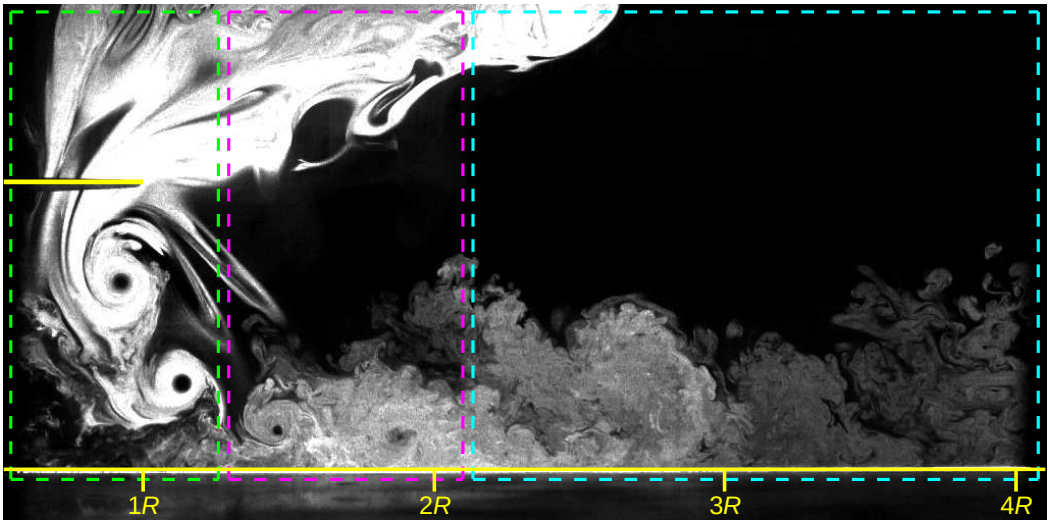

(a) A FV image outlining the pre-, peri-, and post-impingement zones.

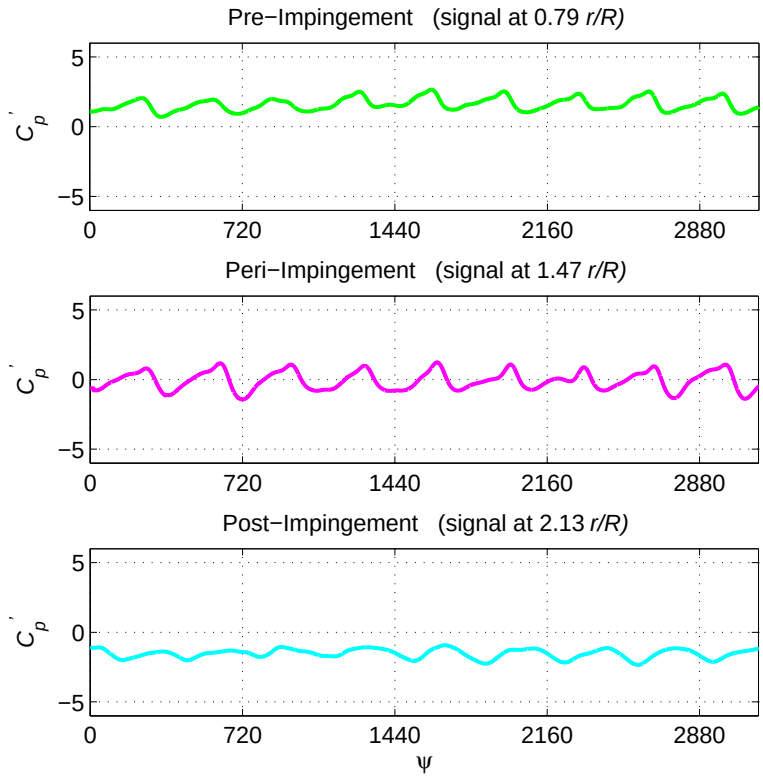

(b) Examples of phase-averaged pressure signatures from within pre-, peri-, and post-impingement zones.

Figure 3.5: A FV image defining the location of the three phases of vortex impingement. The phase-averaged pressure responses show the characteristics of their corresponding pressure signatures. One-bladed rotor operating at 1.0 z/R and 130 Hz.

Finally, the results from the z/R = 1.5 test are shown in Fig. 3.6. It can be seen from Fig. 3.6(a), that the narrowest impingement zone exists at the highest rotor height off the ground. Phase-averages of the unsteady pressure measurements at r/R = 0.79, 1.77, and 2.13 are shown in Fig. 3.6(b). The first response is from the pre-impingement zone and shows smooth peaks of similar magnitude to those seen for the z/R = 1.0 case. However, the base of these peaks is narrower. Instead of blending together continuously, with the downward slope of one end of the peak leading right into the upward slope of the next peak, these peaks appear to be more discrete while still containing the 1/rev frequency. For the peri-impingement zone, the trough shapes in the pressure response were apparent again but were of smaller magnitude than those produced at z/R = 1.0. At this rotor height from the ground, the rotor wake generated relatively small pressure responses in the post-impingement zone.

3.3 Description of the Condensed Test Matrix

Based on the results from the scoping studies, a condensed test matrix was determined. It has been shown that varying the rotor height above the ground plane affected the location of the wake impingement zone and the magnitude of the unsteady pressure responses. Each 0.5 z/R increment in rotor height shifted the onset of wake impingement by approximately 0.1 r/R. The lowest rotor height of 0.5 z/R produced the clearest unsteady pressure responses on the ground plane, with easily recognizable event signatures corresponding to the effects of vortices in the flow. It also generated the strongest suction pressures in the peri-impingement zone, which would likely make any vortex-induced suction effects on particle mobilization more pronounced. These effects, if

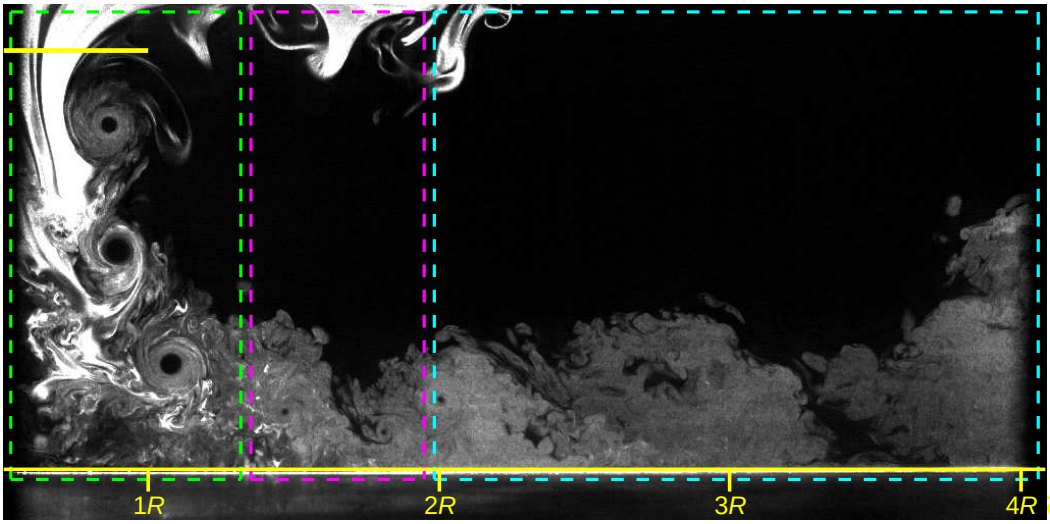

(a) A FV image outlining the pre-, peri-, and post-impingement zones.

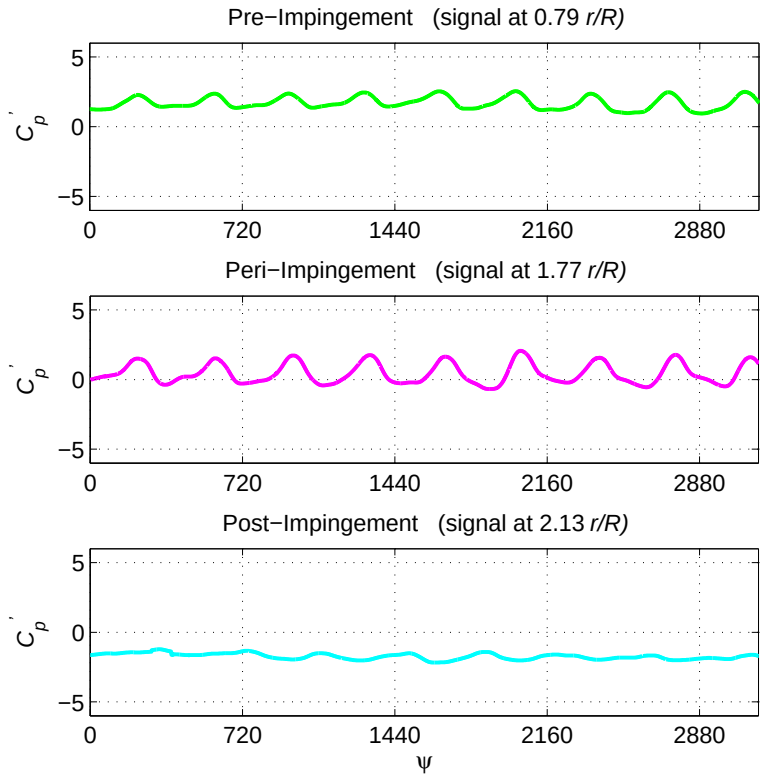

(b) Examples of averaged pressure signatures from within pre-, peri-, and post-impingement zones.

Figure 3.6: A FV image defining the location of the three phases of vortex impingement. The phase-averaged pressure responses show the characteristics of their corresponding pressure signatures. One-bladed rotor operating at 1.5 z/R and 130 Hz.

they were to exist, would likely be observable over a larger region of the ground plane because the vortices in this case were seen to persist to later wake ages.

However, while these latter operating conditions are desirable for making pressure measurements, the intensity of the wake interactions would also likely increase the quantity of sediment particle mobilization and the extent of particle uplift. With more sediment in the flow, and the sediment also being lifted to higher heights above the bed, PIV and PTV measurements become more difficult. As the particle cloud grows downstream it can block the incoming (incident) laser light and cast shadows in the flow further upstream, i.e., the images have bands of greater and lower light intensity. This tradeoff in the quantity of uplifted particles and the strength of pressure responses made a compromise necessary. Because the 1.5 z/R rotor height produced lowest unsteady pressures in the peri-impingement zone, it was decided that most of the next set of experiments would be performed at a rotor height of 1.0 r/R above the ground plane and/or sediment bed.

Varying the rotational frequency of the rotor also affected the location of the wake impingement zone and the magnitude of the pressure responses. Increasing the rotational frequency from 110 Hz to 130 Hz shifted the wake impingement zone outward by approximately 0.06 r/R. Because the higher rotational frequency produced pressure responses with more clearly identifiable features, a frequency of 130 Hz was selected to be the operating condition for most of the subsequent experiments.

Increasing the number of blades from one to two shifted the location of wake impingement inboard by 0.04 r/R. This change also doubled the number of observable flow events because the two-bladed rotor trails two blade tip vortices per rotor revolution. Consequently, the two-bladed

wake was comprised of vortices that convected over the ground with twice the frequency and approximately half the vortex-to-vortex spacing. It was decided to pursue experiments using both the one-bladed and two-bladed rotors to examine how these differences would affect the unsteady pressures on the ground plane.

Experiments to document the characteristics of both the single-phase and dual-phase flow were necessary. While the real-world problem of brownout is fundamentally a dual-phase flow problem, the presence of sediment particles in the flow can make it difficult to obtain quantitative measurements of the carrier phase of the flow. Also, the impingement of the rotor wake on the sediment bed can cause deflation of the bed and the formation of dunes, which can affect the results. In particular, laser shadowing can result within these regions of the bed topology, compromising the near ground flow velocity measurements. Additionally, because of the size and reflectivity of the airborne sediment particles, they can obfuscate nearby tracer particles, causing a loss of PIV information at those locations. In this latter case, during the processing of the PIV data any erroneous vectors can be replaced with interpolated vectors but the use of this strategy must be minimized as much as possible. Because of these limitations, single-phase flow (i.e., carrier flow alone) measurements were also performed to measure the velocity field over the regions of interest.

3.4 Flow Visualization Results

Initial scoping studies were performed at higher values of rotor thrust to produce a sufficiently large signal-to-noise ratio (SNR) and the clearest pressure responses possible. Also, because the purpose of those experiments was only to explore the general nature of the flow field and

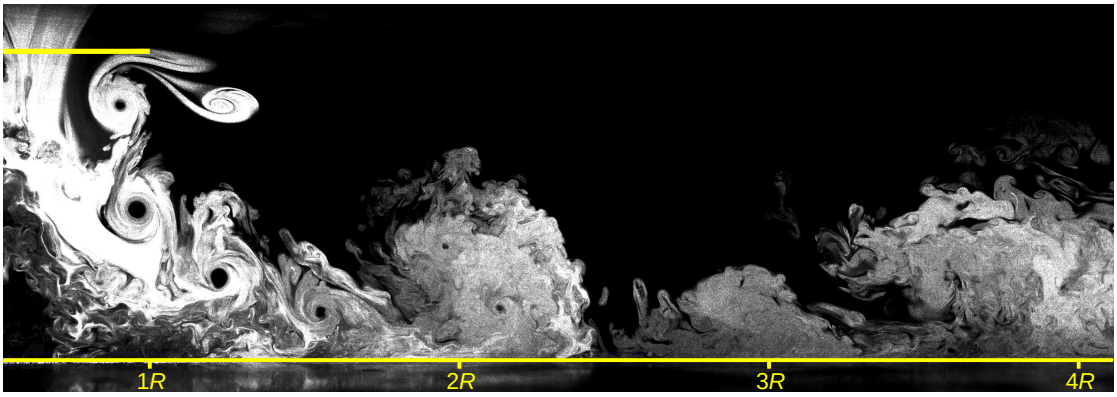

(a) One-bladed rotor.

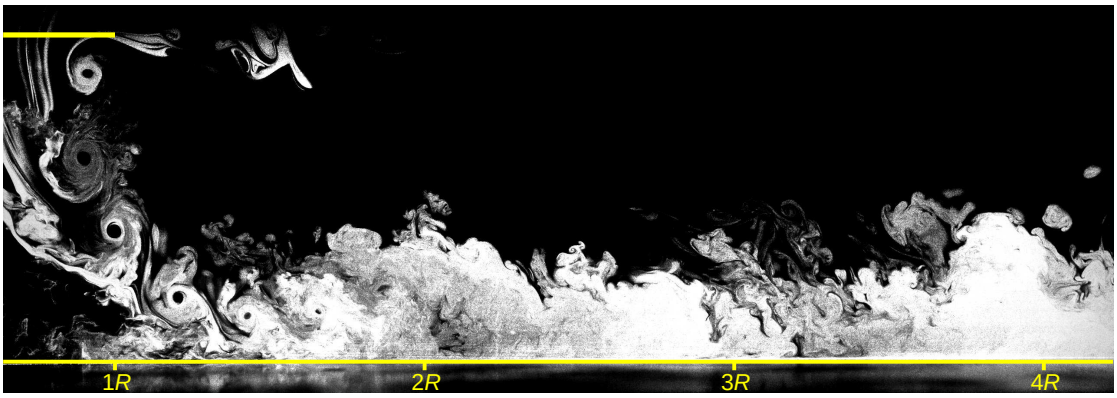

(b) Two-bladed rotor.

Figure 3.7: Single-phase FV images for z/R = 1.0 and 130 Hz.

the pressure fluctuations on the ground plane over a range of operating conditions, operations at a specific thrust or blade loading coefficient were not required. However, the results presented in this section will be for experiments where the rotor was operated $C_T/\sigma = 0.0667$, i.e., a relatively modest blade loading coefficient typical of a helicopter in hovering flight.

Single-phase and dual-phase FV results for the condensed test matrix are presented in Figs. 3.7 and 3.8, respectively. The onset of particle uplift on the bed occurs near 1.65 r/R for the one-bladed case, whereas particle uplift begins more inboard beneath the two-bladed rotor, with mobilized sediment already being visible at the left boundary of the ROI near 0.65 r/R; compare Figs. 3.8(a) and

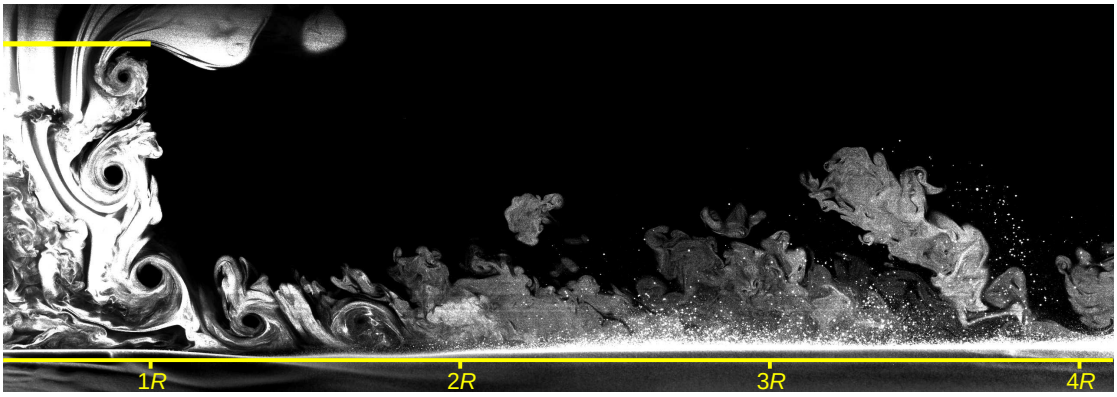

(a) One-bladed rotor.

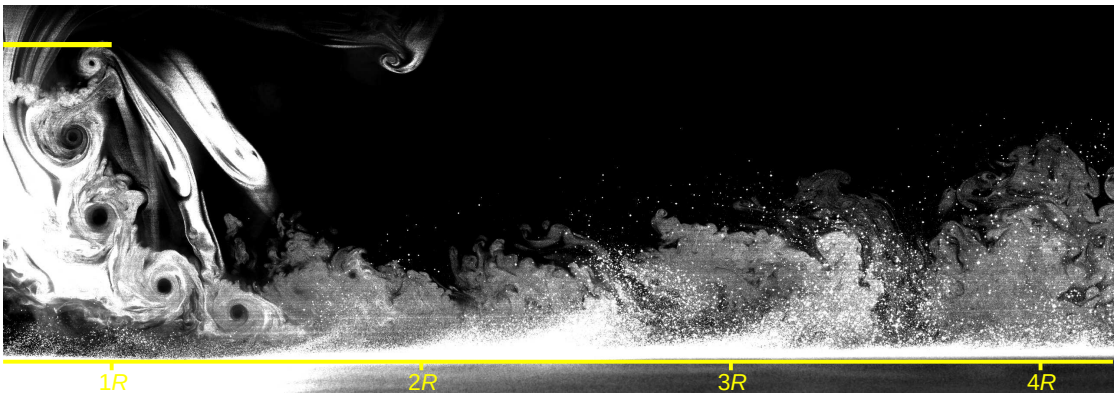

(b) Two-bladed rotor.

Figure 3.8: Dual-phase FV images for z/R = 1.0 and 130 Hz.

3.8(b). The two-bladed rotor also mobilized and uplifted more particles, with waves of particles cresting as high as 0.20 z/R off the bed, while sediment waves for the one-bladed rotor crested only near 0.13 z/R. The maximum heights reached by the particles for each rotor were similar, with particles being observed up to 0.67 z/R for the one-bladed rotor and 0.79 z/R for the two-bladed rotor. However, the overall quantity of particles found to be suspended at these heights was definitely greater for the two-bladed rotor.

3.5 Unsteady Pressure Measurements

Unsteady pressure measurements were obtained over the ground beneath the hovering rotor for the conditions defined in the condensed test matrix shown in Tab. 3.1. Figure 3.9 shows perspective views or carpet plots for the complete time-history of the pressure measurements for the one-bladed and two-bladed rotors. Figure 3.10 presents these carpet pressure plots in greater detail by showing only a fraction of the time-history. It can be seen that while the wakes impinge on the ground plane at different radial locations for each rotor, the time-averaged pressures as a function of radial distance are very similar.

Directly beneath the rotor is a stagnation region where the flow is mostly downward on the ground; this area is where the highest positive values of $C_p{}'$ occurred. Figure 3.9(a) shows maximum $C_p{}'$ values of 1.5 were produced with the one-bladed rotor. However, because the two-bladed rotor is operating at twice the thrust, and so on average higher slipstream flow velocities occur near the rotor, Fig. 3.9(b) shows maximum $C_p{}'$ values as high as 3. While Fig. 3.11 shows the complete time-history, Fig. 3.12 shows only six rotor revolutions but in greater detail, revealing that the inboard region is characterized by 1/rev oscillations that occur in-phase with the passage

Rotor Configuration	One-bladed & Two-bladed
Rotor Height	1.0 z/R
Rotational Frequency	130 Hz
Environment	Single-phase

Table 3.1: Table summarizing the rotor operating conditions for the condensed test matrix.

of the blade over the row of sensors. In fact, this effect can be seen in ground pressures measured as far downstream as 1.3–1.5 r/R.

Beyond this region, the mean Cp' values were seen to decrease and ultimately become negative, again with negative values indicating a suction pressure. Figure 3.9 shows that a negative minimum Cp' region occurs over a distance of approximately 0.5 r/R near the wake impingement location. On examination of the contours shown in Fig. 3.12, it can be seen that the peak-to-peak values of the pressure oscillations are approximately twice as large for this suction region as compared to the oscillations produced beneath the blade passage region because the velocities near impingement are higher as the flow turns outward and accelerates. For the one-bladed rotor, the peak-to-peak Cp' values near the blade are on the order of 1, whereas near impingement they are closer to 2. Similarly, the two-bladed rotor produces peak-to-peak Cp' values of approximately 1.5 in the region beneath the rotor, while this value is approximately doubled at the location of the wake impingement.

Downstream from the location of wake impingement as the vortices start to diffuse their vorticity, the mean ${C_p}'$ values gradually asymptoted to zero with increasing radial distance away from the rotor as the flow decelerates. The shallow curves shown in Fig. 3.12 indicate the propagation of pressure waves produced by the vortices as they convect radially outward from sensor location to sensor location. These waves (and smaller oscillations of pressure) are still apparent as far downstream as 4.0 r/R, mainly because of the presence of turbulent eddies in this region of the flow field.

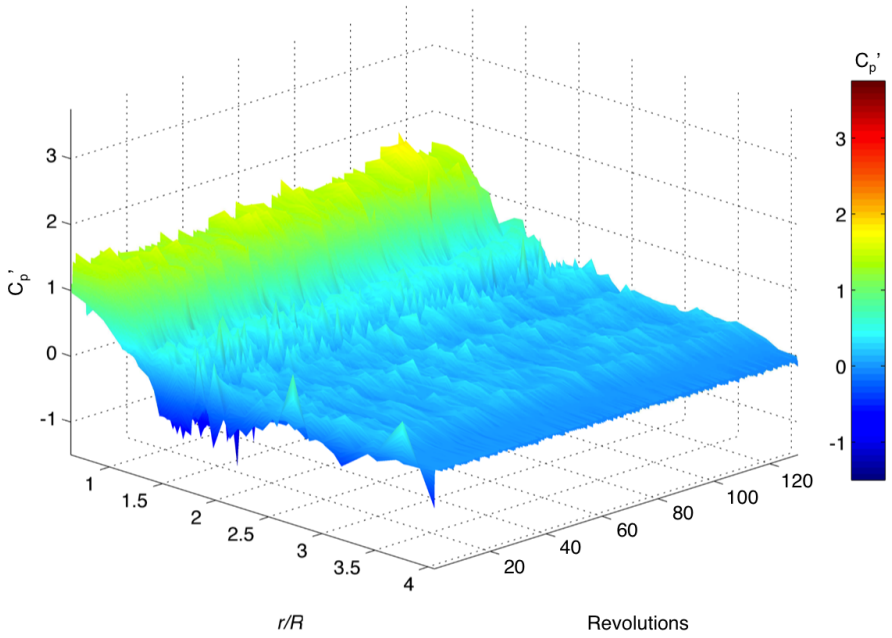

(a) One-bladed rotor.

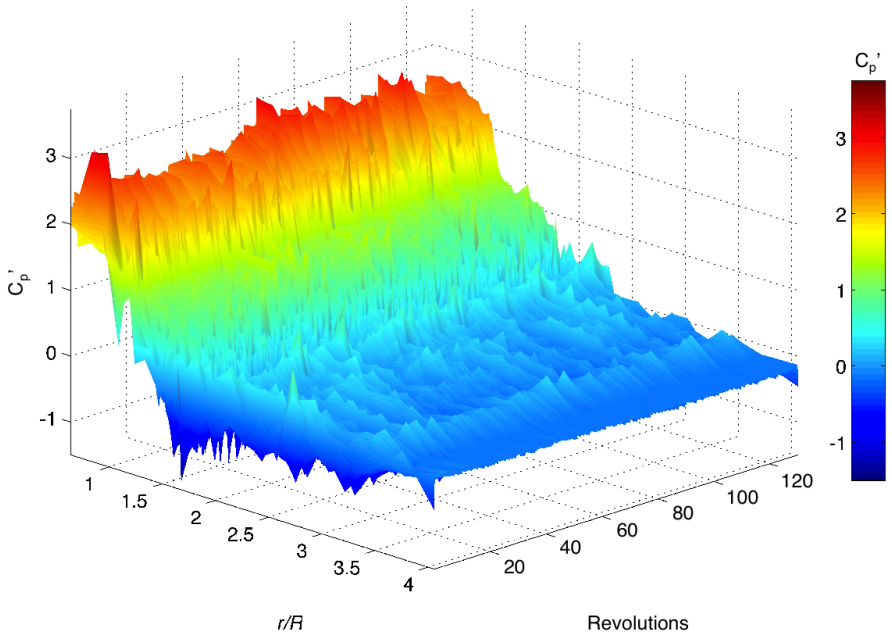

(b) Two-bladed rotor.

Figure 3.9: Carpet plots of the time-history of the ground surface pressure. One-bladed and two-bladed rotors operating at 1.0 r/R and 130 Hz.

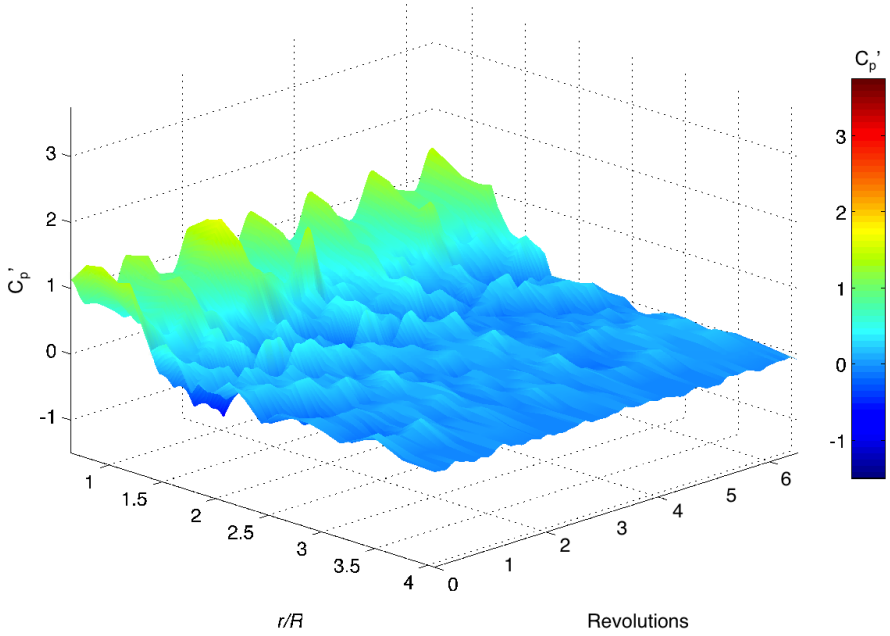

(a) One-bladed rotor.

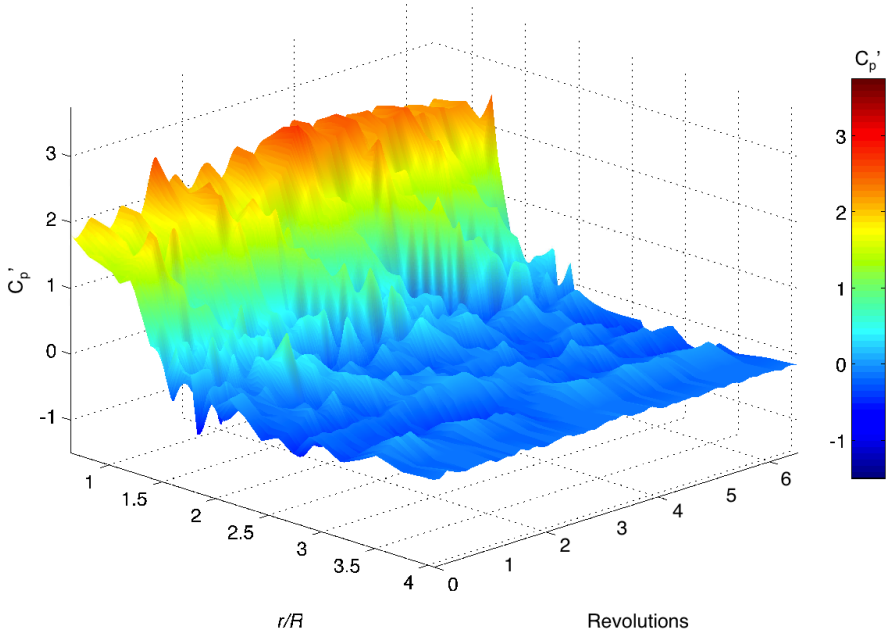

(b) Two-bladed rotor.

Figure 3.10: Detailed view of ground surface pressure carpet plots. One-bladed and two-bladed rotors operating at 1.0 r/R and 130 Hz.

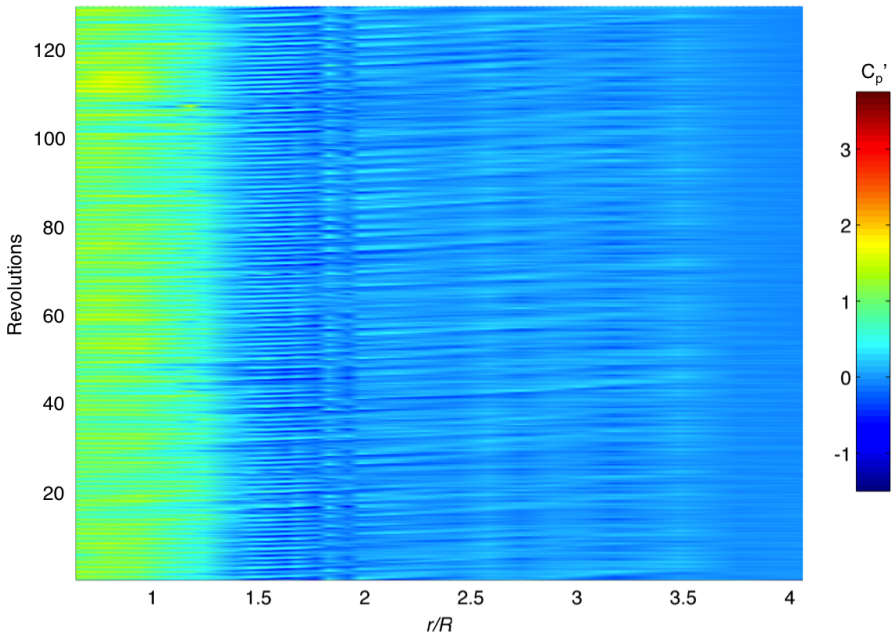

(a) One-bladed rotor.

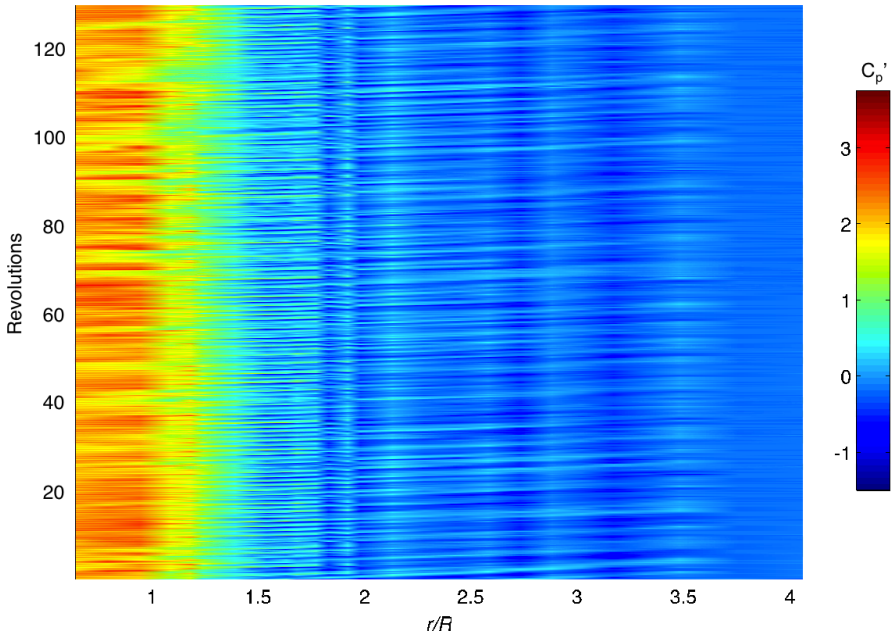

(b) Two-bladed rotor.

Figure 3.11: Contour plots of the time-history of the ground surface pressure. One-bladed and two-bladed rotors operating at 1.0 r/R and 130 Hz.

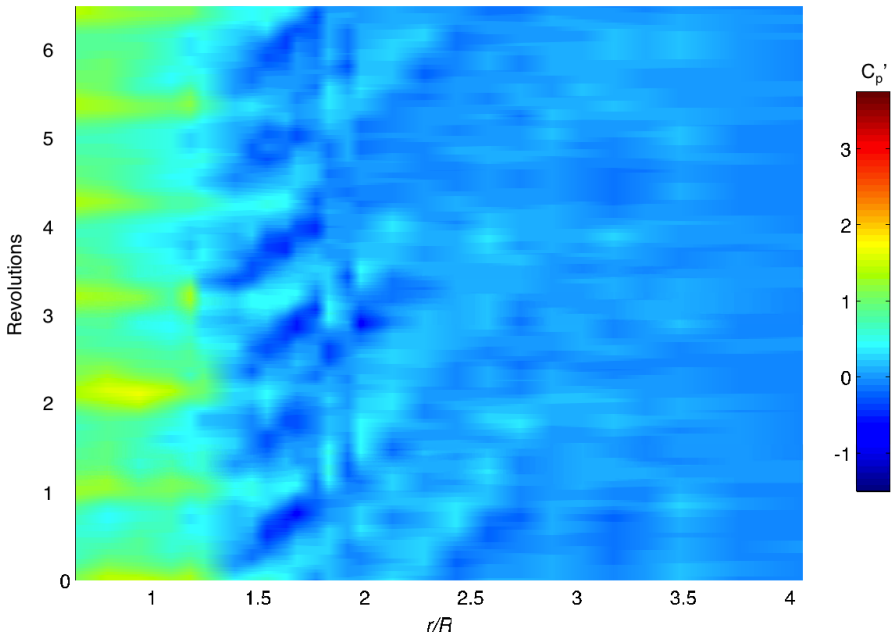

(a) One-bladed rotor.

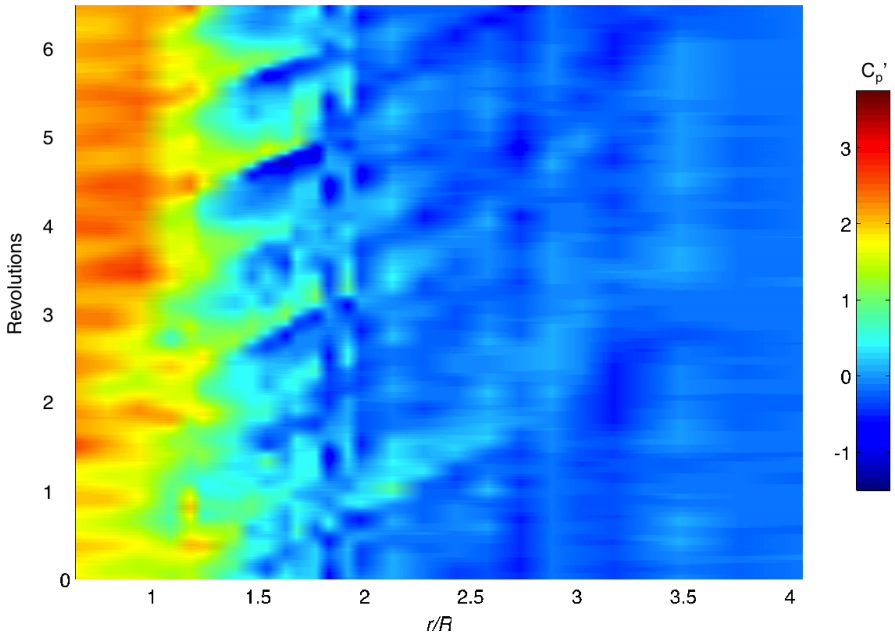

(b) Two-bladed rotor.

Figure 3.12: Detailed view of the ground surface pressure contour plots. One-bladed and two-bladed rotors operating at 1.0 r/R and 130 Hz.

3.6 Understanding the Pressure Responses

It was clear that there were many factors that could influence the shape, magnitude, and frequency of the features that comprise the unsteady pressure responses on the ground plane. Taken together, it is clearly very difficult to isolate the individual effects of number of blades, rotational frequency, rotor height, etc. To better understand the pressure responses and the factors that may influence them, the following discussion is covered in three parts: 1. the trends shown in the time-averaged pressure, 2. an explanation of the blade passage effect, and 3. the effect of vortex passage on the ground pressures.

3.6.1 Time-Averaged Pressure Responses

Using rotor momentum theory to produce a simplified model of the rotor flow while in ground effect can aid in the explanation of trends observed in the time-averaged ground pressure responses. The conditions far above the rotor were defined as ambient, and four locations within the flow field were evaluated: just above the the rotor plane, just below the rotor plane, a point in the flow convecting wall-parallel above the ground plane, and a point beneath the ground plane (aligned with the previous point); see Fig. 3.13.

At the point far above the rotor disk, velocity (V_∞) is zero and hence the pressure there is the total pressure (P_∞). Just above the rotor disk, the static pressure is P_1 and the velocity (V_1) is equal to the hover induced velocity (V_h), i.e.,

$$V_h = \sqrt{\frac{T}{2\rho A}} \tag{3.1}$$

Just below the rotor disk, the static pressure is P_2 and the velocity (V_2) is also equal to the hover induced velocity. At a point downstream above the ground plane, the static pressure and velocity are P_3 and V_3, respectively. At this same downstream distance, but for a point located below the ground plane, because the velocity (V_4) is zero there, the pressure (P_4) is equal to the ambient pressure (P_∞).

A streamline can be drawn to connect the location of the free-stream conditions to location 1, just above the rotor disk, and Bernoulli's equation can be used to derive an expression for P_1, i.e.,

$$P_\infty + \frac{1}{2}\rho {V_\infty}^2 = P_1 + \frac{1}{2}\rho {V_1}^2 \tag{3.2}$$

$$P_1 = P_\infty - \frac{T}{4A} \tag{3.3}$$

Recognizing that the difference in pressure between locations 1 and 2 is equal to the disk load-

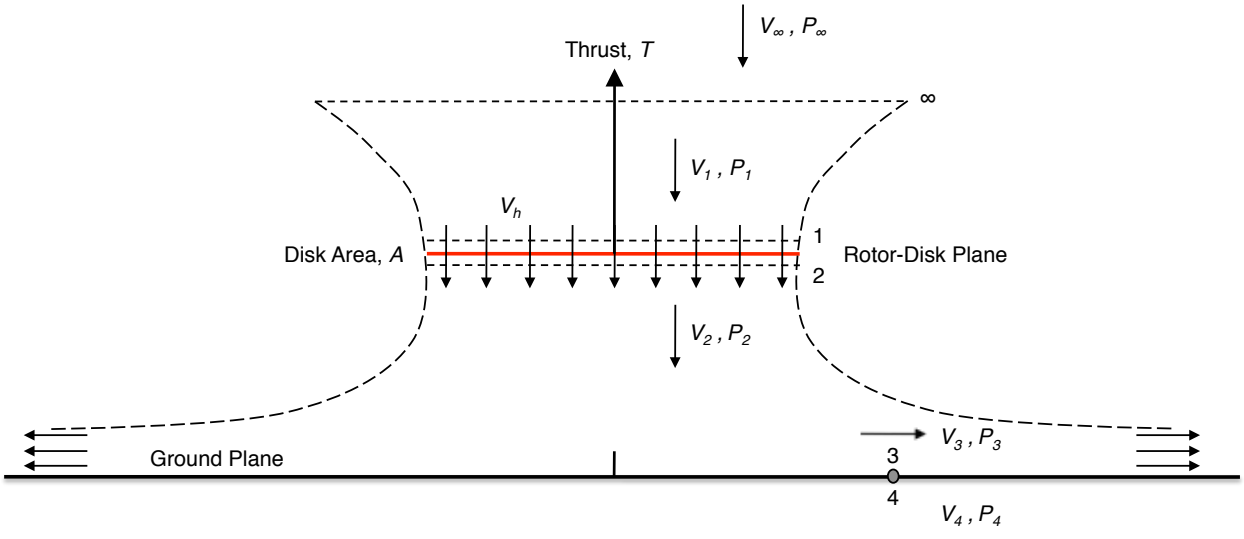

Figure 3.13: Schematic of the simplified model used for momentum theory analysis of the rotor flow field.

ing (T/A), and using the expression previously obtained for P_1, a similar expression can then be derived for P_2, i.e.,

$$P_2 = P_\infty + \frac{3T}{4A} \tag{3.4}$$

Similarly, applying Bernoulli's equation to a streamline connecting point 2 to point 3, and using the expression P_2, an expression can also be derived for P_3 in terms of P_∞, i.e.,

$$P_2 + \frac{1}{2}\rho {V_2}^2 = P_3 + \frac{1}{2}\rho {V_3}^2 \tag{3.5}$$

$$P_3 = P_\infty + \frac{T}{A}\left[1 - \frac{\overline{V_3}^2}{4}\right] \tag{3.6}$$

where $\overline{V_3}$ is the nondimensional velocity, V_3/V_h.

The differential pressure sensors measure a pressure difference between the top and bottom of the ground plane. In terms of this model, that is the difference between P_3 and P_∞. To compare

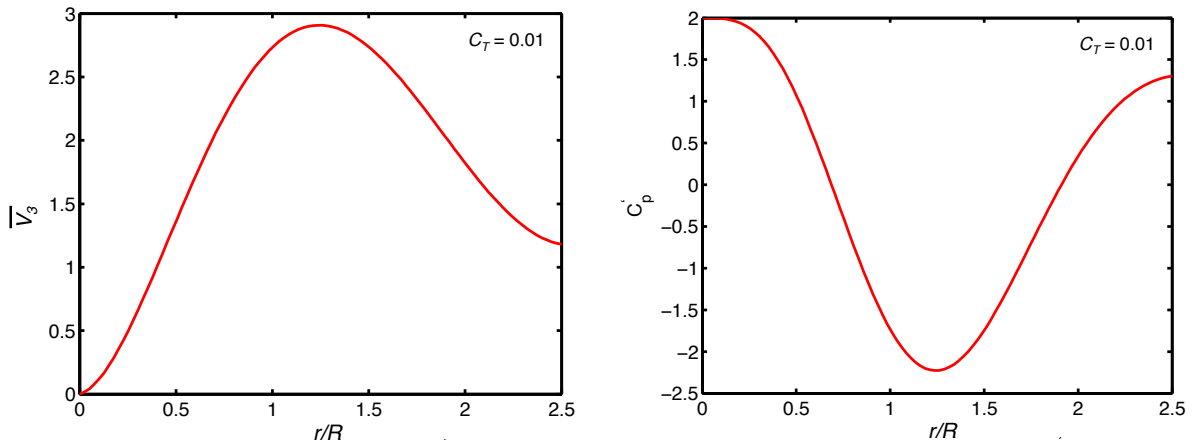

(a) Relationship between velocity and radial distance. (b) Distribution of $C_p{}'$ along the ground from Eq. 3.8.

Figure 3.14: Estimates of the velocity and pressure distribution along the ground below a hovering rotor obtained using momentum theory.

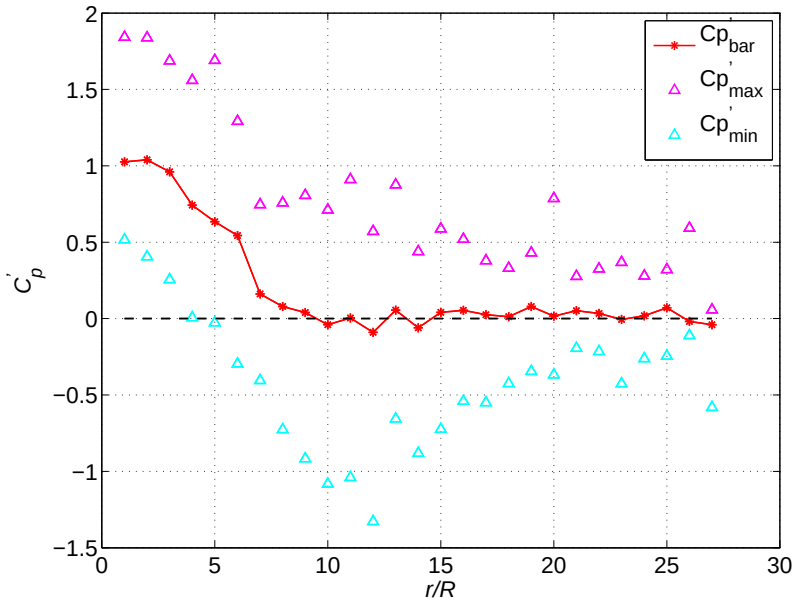

(a) One-bladed.

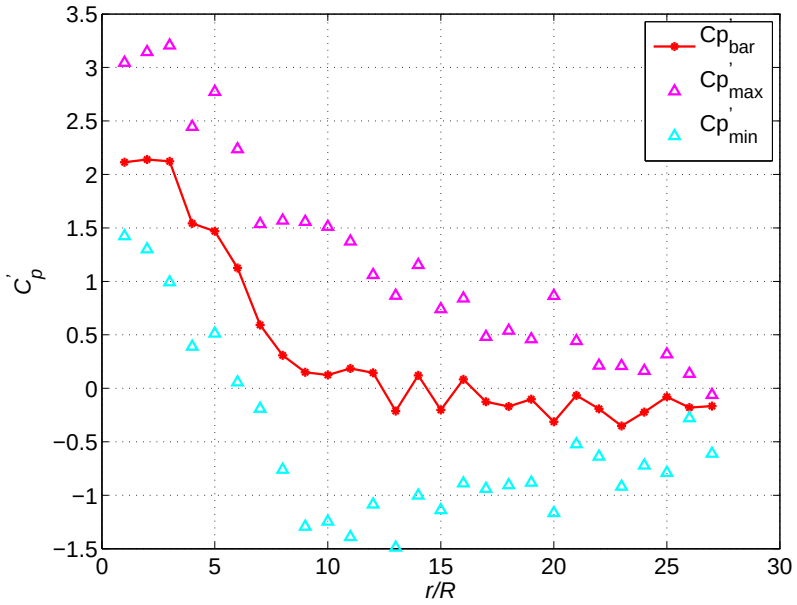

(b) Two-bladed.

Figure 3.15: Plots of the mean $C_p{}'$ values along the ground and the variation from the mean calculated from the pressure measurements.

the result of this analysis to the pressure measurements previously presented, the definition of C_p' can be invoked, i.e.,

$$C_p{}' = \frac{100\,(P_3 - P_\infty)}{\frac{1}{2}\rho(\Omega R)^2} \tag{3.7}$$

This relationship can be rewritten in terms of the thrust coefficient C_T, further simplifying the expression for $C_p{}'$ to

$$C_p{}' = 200\frac{T}{\frac{1}{2}\rho A(\Omega R)^2}\left[1 - \frac{\overline{V_3}^2}{4}\right] = 200C_T\left[1 - \frac{\overline{V_3}^2}{4}\right] \tag{3.8}$$

The rotor induced velocity will not change, but V_3 will increase as the flow impinges on the ground and turns to continue outward, and then eventually will asymptote to zero, as shown in Fig. 3.14(a). Using the expression for $C_p{}'$ (Eq. 3.8), the, Fig. 3.14(b) shows the pressure as positive inboard and then decreasing to negative values with increasing radial distance. The mean $C_p{}'$ values for the pressure measurements presented in Fig. 3.15 are similar to the pressure distribution predicted by Eq. 3.8.

3.6.2 Blade Passage Effect

For inboard radial locations below the rotor and near the rotor, the form of the pressure response remained relatively unchanged for all operating conditions. Peaks of positive pressure were similar in magnitude and occurred exactly in-phase with each other for this inboard region along the ground, as shown in Fig. 3.16. This feature is specifically the result of the bound circulation on blade(s) passing over the row of pressure sensors. Blade bound vortices produce a spike in

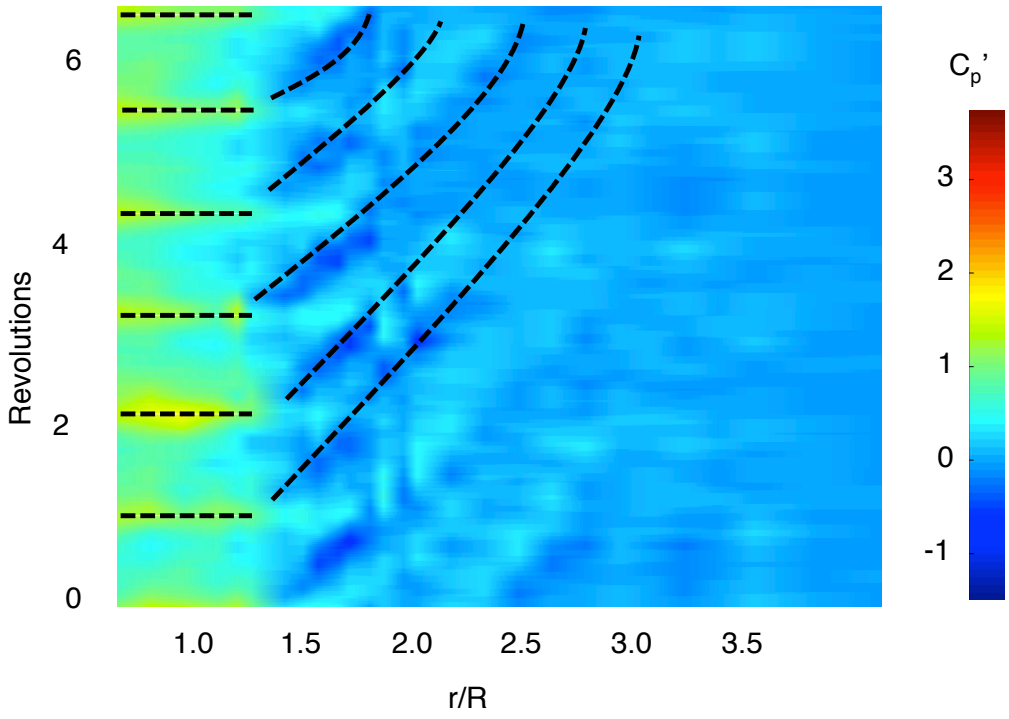

(a) One-bladed.

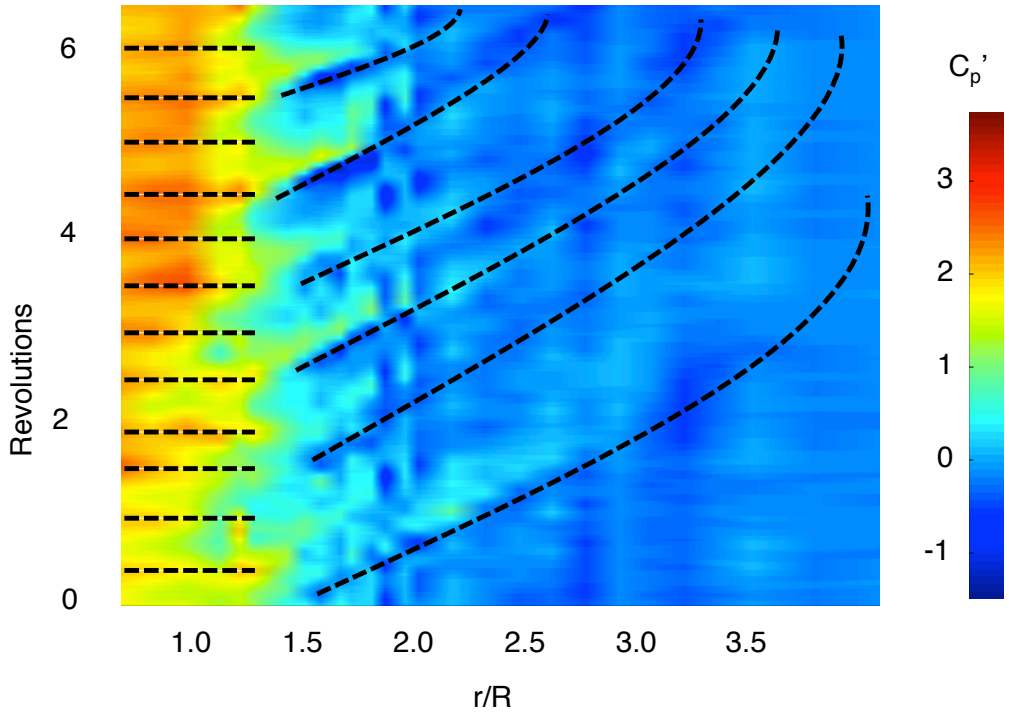

(b) Two-bladed.

Figure 3.16: Contour plots of the time-histories of the pressure measurements showing evidence of the blade passage effect.

pressure for all nearby sensors, at precisely the same time, and at a frequency of N_b/rev, where N_b is the number of blades. Because of the spatial variation of these bound vortices, trailed tip vortices are generated, which convect down to and then along the ground. In contrast to the straight lines of simultaneously occurring positive pressure pulses observed near the blade, the effect of the trailed vortices can be seen farther outboard, appearing as curved patterns which indicate the convection of these vortices through space and time. Work by Crouse et. al [58] on the topic of rotor wake/fuselage body interactions also captured this behavior of positive pressure pulses near the rotor. The study referred to it as the blade passage effect, and determined this particular pressure response was one of four representative types of unsteady pressure signatures.

3.6.3 Effect of Vortex Passage on Ground Plane Pressure

To understand the pressure response to the passage of a vortex near the ground, an unsteady flow model was developed. A schematic of this model is shown in Fig. 3.17. For this model, potential flow was assumed and used to derive expressions for the velocity and the unsteady pressure term $(\partial\phi/\partial t)$ within the unsteady Bernoulli equation, i.e.,

$$P - P_\infty = \frac{1}{2}\rho\left({V_\infty}^2 - V^2\right) - \rho\frac{\partial\phi}{\partial t} \tag{3.9}$$

where the $P - P_\infty$ term represents the static (or total pressure), the $(1/2)\,\rho\left({V_\infty}^2 - V^2\right)$ term is the dynamic pressure, and the $\rho\,(\partial\phi/\partial t)$ term is the unsteady pressure, i.e.,

$$\frac{\partial\phi}{\partial t} = -V_s \cdot V_{\text{ind}} \tag{3.10}$$

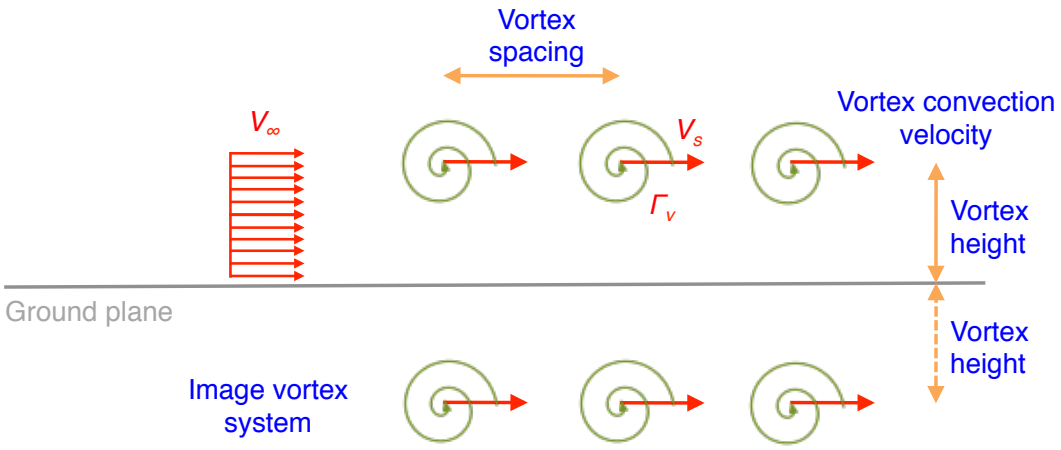

Figure 3.17: Schematic of the unsteady flow model.

A derivation of the equations used to formulate this model is given in Appendix A.

The model to can be used calculate the values of C_p' along the ground while a single vortex, or a train of vortices, convected parallel to the ground at a fixed height, velocity, vortex strength, and spacing. The method of images was utilized so that the dividing streamline became the ground plane, and a free-stream velocity was introduced to mimic the effects of the wall-parallel flow velocity that develops as a result of the rotor wake impinging and turning to flow more parallel to the ground. To calculate pressures, the velocities induced at the ground by both "real" and "imaginary" or "image" vortices were super-imposed, along with the contribution from the free-stream velocity; see Fig. 3.17. A time-history of the ground pressure was calculated using this unsteady flow model, as shown in Fig. 3.18.

To examine the simplest case first, a single vortex was used. The inputs to the model were selected to closely match the experimental conditions. The height of the vortex was set to 0.20 z/R, which was the approximate height of vortices convecting within the peri-impingement zone; see Fig. 3.19(a). The convection velocity of these impinging vortices, as obtained from PIV results,

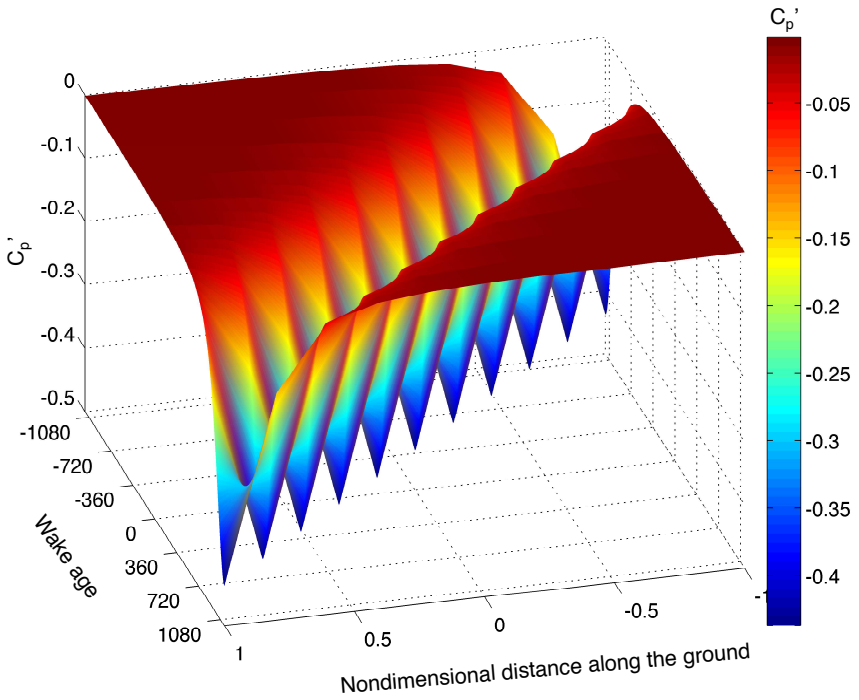

(a) Carpet plot of the $C_p{}'$ values predicted using the unsteady flow model.

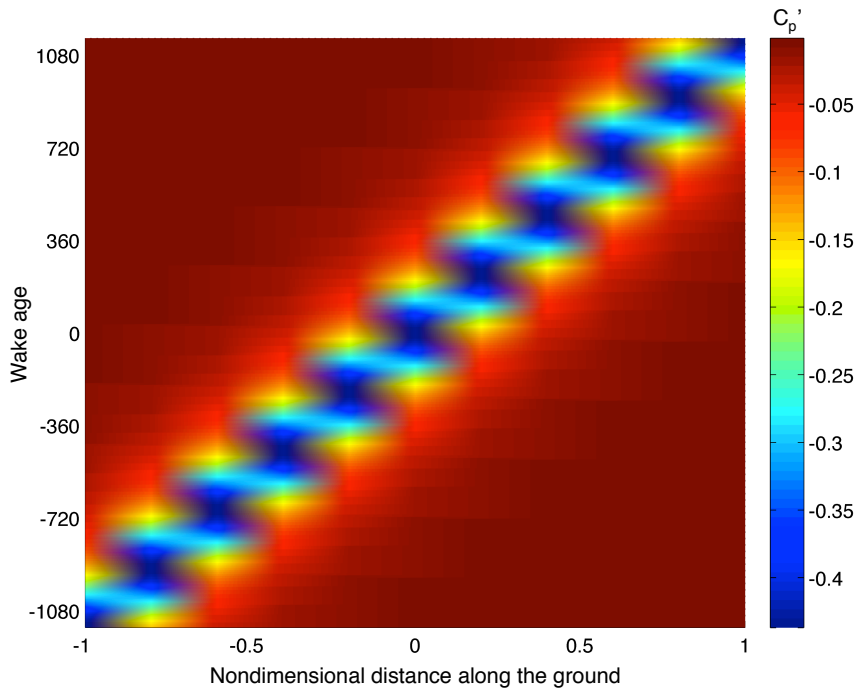

(b) Contour plot of the $C_p{}'$ values predicted using the unsteady flow model.

Figure 3.18: Predicted results from the unsteady flow model showing a vortex convecting parallel to the ground.

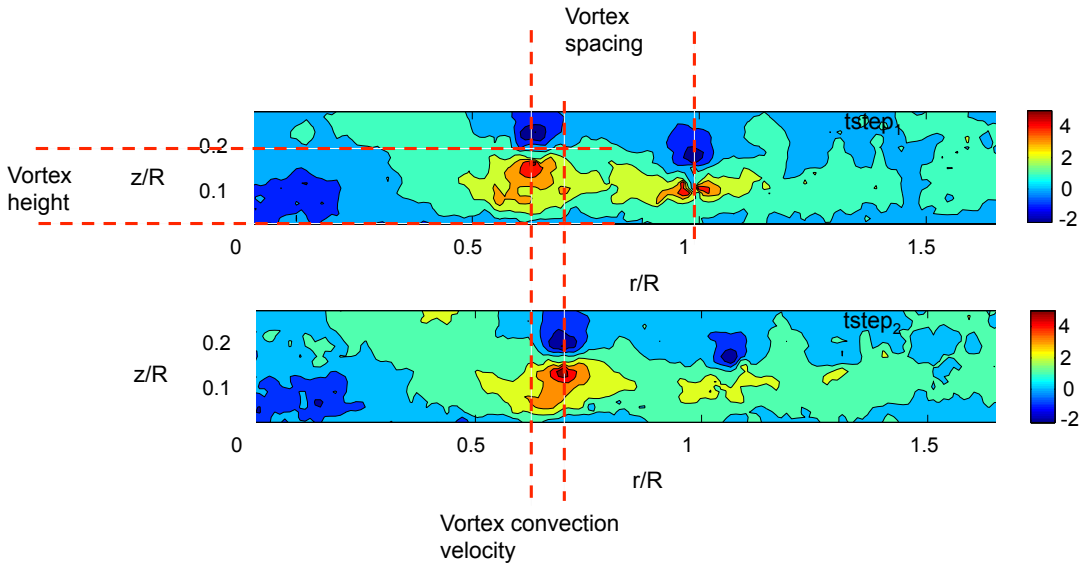

(a) Vortex spacing, vortex height, and vortex convection velocity from experiment.

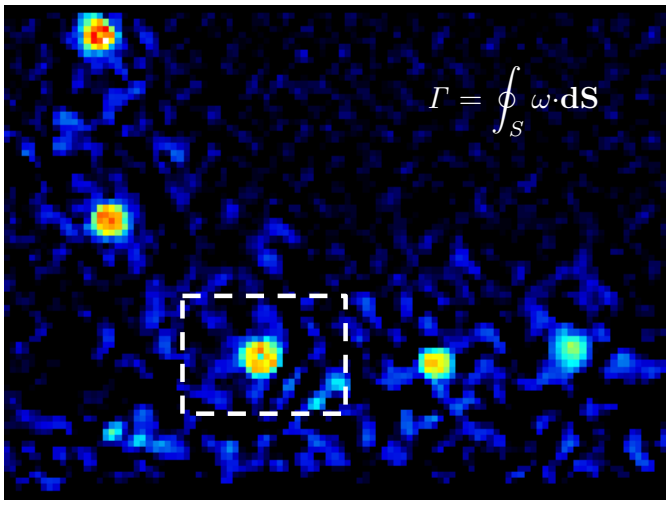

(b) Vortex strength (Γ_v) was calculated from the vorticity data.

Figure 3.19: Determining values for the unsteady flow model inputs from the experimental data.

was determined to be approximately 5% of the tip speed, i.e., 0.05 V_{tip}, also shown in Fig. 3.19(a). The vortex strength, calculated from the vorticity data, was 0.20 $\text{m}^2\ \text{s}^{-1}$, as shown in Fig. 3.19(b).

The results obtained by manipulating the magnitude of the free-stream velocity (V_∞) to vary the velocity induced at the ground are shown in Fig. 3.20. The time-history of the static, dynamic, and unsteady pressures will be plotted, hereafter, for a single point on the ground. Comparing Fig. 3.20(a) to 3.20(b) suggests that for regions of the flow for which the velocity induced at the

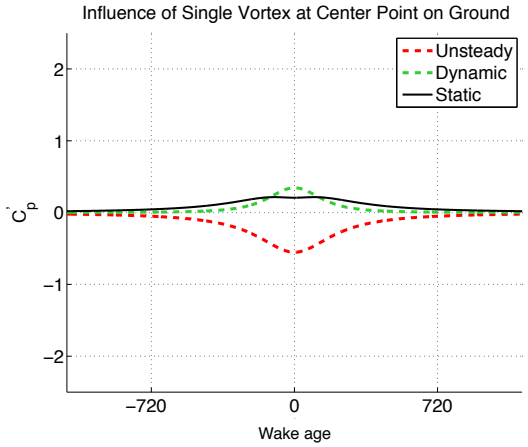

(a) $V_{\text{ind}} = 4.0\ \text{ms}^{-1}$

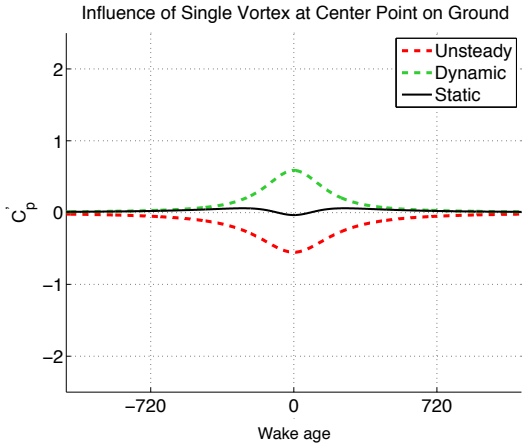

(b) $V_{\text{ind}} = 5.5\ \text{ms}^{-1}$

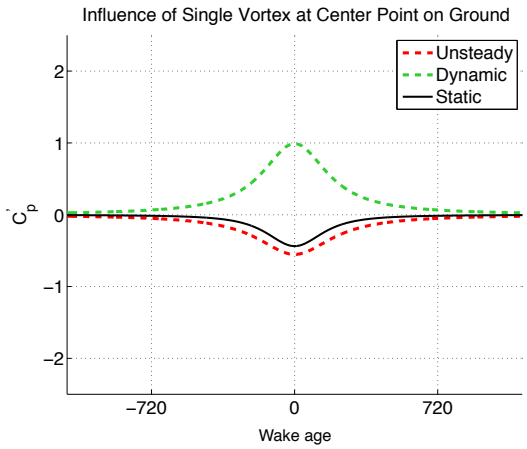

(c) $V_{\text{ind}} = 8.0\ \text{ms}^{-1}$

Figure 3.20: The pressure predictions from the unsteady flow model for three induced velocities.

ground is less than 5.5 m s^{-1}, the passage of a vortex will result in a pressure peak. Conversely, comparing Fig. 3.20(b) to 3.20(c) indicates that for regions of the flow experiencing an induced velocity in excess of 5.5 m s^{-1}, a decrease in pressure will be produced by a passing vortex.

To make the model more realistic, the passage of a train of vortices parallel to the ground was then considered. By adjusting the vortex spacing within the train, the effects produced by both one-bladed and two-bladed rotors could be simulated. From the PIV measurements, the vortex spacing produced by the one-bladed rotor was determined to be $0.31R$; see Fig. 3.19(a). Therefore, to model the two-bladed rotor case, this spacing was reduced by half. The resulting unsteady pressure predictions are shown in Fig. 3.21. Adding adjacent vortices altered the induced velocity at which the pressure resulting from vortex passage transitions from a pressure peak to a suction dip. For the 1/rev vortex train, this transitional induced velocity was 8.1 m s^{-1}. However, for the 2/rev vortex train, the pressure outcome transitioned from peak to dip at a higher induced velocity of 10.6 m s^{-1}.

The previous predictions of pressure were all obtained for vortex characteristics that were modeled to match the actual conditions of the experiment. Next, and reaching outside the bounds of the experimental values, the effect of altering these previously fixed parameters was explored. The vortex height, convection velocity, and strength of a single vortex were varied, each in turn, while holding the other two conditions and the free-stream velocity constant. The goal was to start with the actual experimental (baseline) conditions and then independently vary each of the parameters to determine the sensitivity of the pressure response to these changes. Figures 3.22–3.24 show the results from this study.

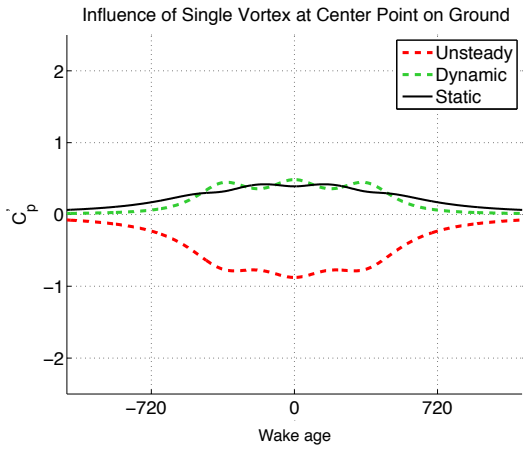

(a) $V_{\text{ind}} = 6.5$ ms^{-1}

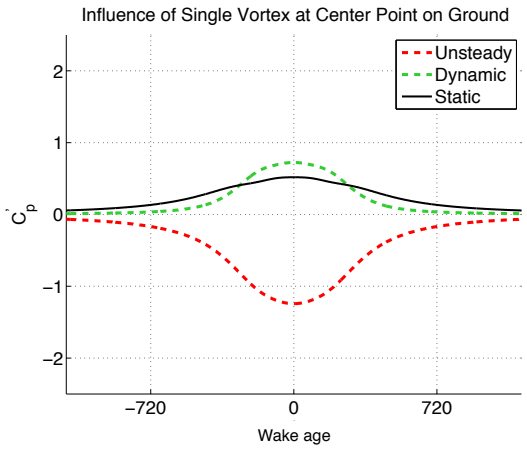

(b) $V_{\text{ind}} = 9.0$ ms^{-1}

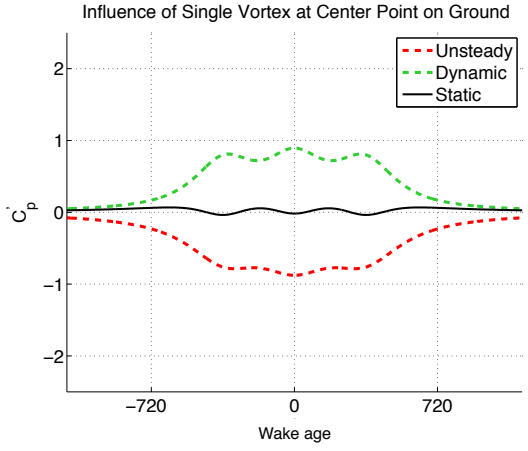

(c) $V_{\text{ind}} = 8.1$ ms^{-1}

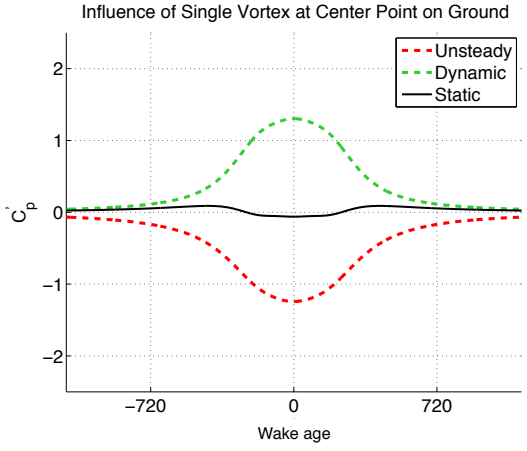

(d) $V_{\text{ind}} = 10.6$ ms^{-1}

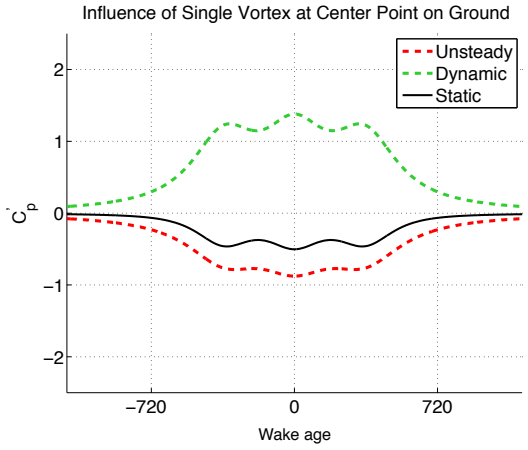

(e) $V_{\text{ind}} = 10.0$ ms^{-1}

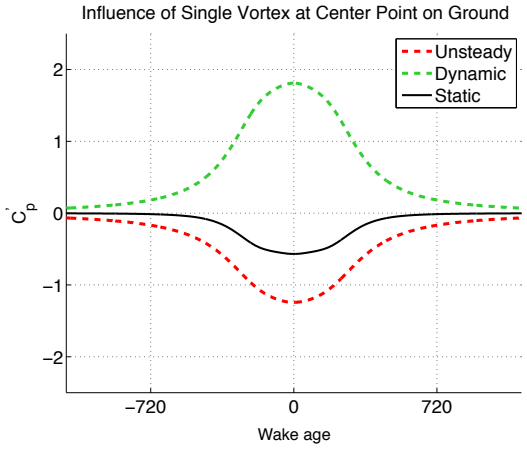

(f) $V_{\text{ind}} = 12.0$ ms^{-1}

Figure 3.21: Pressure predictions from the unsteady flow model for three induced velocities and two vortex spacings.

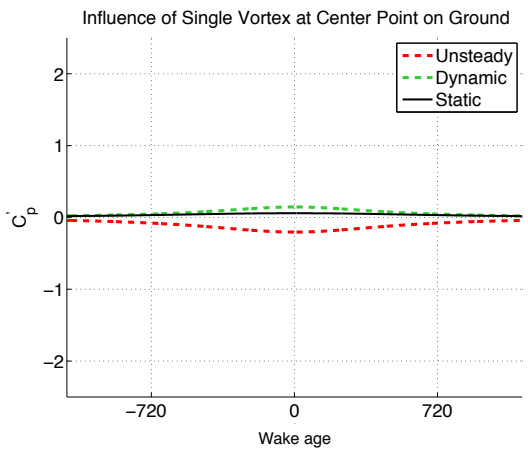

(a) $Z_v = 0.5R$

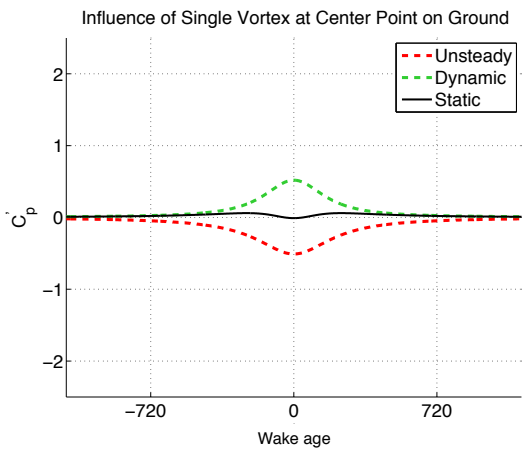

(b) $Z_v = 0.2R$

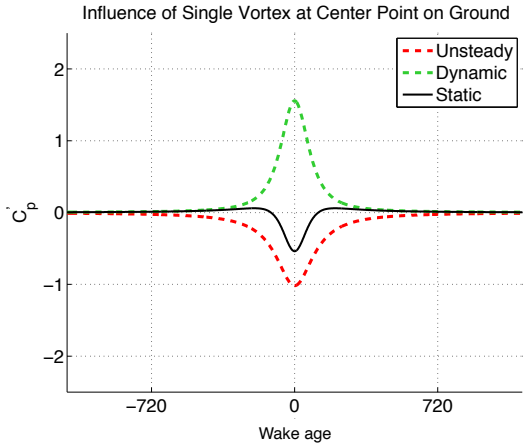

(c) $Z_v = 0.1R$

Figure 3.22: Outlining the sensitivity of the pressure response to vortex height above the ground.

Figure 3.22 compares the pressure response found while varying the height of the vortex above the ground. At a vortex height of $Z_v = 0.5R$, the model predicted a small, but slightly positive static pressure; see Fig. 3.22(a). Reducing the vortex to $Z_v = 0.2R$, the predicted static pressure decreased, becoming slightly negative, as shown in Fig. 3.22(b). However, further decreasing the vortex height from $0.2R$ to $0.1R$ created a significantly negative static pressure (or suction pressure); compare Figs. 3.22(b) and Fig. 3.22(c). Therefore, as the vortex approached the ground,

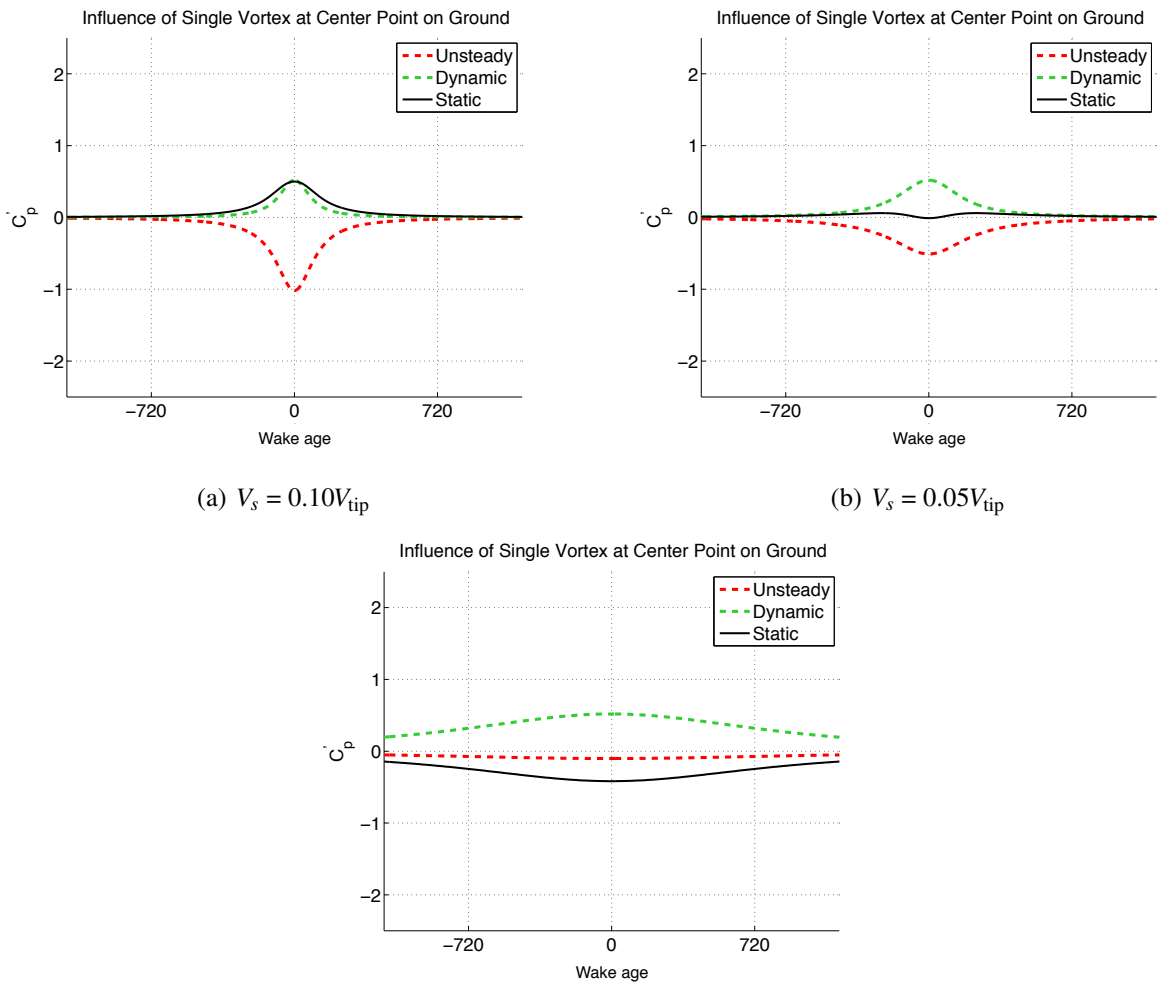

(a) $V_s = 0.10V_{\text{tip}}$

(b) $V_s = 0.05V_{\text{tip}}$

(c) $V_s = 0.01V_{\text{tip}}$

Figure 3.23: Outlining the sensitivity of the pressure response to vortex convection speed along the ground.

the static pressure was found to decrease, and for vortices very near the ground a significant suction pressure was created.

Figure 3.23 compares the pressure response found while varying the vortex convection velocity. For a vortex convecting at $V_s = 0.10V_{\text{tip}}$, the model predicted a distinct pulse in static pressure; see Fig. 3.23(a). As the convection velocity was reduced to $V_s = 0.05V_{\text{tip}}$, no pulse was seen. In fact, Fig. 3.23(b) shows the static pressure at the ground was changed very little by the passage

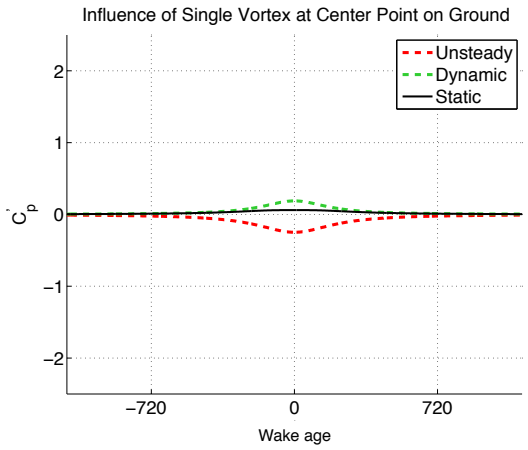

(a) $\Gamma_v = 0.09$ m^{2}s^{-1}

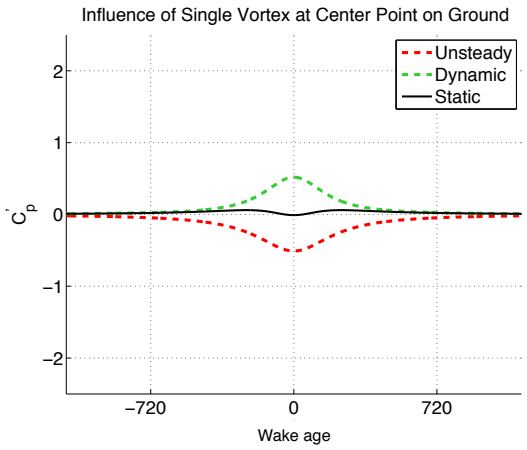

(b) $\Gamma_v = 0.18$ m^{2}s^{-1}

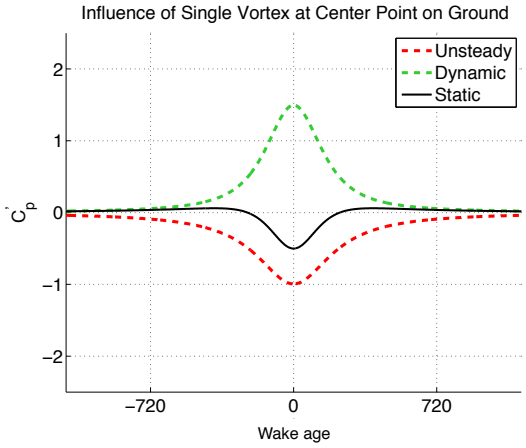

(c) $\Gamma_v = 0.36$ m^{2}s^{-1}

Figure 3.24: Outlining the sensitivity of the pressure response to vortex strength.

of this slower vortex. However, decreasing the vortex convection velocity to $0.01V_{\text{tip}}$ created a negative static pressure, as shown in Fig. 3.23(c). Therefore, the static pressure was found to be sensitive to the vortex convection velocity, i.e., because higher velocities created pressure pulses and smaller velocities produced suction pressures.

Figure 3.24 compares the pressure response while varying the strength of the vortex. For a vortex of strength $\Gamma_v = 0.09$ m^{2}s^{-1}, there was little effect on the predicted static pressure; see

Fig. 3.24(a). Doubling the vortex strength to $\Gamma_v = 0.18$ m^{2}s^{-1}, the static pressure was changed, decreasing to a slightly negative value as shown in Fig. 3.24(b). However, again doubling the vortex strength to a final value of $\Gamma_v = 0.36$ m^{2}s^{-1} produced a significant decrease in the static pressure, as shown in Fig. 3.24(c). Therefore, the static pressure was found to have a sensitivity to vortex strength, and sufficiently strong vortices were capable of producing relatively large suction pressures at the ground.

3.7 Method of Synchronizing Data

Because the flow measurements and ground surface pressure measurements were obtained in separate experiments, a time datum had to be established to compare all of the results. The pressure signature for each of the three phases of impingement was previously described. In this section, the frequency of vortex signatures will be examined. A single vortex was tracked from one pressure sensor location to another as it convected outward over the ground. A reference frame was determined in which a rotor blade was parallel to the light sheet; this condition is defined as the time for which blade azimuth angle (ψ) and wake age (ζ) are both zero. The responses for the pressure sensors nearest the vortices imaged in this frame were examined to establish at time at which all of these sensors simultaneously record the signatures associated with the specific flow events. For reference, the sensor locations are indicated by dashed vertical lines in Figs. 3.25–3.28.

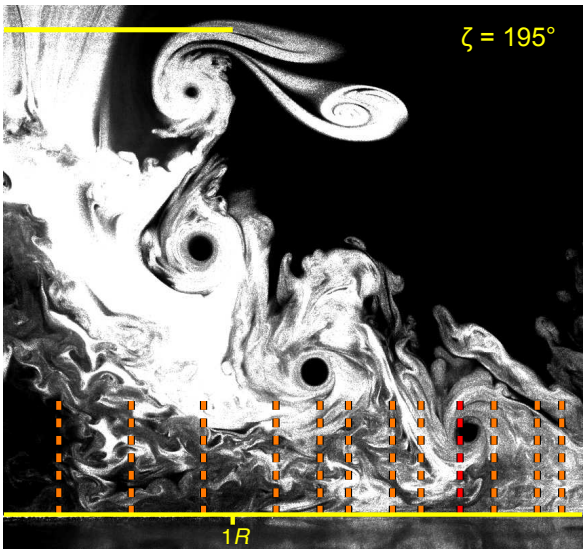

(a) ζ_1

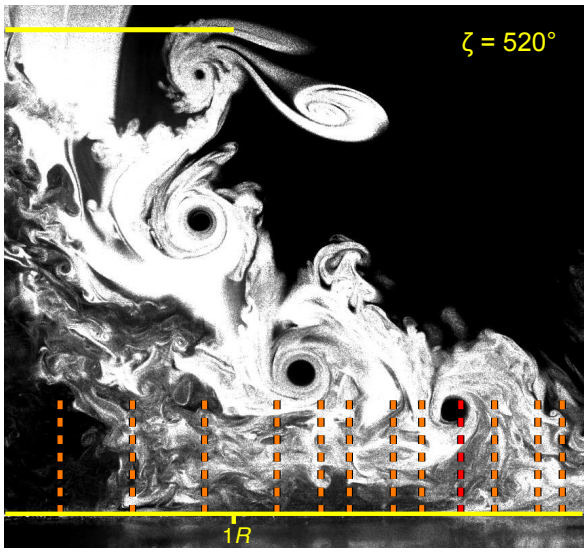

(b) ζ_2

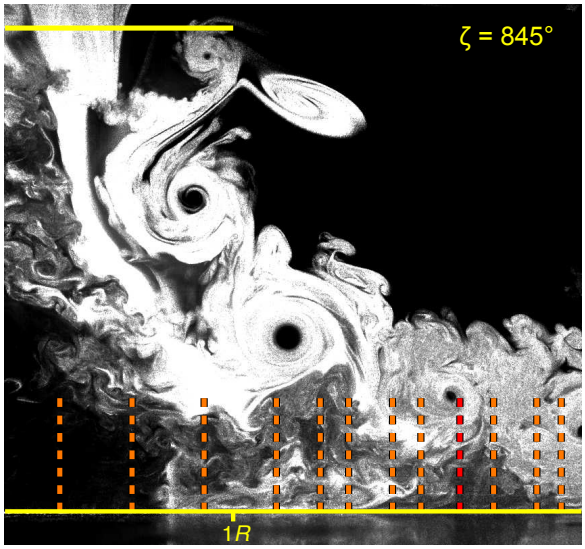

(c) ζ_3

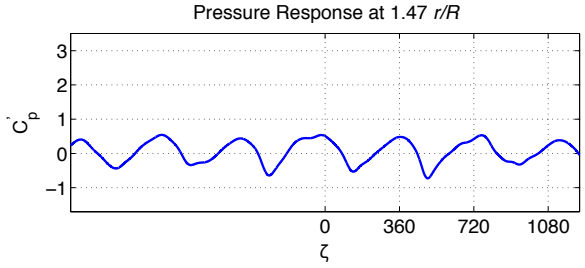

(d) The pressure response measured at 1.47 r/R shows a repeating decrease in pressure that corresponds to the wake ages of the FV images.

Figure 3.25: Each of the FV images show a vortex near the sensor at 1.47 r/R, and the pressure response for that sensor measured a vortex signature near each of the corresponding wake ages.

3.7.1 Vortex Frequency

In this case, the goal was to demonstrate that vortices observed to pass a given sensor location in the FV data can be correlated to the frequency of the pressure fluctuations at that sensor. Figures 3.25(a)–3.25(c) show FV images captured at wake ages of ζ =195, 520, and 845°, respectively. Because the lapse between the capture of these images is near $\Delta\zeta = 360°$, they capture vortices of similar phase passing near the sensor at 1.47 r/R for three consecutive rotor evolutions.

Examining the pressure response measured by this sensor in Fig. 3.25(d), a 1/rev small rounded perturbation appears in-phase with the blade passage over the row of sensors because of the previously described blade passage effect, which can be recorded as far downstream from the rotor as 1.50 r/R. Also, there is a 1/rev suction perturbation that repeats for ζ values near those for which the FV images were captured, i.e., for ζ =195, 520, and 845°. The 1/rev nature of the pressure response is expected because these results were obtained for the one-bladed rotor, and the sawtooth or slant-bottomed trough shape of the suction perturbation matches the event signatures previously identified for the peri-impingement zone in which this sensor (r/R = 1.47) is located.

3.7.2 Vortex Tracking

The passage of a single vortex was tracked as it convected past multiple sensor locations. The FV image in Fig. 3.26(a) captures a vortex near the sensor at r/R = 1.39. Figure 3.26(b) shows the pressure response measured by that sensor. The repeating shape of the response is the consequence of two overlapping, but slightly out of phase event signatures, the positive pressure occurring in-phase with the blade passage (i.e., at $\zeta = 0°, 360°, 720°$, etc.) and the oblique, notched

trough occurring near $\psi = 65^\circ$ (the phase for which the FV image showed a vortex passing above this sensor location).

Figure 3.26(c) shows a later FV image, captured at about $\zeta = 195^\circ$. The same vortex visible in the previous FV image has convected further downstream and now has affected the sensor at 1.47 r/R. The pressure response measured by this sensor again shows the rounded perturbations that are in-phase with blade passage, as well as the 1/rev sawtooth-shaped suction pulse; see Fig. 3.26(d). One such pulse is visible near $\zeta = 195^\circ$, the phase at which a vortex was observed to pass this location, as shown in Fig. 3.26(c).

Figure 3.26(e) shows the effect of the vortex was captured farther downstream near 1.54 r/R at about $\zeta = 260^\circ$. Similar to the other responses, the sensor at 1.54 r/R measured the rounded perturbations of the blade passage effect but offset by a low pressure (suction) trough. The lower pressure at this location is stronger than that shown in Fig. 3.26(d) because the vortex is nearer to the ground plane at this wake age. The trough in the signature at this sensor also occurs at a later phase than is shown in Fig. 3.26(d) (near $\zeta = 260^\circ$), with the time period between them being approximately equal to the distance between the adjacent sensors divided by the convection speed of the vortex.

3.7.3 Synchronization of the Measurements

The next goal of the work was to define a reference image within the FV data to be the datum, and to show that a time exists within the pressure time-histories at which coincident event signatures are recorded by the sensors corresponding to the same radial locations near which the

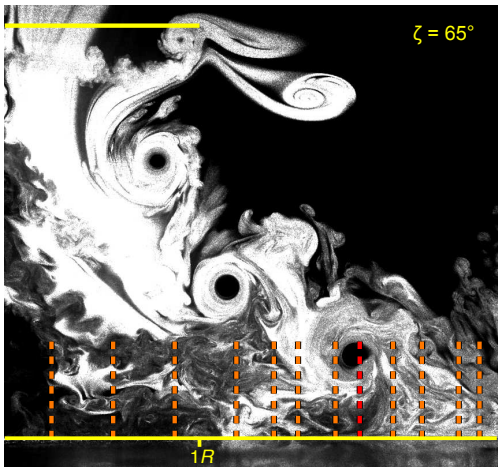

(a) At $\zeta = 0$, a vortex is located near 1.39 r/R.

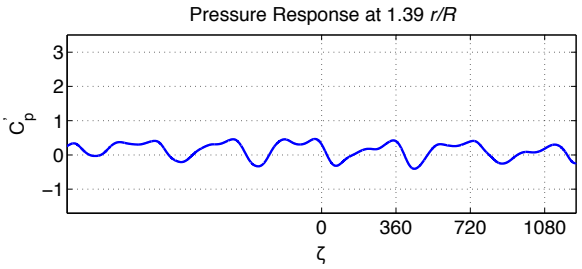

(b) The pressure response measured at 1.39 r/R shows a vortex passing this location near $\zeta = 0$.

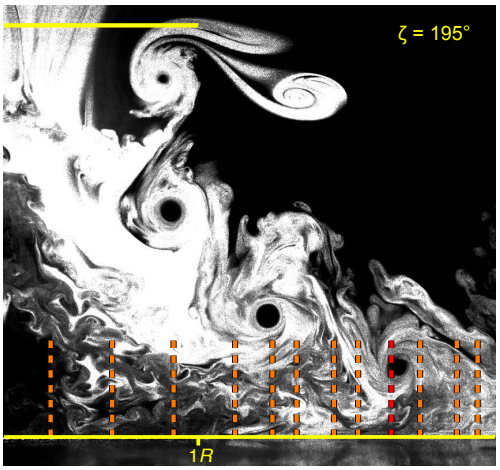

(c) At $\zeta = 195$, a vortex is located near 1.47 r/R.

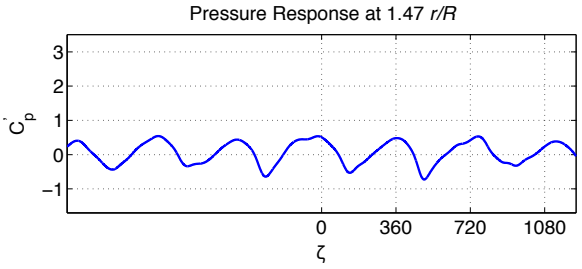

(d) The pressure response measured at 1.47 r/R shows a vortex passing this location near $\zeta = 195$.

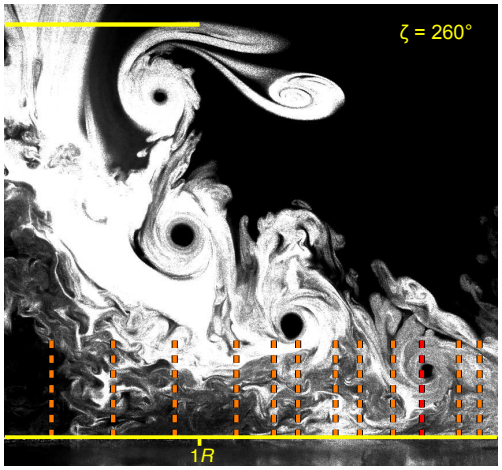

(e) At $\zeta = 260$, a vortex is located near 1.54 r/R.

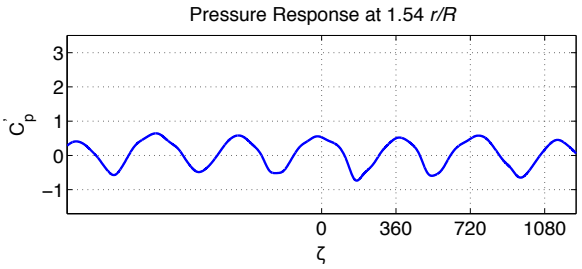

(f) The pressure response measured at 1.54 r/R shows a vortex passing this location near $\zeta = 260$.

Figure 3.26: The FV images track the progress of a single vortex as it passes three sensor locations.

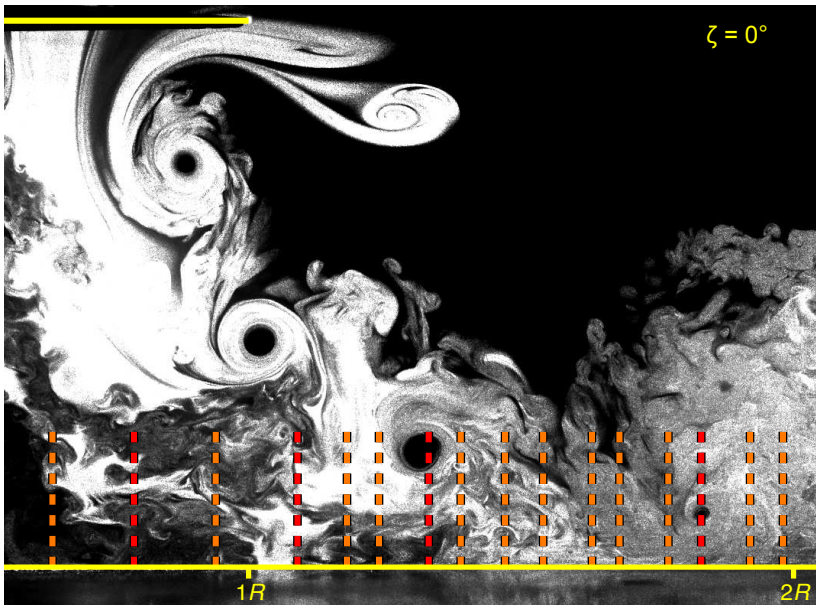

(a) A FV image capturing the rotor blade parallel to the light sheet ($\Delta\zeta = 0$).

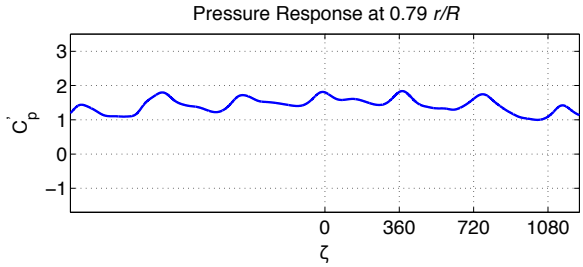

(b) The pressure response at 0.79 r/R showing a peak in-phase with the blade passage over the sensors.

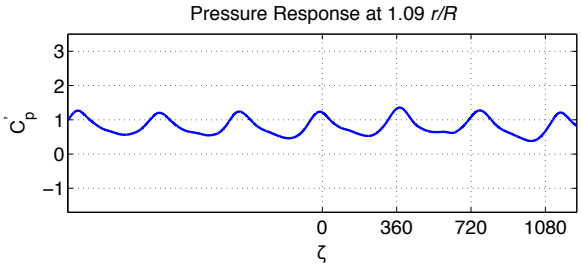

(c) The pressure response at 1.09 r/R showing a peak in-phase with the blade passage over the sensors.

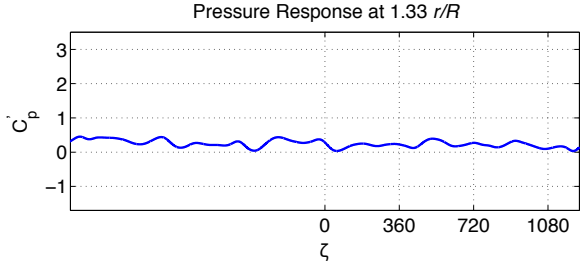

(d) The pressure response at 1.33 r/R showing a peak in-phase with the blade passage over the sensors, followed closely by a decrease in pressure created by the passage of a vortex.

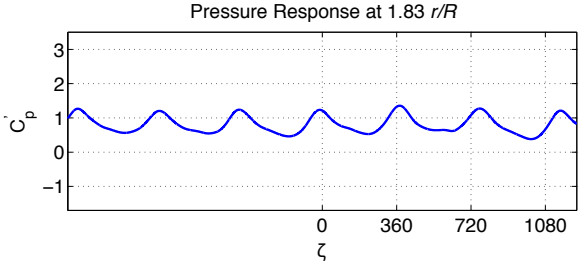

(e) The pressure response at 1.83 r/R showing a decrease in pressure caused by the passage of a vortex, which coincides with the passage of the blade.

Figure 3.27: Locating a datum within the pressure responses that contains signatures corresponding in phase to the flow events, such as blade or vortex passage, as observed in the one-bladed reference FV image.

flow events were observed in the FV images. For the one-bladed rotor, Fig. 3.27(a) shows the reference frame because the spanwise axis of the rotor blade is parallel to the plane of the light sheet, i.e., defined as $\zeta = 0^\circ$. The pressure responses recorded at the sensors at 0.79 and 1.09 r/R showed smooth peaks occurring in-phase with the each blade passage over the sensors (i.e., at $\zeta = 0^\circ, 360^\circ, 720^\circ$, etc.). The shape of the pressure response recorded at 1.33 r/R was more complex, however, because it captures the interaction of two flow events occurring in close succession; the positive perturbation from the blade passage effect is followed immediately by a decrease in the pressure because of a vortex passing over this location an instant later. The reference image frame in Fig. 3.27(a) also shows a vortex near 1.83 r/R. Figure 3.27(e) shows a decrease in the pressure response at $\zeta = 0^\circ$, which corresponds to the proximity of a vortex at that time, as shown in Fig. 3.27(a).

In a similar fashion, a reference image for the two-bladed rotor that captured a blade parallel to the light sheet was selected to be the datum for this data set; see Fig. 3.28(a). The pressure responses for the sensors located at 0.94 and 1.09 r/R, as shown in Figs. 3.28(b) and 3.28(c), recorded the blade passage effect in that they showed smooth rounded peaks at $\zeta = 0^\circ, 180^\circ, 360^\circ$, etc. Figure 3.28(d) also shows the blade passage signature, but this is also followed soon after by a decrease in pressure. The timing of this decrease in pressure matches the order of events captured in the FV reference frame (see Fig. 3.28(a)), which shows a vortex slightly upstream but approaching this sensor location at this instance at $\zeta = 0^\circ$. The response measured at 1.54 r/R shows the characteristics 2/rev peaks of the blade passage effect as well, but the peak occurring at $\zeta = 0^\circ$ is of smaller magnitude as compared to adjacent peaks. As shown in Fig. 3.28(a), this

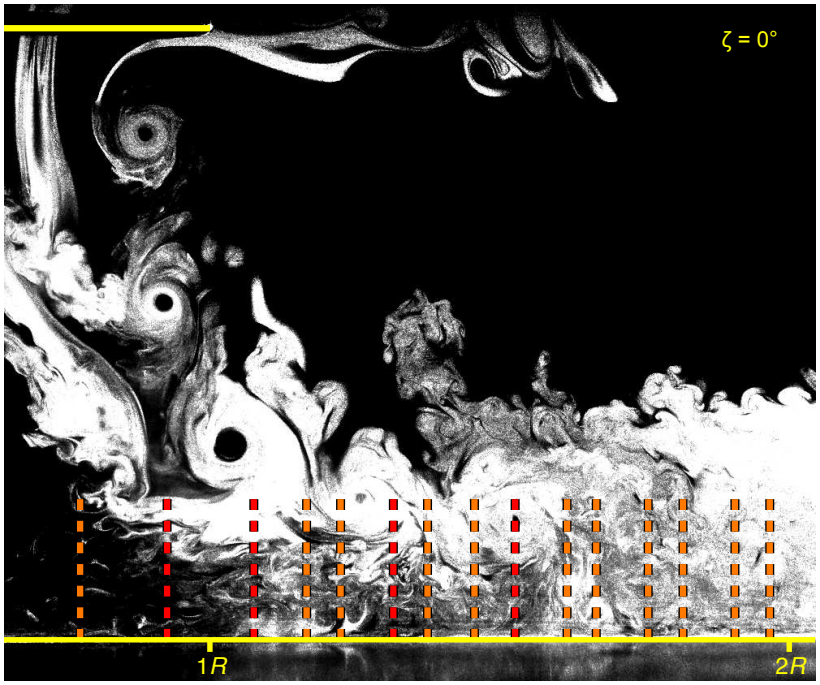

(a) A FV image capturing a rotor blade parallel to the light sheet ($\Delta\zeta = 0$).

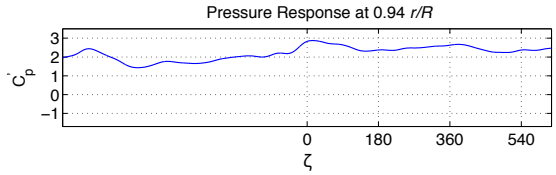

(b) The pressure response at 0.94 r/R showing a peak in-phase with the blade passage over the sensors.

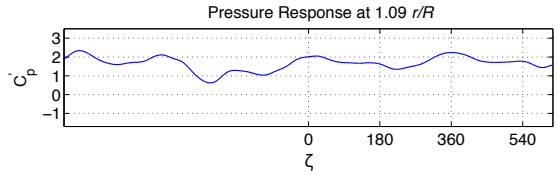

(c) The pressure response at 1.09 r/R showing a peak in-phase with the blade passage over the sensors.

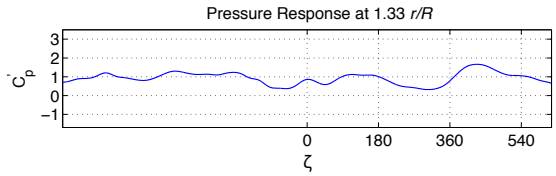

(d) The pressure response at 1.33 r/R showing a peak in-phase with the blade passage over the sensors, followed closely by a decrease in pressure created by the passage of a vortex.

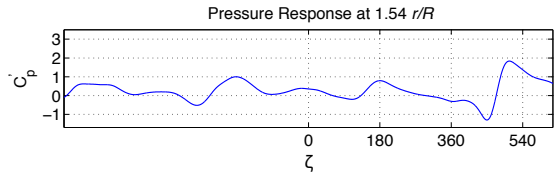

(e) The pressure response at 1.54 r/R showing a peak at $\zeta = 0$; the combined result of simultaneous blade and vortex passage effects.

Figure 3.28: Locating a datum within the pressure responses that contains signatures corresponding in phase to the flow events, such as blade or vortex passage, as observed in the two-bladed reference FV image.

reduced magnitude may be because of two flow events coinciding: 1. the blade passage, which creates positive pressure, and 2. the passage of a vortex, which can create a negative pressure. The combined effects are likely then to produce smaller pressure fluctuations for those combined and almost coincident events.

3.8 Analysis of Measured Results

Further analysis of the PIV, PTV, and surface pressure measurements is discussed in this section. Regions below the vortices near the bed were examined to see if and how sediment particle mobilization occurred. Instances where there were fluctuations in flow velocity and unsteady pressure on the ground plane were examined to look for increases sediment uplift. The corresponding particle flux in both the wall-normal and wall-parallel directions were also calculated. The relationship between sediment height and the proximity of the vortices to the bed was examined. Furthermore, any significant deviations of the particle trajectories from the primary directions of the carrier flow were quantified.

3.8.1 Particle Concentrations Near Vortices

Maps of particle concentration were generated from the image intensity data in the dispersed phase. Pixels having an intensity of 1,000 or greater were regarded as sediment particles. A binning method was used to quantify the concentrations. This process was performed by dividing the image into a grid of 2×2 pixel bins and pixels above the specified intensity value were added to each bin. The aggregate values in the bins were then plotted as contours to produce a map of

particle concentrations. To complete this form of analysis, the concentration map was overlaid with the corresponding velocity vector field, the vectors being generated from the u and v flow velocity components that were obtained from the PIV analysis.

Figures 3.29–3.32 show concentration maps and velocity fields that were produced by each rotor (i.e., one-bladed and two-bladed). The yellow dots indicate the r/R locations where ground pressure measurements were obtained. Figure 3.29 shows results for the near-ground region within the wake impingement zone that were produced by the one-bladed rotor. Waves of particle concentrations can be seen to convect directly beneath some of the vortices. The exact location of the particle concentration relative to a vortex is more clearly identified in the detailed results shown in Fig. 3.30. It is important to notice that particle concentrations were observed to occur below the center or core of the vortices and not just ahead of the vortices in regions of strong vertical upwash.

The vertical uplift of particles in the absence of large wall-normal (v) velocities could indicate the presence of another force acting on the particle bed in addition to the boundary layer shear; i.e., a vortex-induced pressure effect. Of course, Saffman forces or, if the particles were spinning at significant rates, Magnus forces could also create lift on the particles and may affect their trajectories. Given their spherical shape, however, it is unlikely that any small spin velocities that originate while the particles first creep along the bed would be high enough to produce significant Magnus forces, or that the particle spin would increase or be sustained once the spherical particles were entrained into the flow. Furthermore, prior work by Zou [22] indicated that the Magnus force is likely larger in magnitude than the Saffman force, so any effects on particle motion resulting from the Saffman force would be even less significant than those produced by the Magnus force.

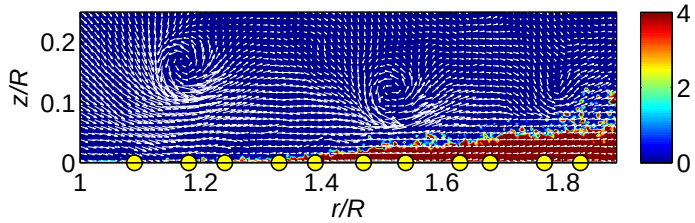

(a) $\zeta = \zeta_0$

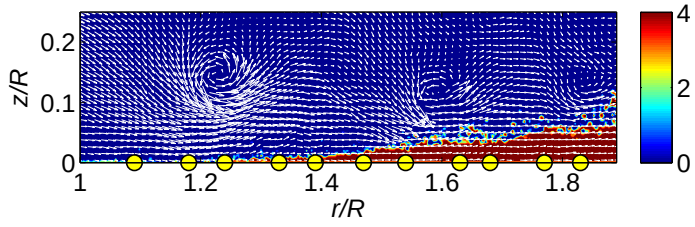

(b) $\zeta = \zeta_0 + 65°$

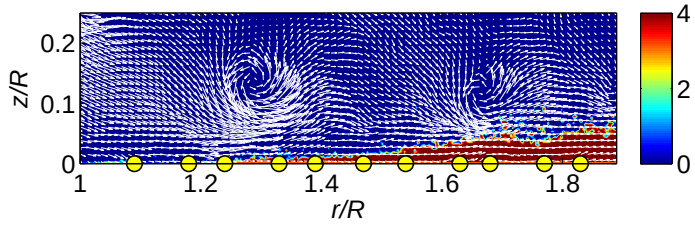

(c) $\zeta = \zeta_0 + 130°$

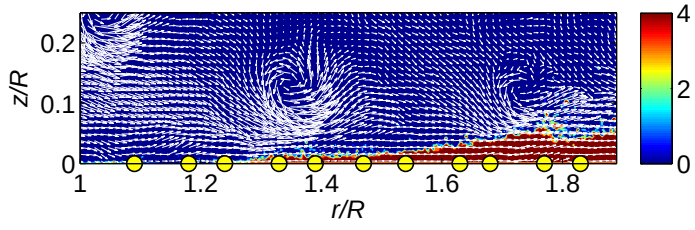

(d) $\zeta = \zeta_0 + 195°$

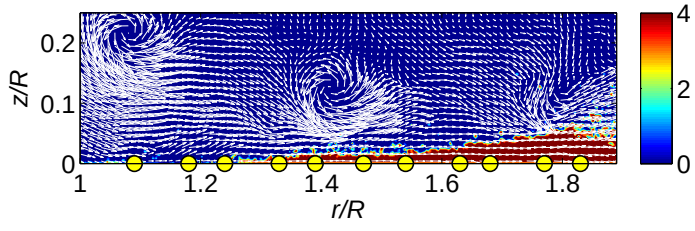

(e) $\zeta = \zeta_0 + 260°$

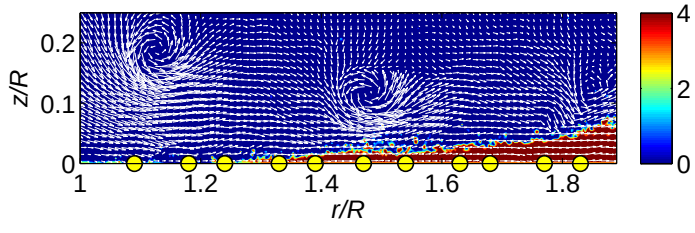

(f) $\zeta = \zeta_0 + 325°$

Figure 3.29: Maps of particle concentration for the one-bladed rotor at 1.0 z/R and 130 Hz.

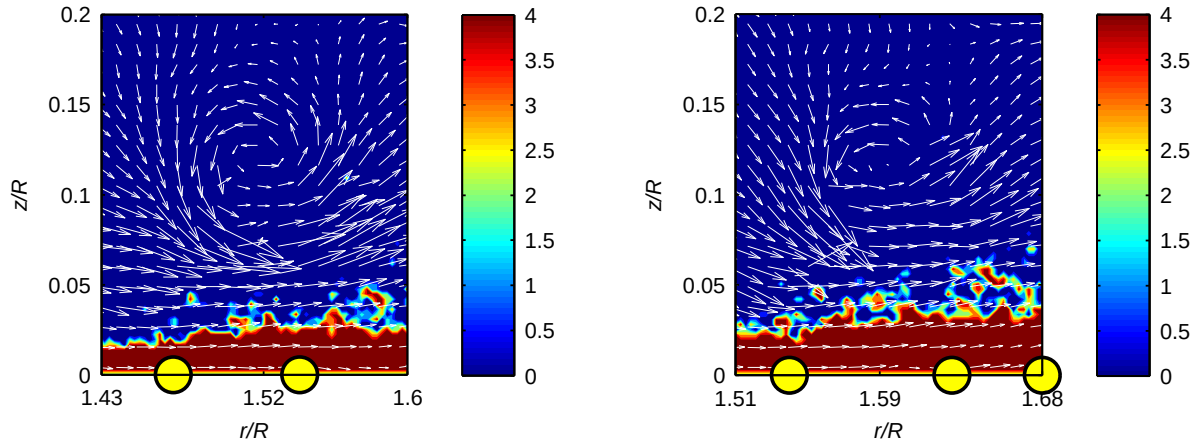

(a) $\zeta = \zeta_0$

(b) $\zeta = \zeta_0 + 65°$

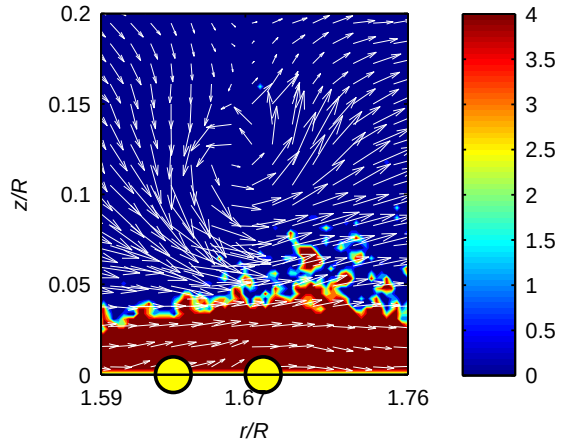

(c) $\zeta = \zeta_0 + 130°$

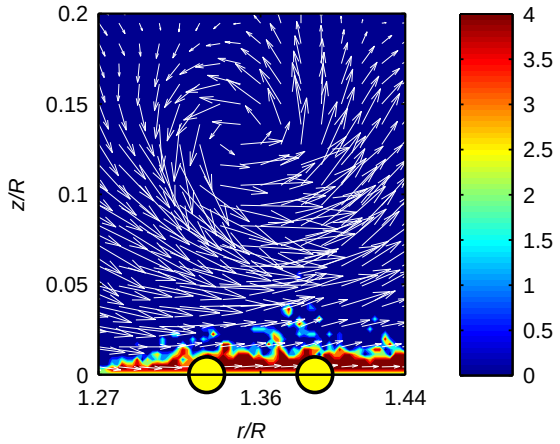

(d) $\zeta = \zeta_0 + 195°$

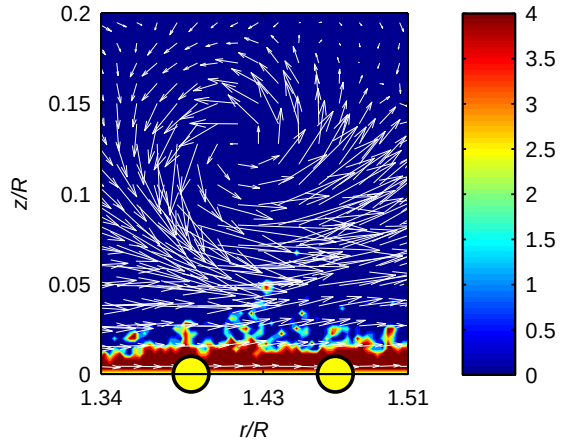

(e) $\zeta = \zeta_0 + 260°$

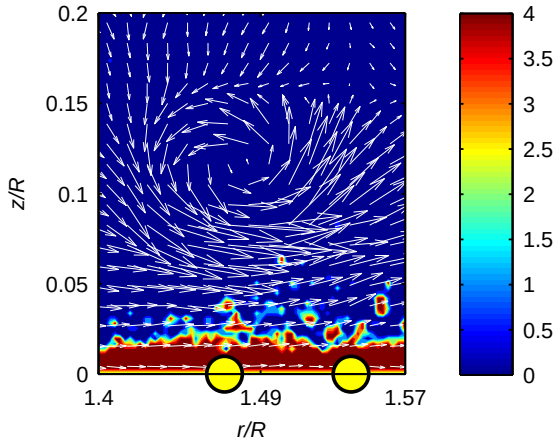

(f) $\zeta = \zeta_0 + 325°$

Figure 3.30: Detailed maps of particle concentration for the one-bladed rotor at 1.0 z/R and 130 Hz.

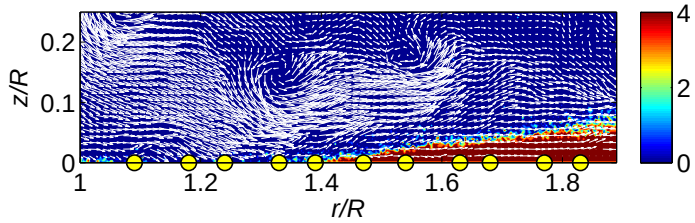

(a) $\zeta = \zeta_0$

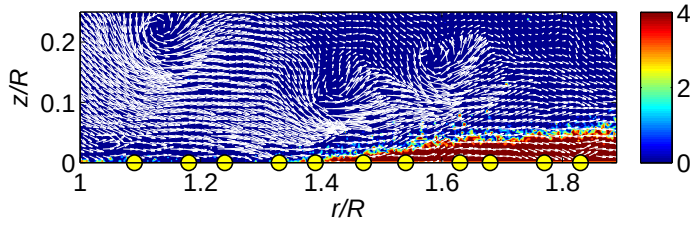

(b) $\zeta = \zeta_0 + 65°$

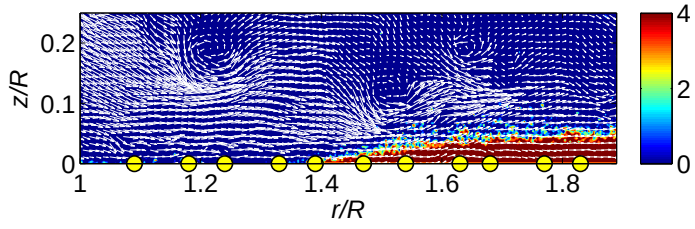

(c) $\zeta = \zeta_0 + 130°$

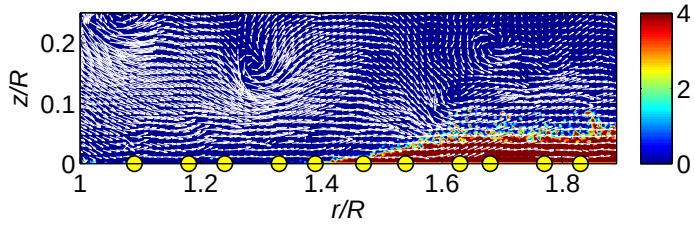

(d) $\zeta = \zeta_0 + 195°$

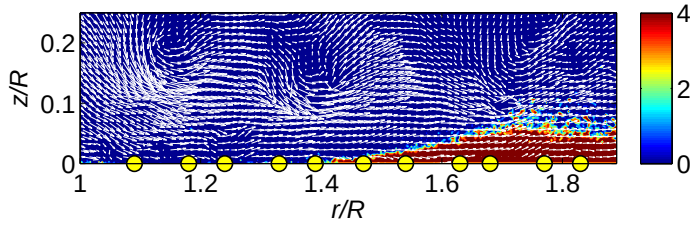

(e) $\zeta = \zeta_0 + 260°$

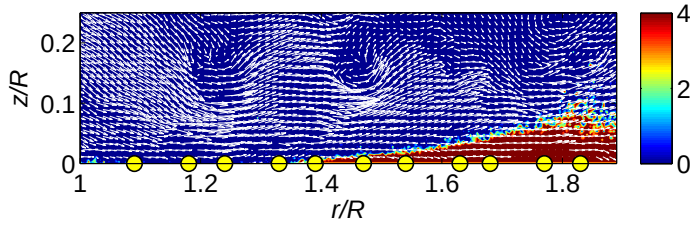

(f) $\zeta = \zeta_0 + 325°$

Figure 3.31: Maps of particle concentration for the two-bladed rotor at 1.0 z/R and 130 Hz.

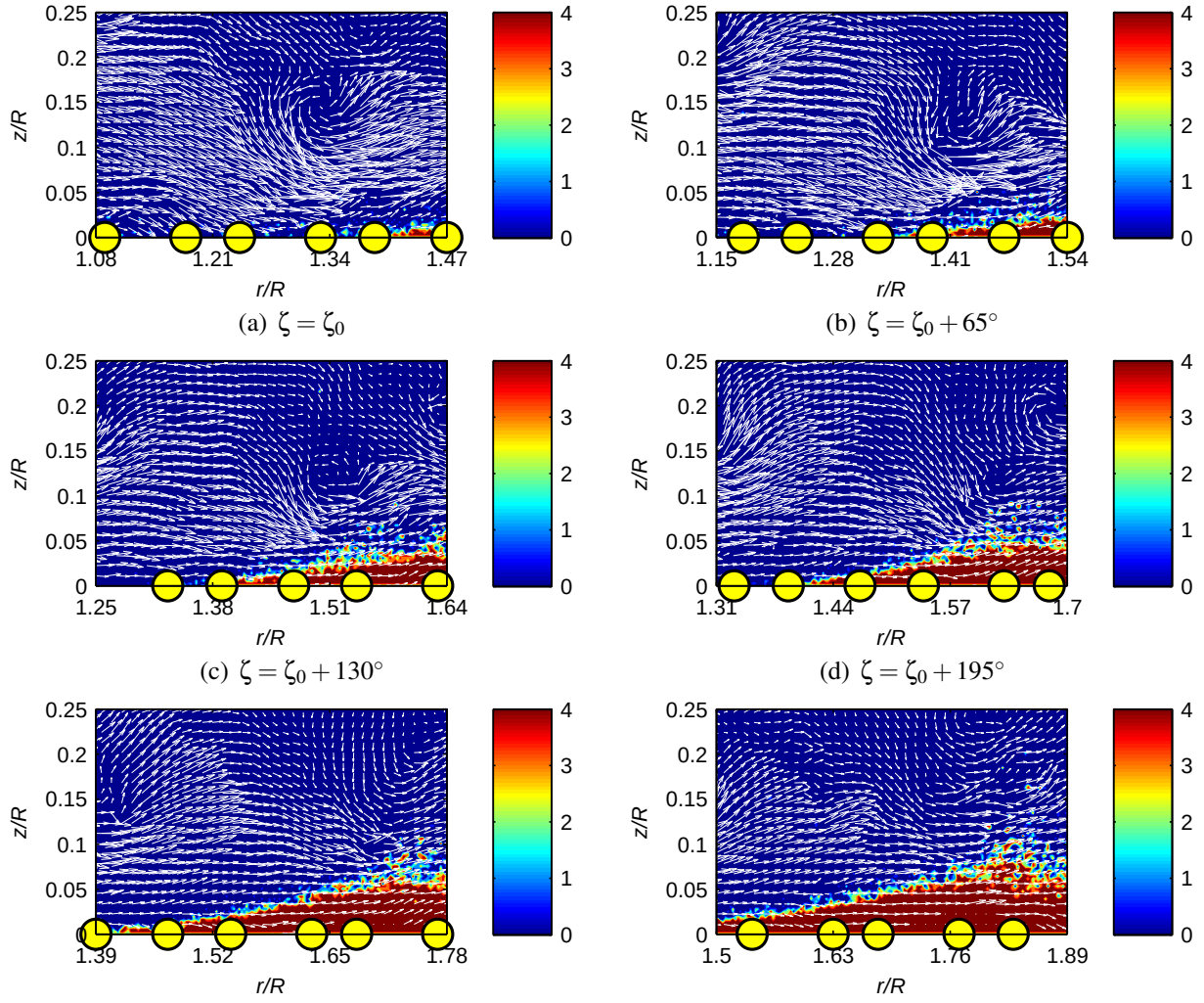

(a) $\zeta = \zeta_0$

(b) $\zeta = \zeta_0 + 65°$

(c) $\zeta = \zeta_0 + 130°$

(d) $\zeta = \zeta_0 + 195°$

(e) $\zeta = \zeta_0 + 260°$

(f) $\zeta = \zeta_0 + 325°$

Figure 3.32: Detailed maps of particle concentration for the two-bladed rotor at $1.0z/R$ and 130 Hz.

This same behavior was also seen for the two-bladed rotor, as shown in Figure 3.31. For this case, there are more vortex-vortex interactions in the flow near the bed, so clusters of more and less vorticity can sometimes be observed. Figure 3.32 shows more clearly that waves of particle concentrations were again produced directly below the vortices and convect with them in the flow. In effect, the presence of the vortices appear to be producing an effect with a magnitude sufficient to exceed the gravitational and inter-particle forces, uplifting the particles from the sediment bed and carrying them along into the flow.

3.8.2 Fluctuating Velocity and Pressure Effects on Particle Uplift

To support the hypothesis that the presence of a vortex-induced negative (or suction) pressure can lower the thresholds for sediment mobility and entrainment to dislodge and uplift more particles to higher heights, the existence of correlations between the velocity fluctuations, the uplift heights of the sediment particles, and the pressure measurements were investigated. For this study, a series of 56 consecutive dual-phase flow realizations were examined for the one-bladed rotor; only half as many realizations were used in the case of the two-bladed rotor to capture the same number of flow events.

The flow velocities, surface pressures, and quantity of sediment uplift were all compared at the same radial location. This location was selected because particle concentrations were observed to convect beneath the vortices there, as shown in the concentration maps previously presented in Figs. 3.30 and 3.32. For the one-bladed rotor, a radial location of 1.54 r/R was selected, while the flow generated by the two-bladed rotor was examined farther downstream at 1.77 r/R.

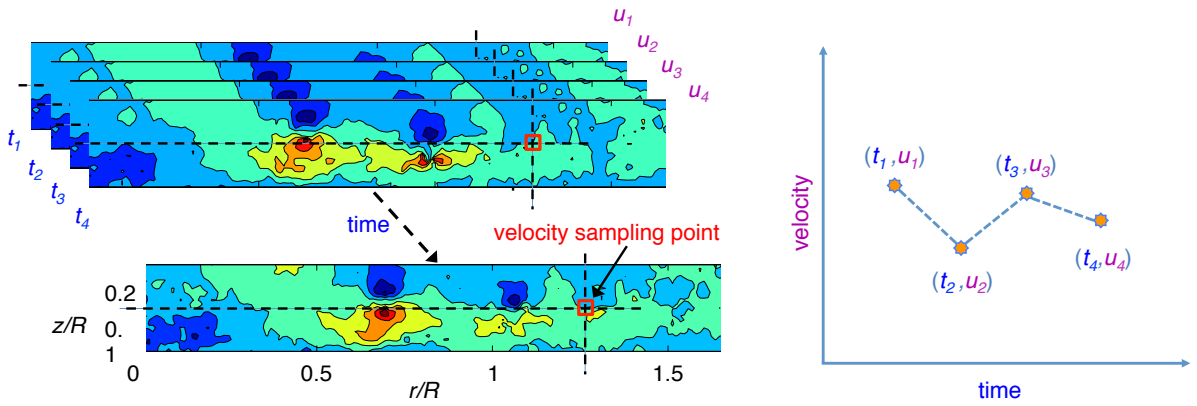

(a) Schematic illustrating the sampling of velocity at a given point for a series of frames.

(b) Example of plotting the components of velocity versus time.

Figure 3.33: Explanation of the method used to extract the time-history of the velocity components for given point in the flow field.

To extract the fluctuations of the velocity components from PIV data, the height of the sampling location within the flow must also be selected; see Fig. 3.33. Heights within the 0–0.25 z/R range showed the greatest fluctuations in the v-velocity component and so were selected as the primary sampling location. The greatest v-velocity fluctuations were measured to occur at a height of 0.17 z/R for the one-bladed rotor flow field and at a height of 0.13 z/R for the two-bladed rotor.

To determine the maximum height to which mobilized sediment particles were lifted at each selected radial location, a rectangular ROI was utilized; see Fig. 3.34. The intensity of pixels within the ROI (sized to a height of 0.18 z/R and a length equal to 5% of the blade chord) were evaluated using the threshold method. Again, pixels displaying an intensity of greater than 1,000 were considered to be sediment particles. To find the highest instances of sediment uplift within the ROI, the pixels contained therein were examined row by row, starting from the top of the ROI and working down. The maximum height of the sediment was considered to have been identified once a 3×3 pixel cluster was found having at least 6 of 9 pixels with sufficient intensities.

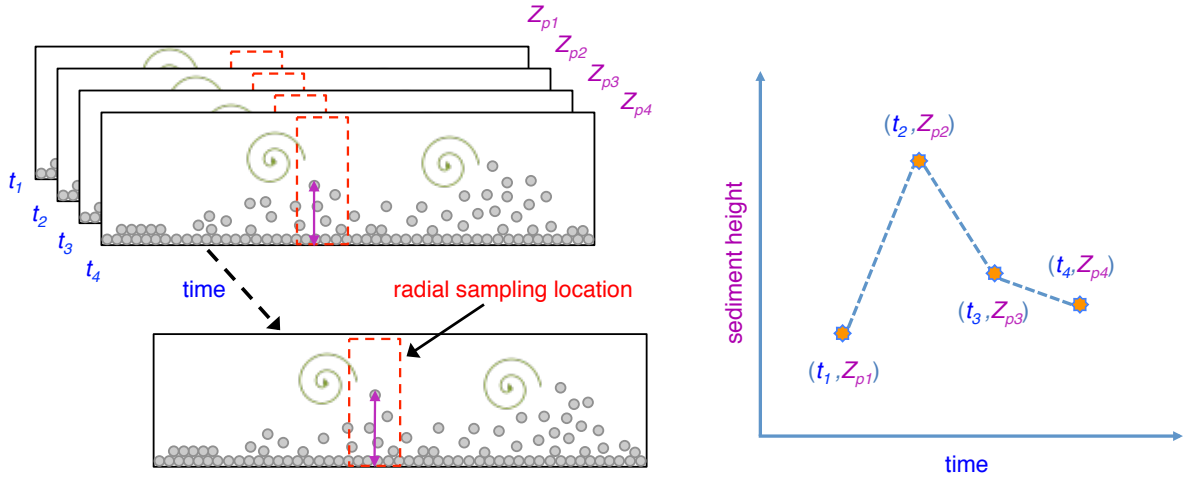

(a) Schematic illustrating the determination of sediment height for a series of frames.

(b) Example of plotting the height of sediment versus time.

Figure 3.34: Explanation of the method used to extract the time-history of sediment height above the ground for a given radial location.

Figures 3.35 and 3.36 compare the velocity components for the one-bladed and two-bladed rotors, respectively. The results show that the v-velocity fluctuates over a much wider range of values than does the u-velocity. While the u-velocity remains predominantly positive, the v-velocity fluctuates between positive and negative extremes. The positive and negative peaks of v-velocity, taken as pairs, occur at a frequency of once-per-rotor revolution (or 1/rev) for the one-bladed rotor and indicate the presence of a passing vortex.

Figures 3.37 and 3.38 compare the fluctuations in the v-velocity to the maximum height to which the sediment particles are convected for the one-bladed and two-bladed rotors, respectively. While some increases in the sediment height appear to coincide with positive increases in the v-velocity, that is not necessarily the case. For example, for the one-bladed rotor the first peak occurs when the v-velocity is near zero and is flanked on either side by substantially negative v-velocities. Also, the sediment convection height remained low for instances where the v-velocity achieves its

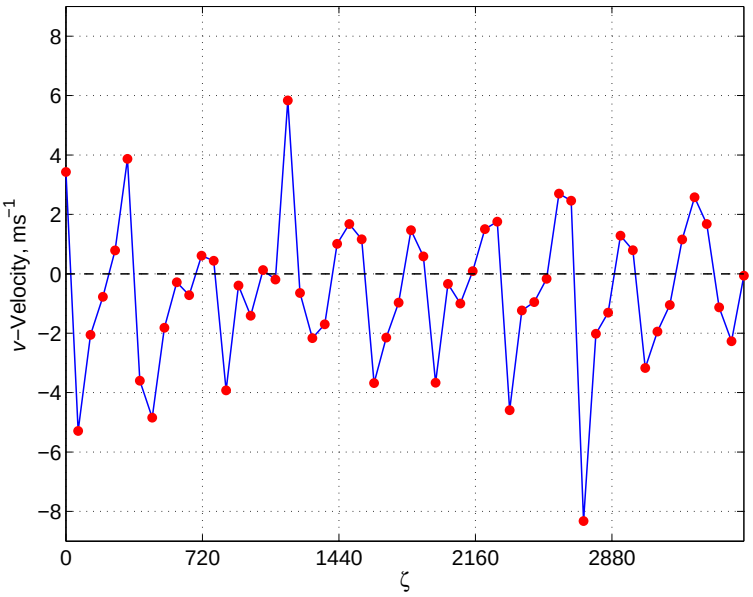

(a) *v*-velocity.

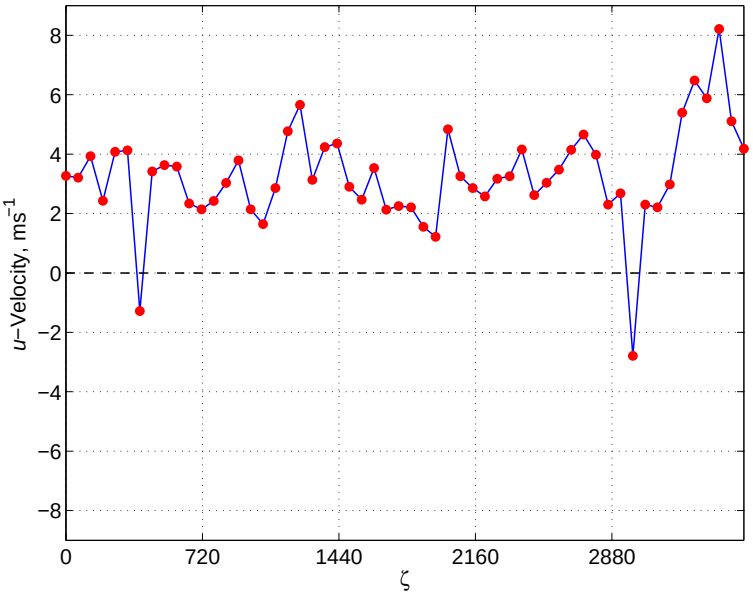

(b) *u*-velocity.

Figure 3.35: Time-history of *v*- and *u*-velocities for one-bladed rotor.

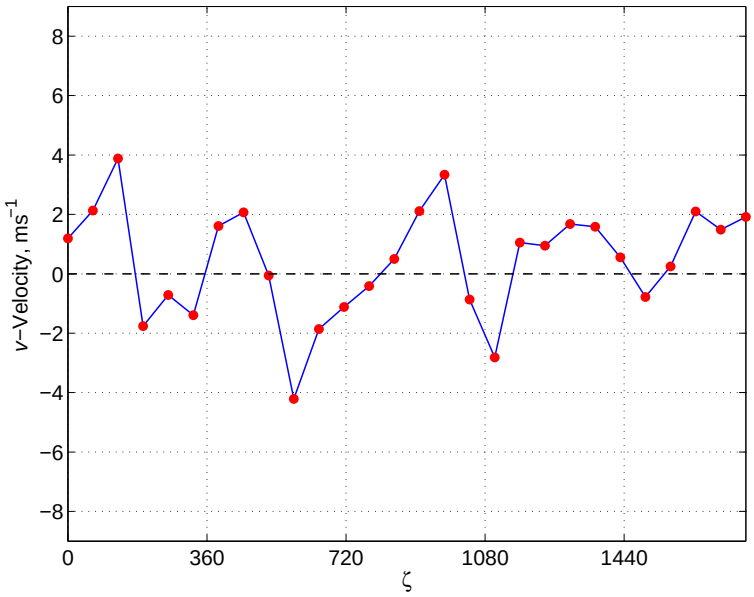

(a) v-velocity.

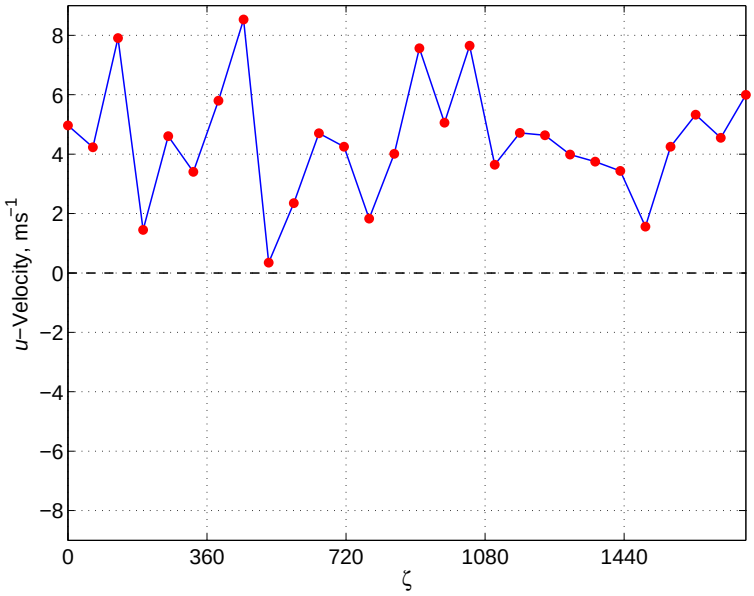

(b) u-velocity.

Figure 3.36: Time-history of v- and u-velocities for two-bladed rotor.

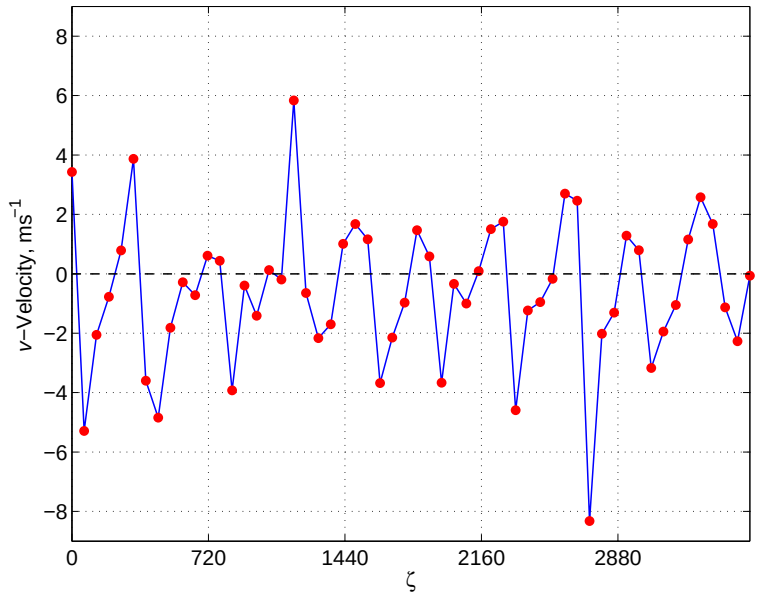

(a) v-velocity.

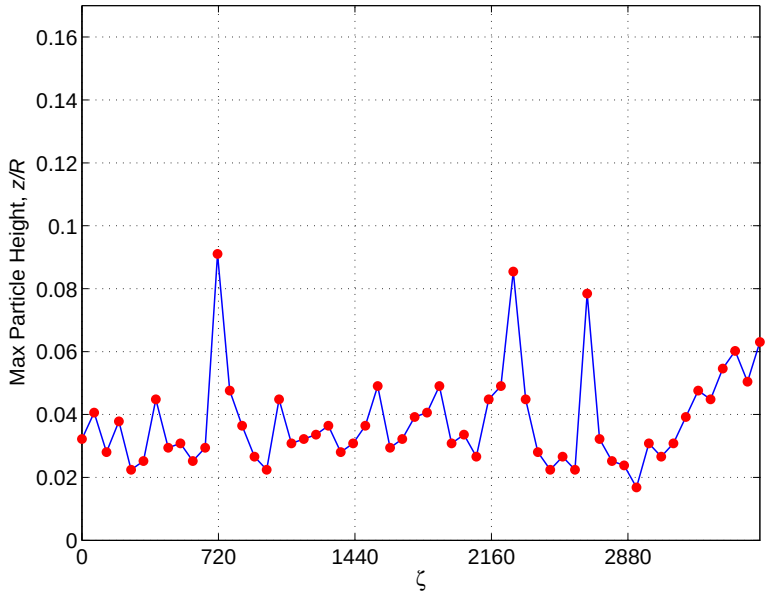

(b) The height of uplifted sediment particles.

Figure 3.37: Time-history of v-velocity and particle uplift for one-bladed rotor.

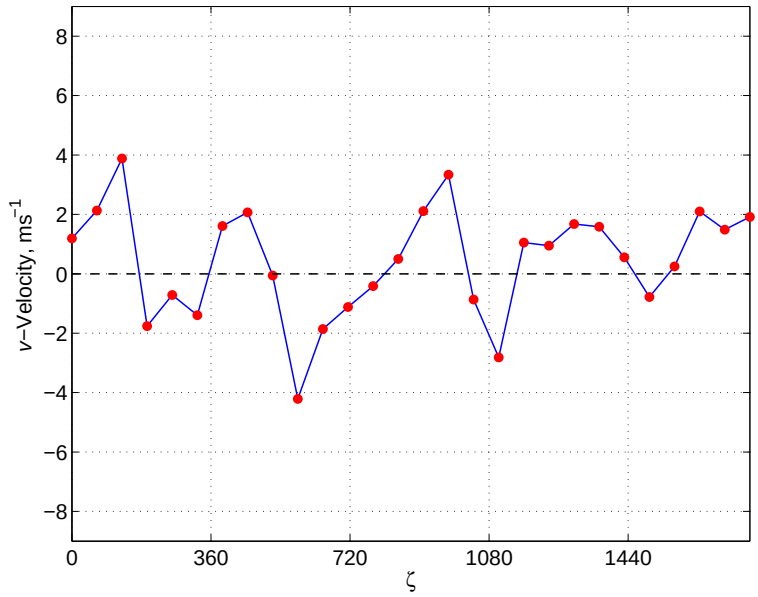

(a) v-velocity.

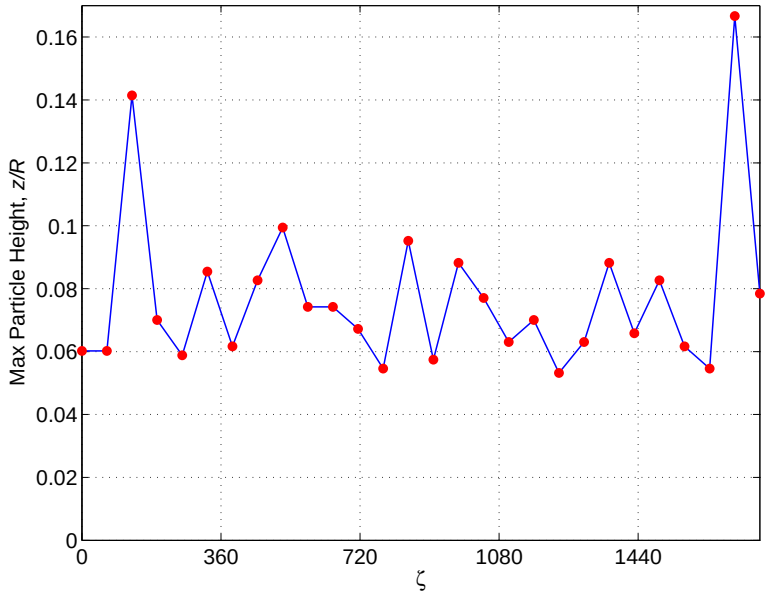

(b) The height of uplifted sediment particles.

Figure 3.38: Time-history of v-velocity and particle uplift for two-bladed rotor.

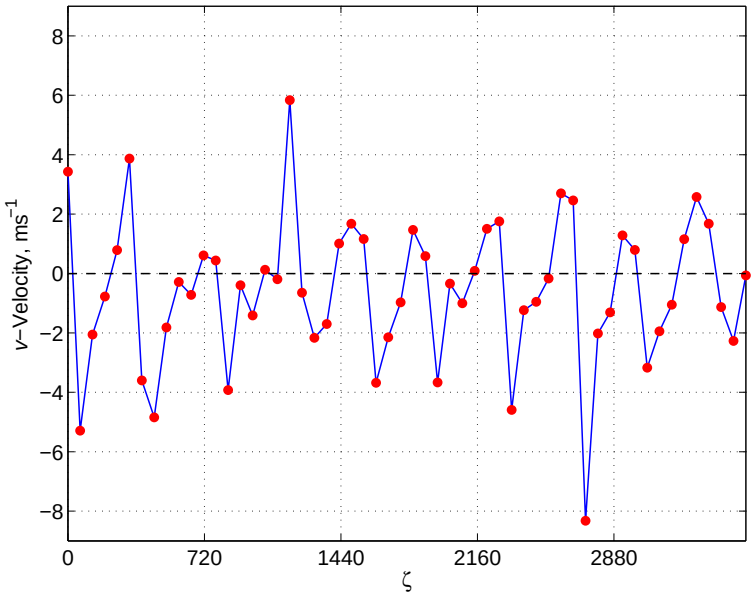

(a) v-velocity.

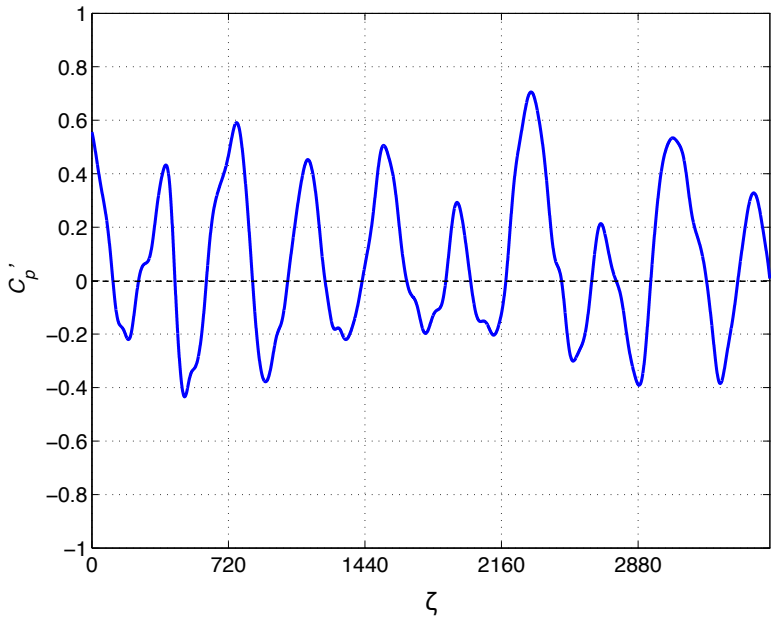

(b) The pressure response.

Figure 3.39: Time-history of v-velocity and pressure at 1.51 r/R for one-bladed rotor.

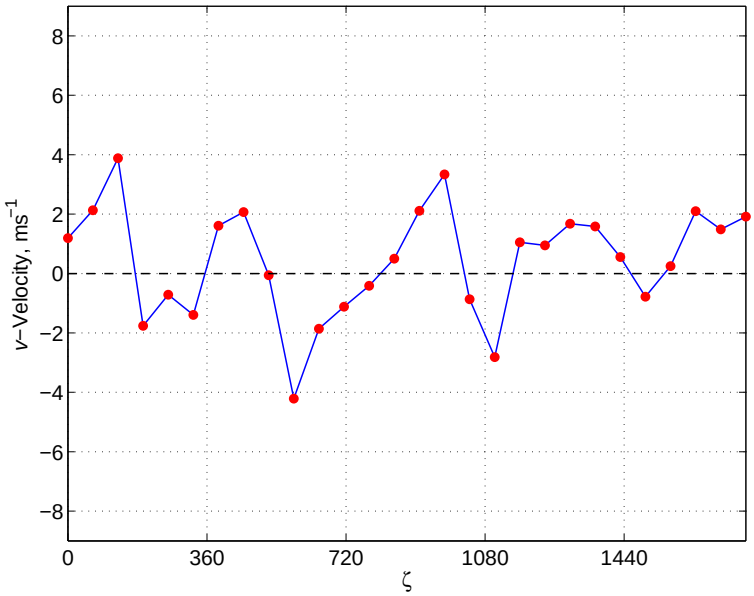

(a) v-velocity.

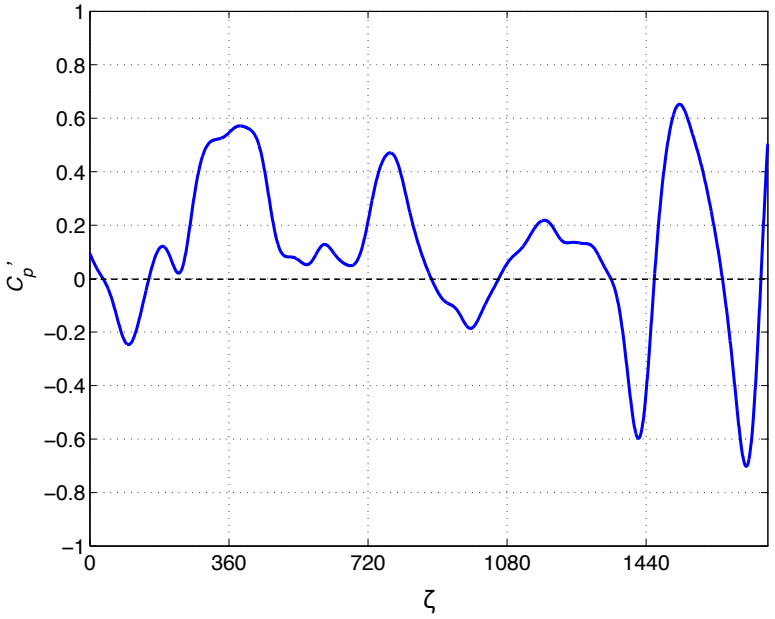

(b) The pressure response.

Figure 3.40: Time-history of v-velocity and pressure at 1.51 r/R for two-bladed rotor.

largest positive peak, which is near $\zeta = 1,100^\circ$; compare Figs. 3.37(a) and 3.37(b). In the case of the two-bladed rotor, the third largest height to which the sediment is convected occurs when the v-velocity is almost zero near $\zeta = 500^\circ$; compare Figs. 3.38(a) and 3.38(b).

Figures 3.39 and 3.40 compare the fluctuations in v-velocity to the pressure responses on the bed as produced by both rotors. Again, the individual vortex signatures are not as clearly visible in the v-velocity nor are they in the pressure responses produced by the two-bladed rotor as compared to the one-bladed rotor. Closer examination of Figs. 3.39(a) and 3.39(b) shows that decreases in the suction pressure occur when the v-velocity fluctuates between extreme positive and negative values. The 1/rev v-velocity fluctuations were already identified as an indication of the presence of a vortex in the flow, which is further evidence that the vortices convecting near the ground can produce lower (suction) pressures there, albeit of a transient nature.

3.8.3 Particle Fluxes

To quantify the number of particles fluxing in both the r and z directions, the flow field was divided into a Cartesian grid. The resulting cells were considered to have unit depth because the measured data were a two-dimensional representation of a three-dimensional flow field. Cosidering the flow field in this way is reasonable because all transient events that occur in the three-dimensional volume will inevitably occur at the plane of interest at some point in time. Using the velocity information for airborne particles obtained from the PTV analysis, and assuming that the particles convect in a straight trajectory during the time step, the future position of each particle was predicted. While translating from the old position to the predicted future position, it

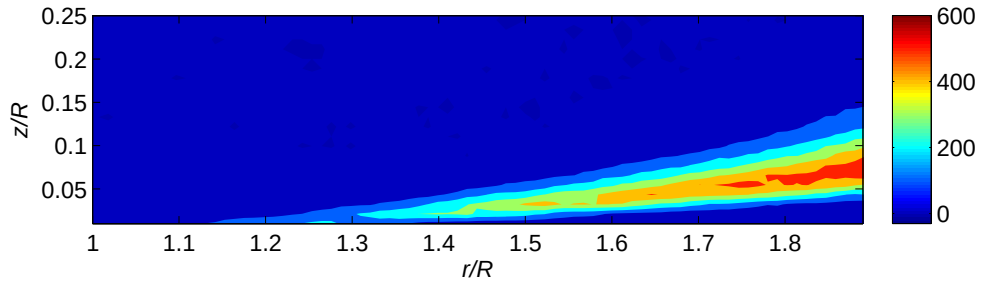

(a) Total number of particles moving in the r-direction.

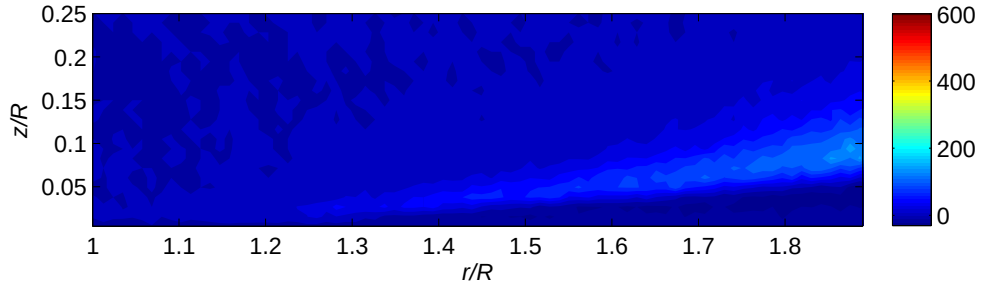

(b) Total number of particles moving in the z-direction.

Figure 3.41: The total particle flux in the r-direction and the z-direction for the one-bladed rotor.

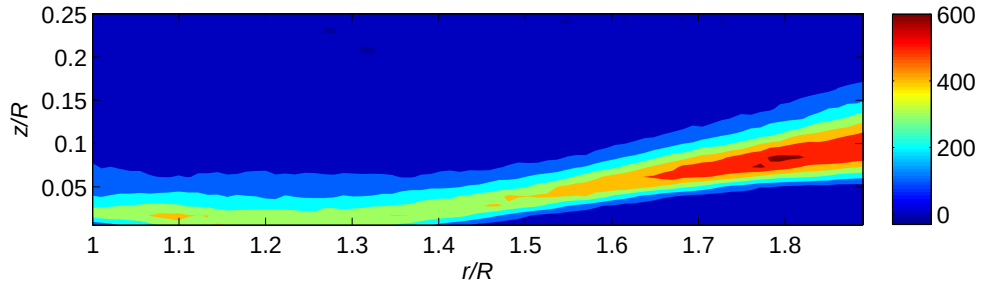

(a) Total number of particles moving in the r-direction.

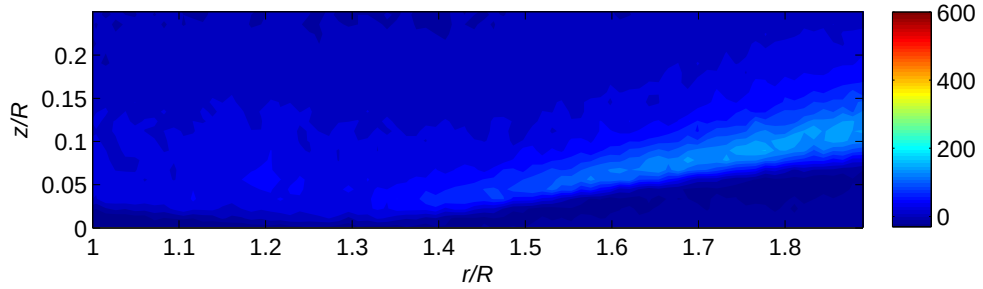

(b) Total number of particles moving in the z-direction.

Figure 3.42: The total particle flux in the r-direction and the z-direction for the two-bladed rotor.

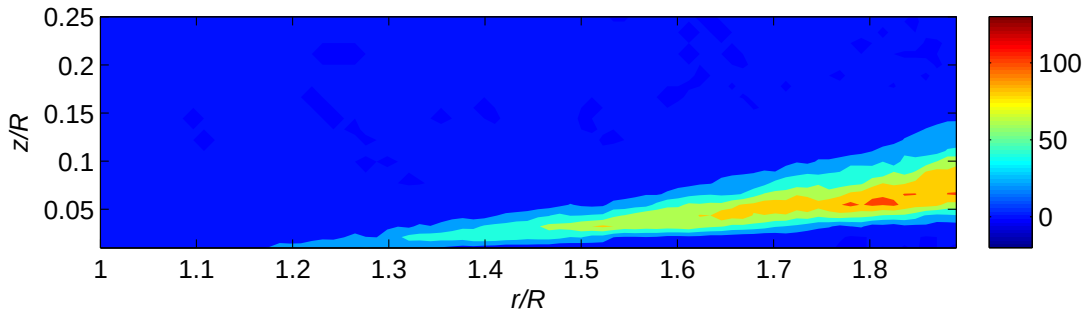

(a) Phase-averaged particle flux in the r-direction.

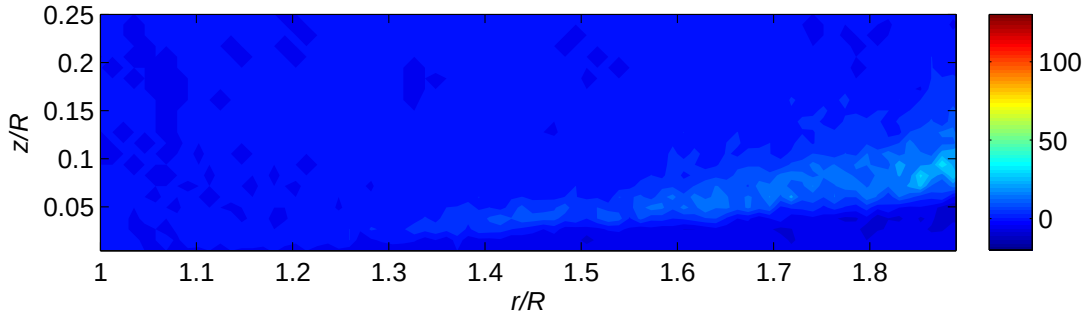

(b) Phase-averaged particle flux in the z-direction.

Figure 3.43: The phase-averaged particle flux for in the r-direction and the z-direction for the one-bladed rotor.

was determined which, if any, of the grid boundaries were crossed. Each time a particle was predicted to cross the left or right face of a particular cell, it was considered to contribute to the flux in the radial direction. Similarly, each particle that was determined to cross the top or bottom face of a cell was counted as a contribution to the wall-normal flux. Finally, an aggregate of particles convecting into and out of each cell was used to produce the contours shown in Figs. 3.41–3.44.

Figures 3.41 and 3.42 show the total time-averaged flux in each direction (outward and upward, respectively) as generated by both the one-bladed and two-bladed rotors at the defined operating conditions. The fluxes generated by the two-bladed rotor was approximately 15% greater in each direction as compared to those produced by the one-bladed rotor. Not only is there a greater number of particles being mobilized by the two-bladed rotor, a close examination of the flux con-

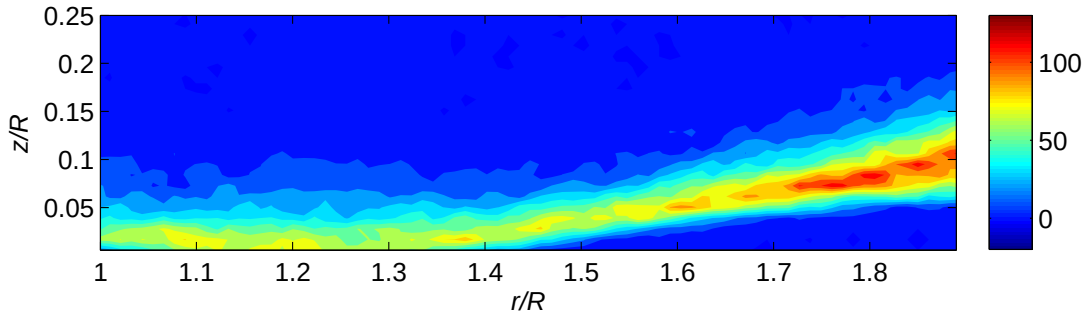

(a) Phase-averaged particle flux in the r-direction.

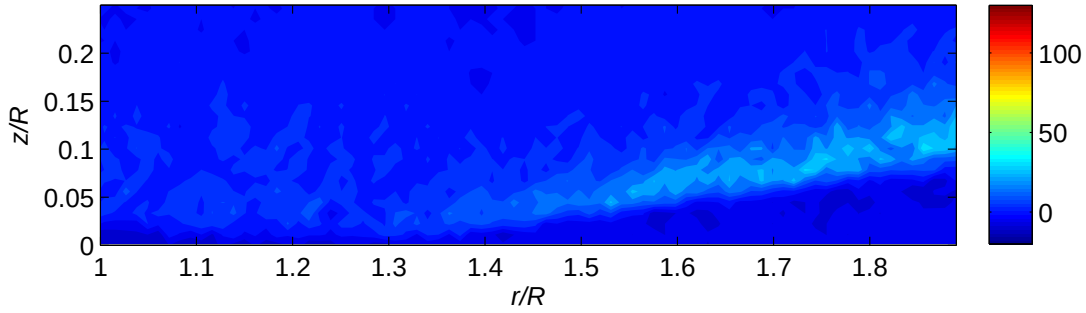

(b) Phase-averaged particle flux in the z-direction.

Figure 3.44: The phase-averaged particle flux for in the r-direction and the z-direction for the two-bladed rotor.

tours shows the two-bladed rotor is also convecting those mobilized particles to higher heights above the bed. Additionally, the radial (outward) flux of particles occurs much closer to the rotational axis of the two-bladed rotor, suggesting the mobilization of particles is initiated significantly earlier than for the one-bladed rotor.

Figures 3.43 and 3.44 shows the fluxes calculated only for images captured at approximately the same blade phase. Because this means only every fifth or sixth frame is considered, the approximately phase-locked results contain only one-fifth of the total particles. These same trends in the fluxes are also apparent in the phase-locked data. The two-bladed rotor again produces more particles upstream than the one-bladed rotor, and also generates a larger quantity of particles in aggregate. For each rotor it can be seen that there are clearly more particles that are being convected

radially as compared to vertically. However, there are certain areas in the flow where particles are moving in a wall-normal direction despite the flow direction in these regions being predominantly in the wall-parallel direction.

3.8.4 Influence of the Vortices on Particles

For this study, the instantaneous vortex locations were determined for 1,000 PIV image realizations using a multi-pass Q-criterion calculation [71], i.e.,

$$Q = \frac{1}{4}S^2 - q \tag{3.11}$$

where S is the trace of the 2-d velocity gradient tensor in the PIV measurements as given by

$$S = \frac{\partial u}{\partial x} + \frac{\partial v}{\partial y} \tag{3.12}$$

and q is the determinant of the velocity gradient tensor given by

$$q = \frac{\partial u}{\partial x}\frac{\partial v}{\partial y} - \frac{\partial u}{\partial y}\frac{\partial v}{\partial x} \tag{3.13}$$

The flow field (flow vectors) was divided into a Cartesian grid. For each rectangular cell, the value and location of the maximum Q-criterion was determined by evaluating the velocity gradients $\partial u/\partial x$, $\partial v/\partial y$, etc, from the PIV data. A second pass was used to filter the identified maximums, retaining only the Q-criterion results most likely to represent the actual locations of the vortices.

Cell maximums not exceeding the threshold for the minimum acceptable value of the Q-criterion were rejected as possible vortices. Additionally, cell maximums failing to satisfy the minimum spacing, i.e., located too closely to previously confirmed vortices, were not considered as possible candidates for identified vortices.

The maximum height of the uplifted sediment particles was evaluated by defining a rectangular region of influence below each vortex location; see Fig. 3.45(a). The ROI was again placed with the lower edge on the ground and sized to be 0.18 z/R in height with a length equal to 5% of the blade chord. However, if a vortex descended to a height of less than 0.18 z/R off the ground, then the height of its ROI was redefined to match the height of the vortex core. Pixel intensities were evaluated from the top of the ROI toward the bottom until a cluster of at least 6 connected pixels were found to have intensities that exceed the threshold for sediment particle identification.

The instantaneous heights of the identified vortices were then plotted against the maximum

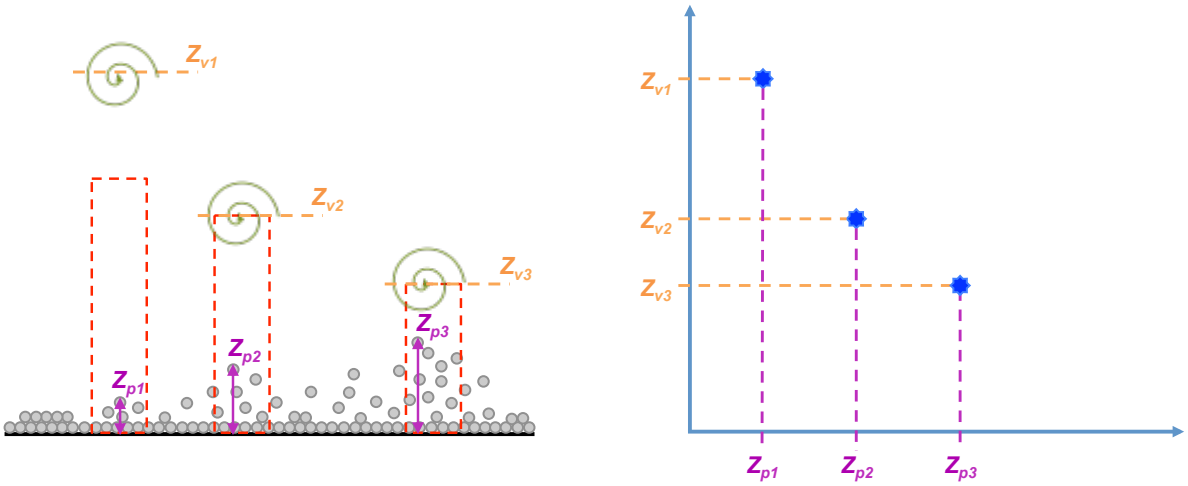

(a) Schematic defining vortex and particle heights.

(b) Example plot of vortex height versus particle height.

Figure 3.45: Method of comparing the proximity of vortices to the ground and the height of uplifted sediment particles beneath each vortex.

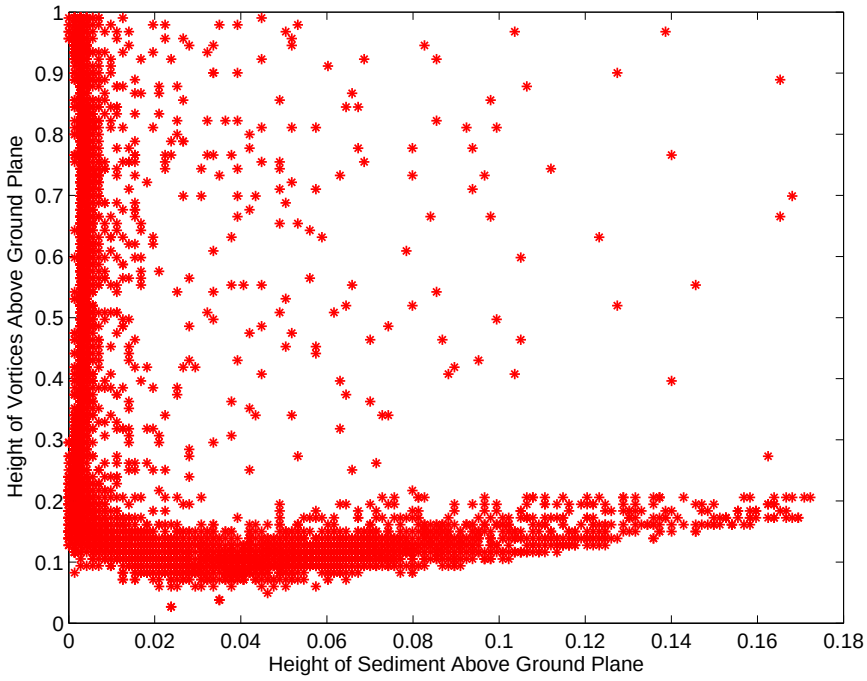

(a) One-bladed rotor.

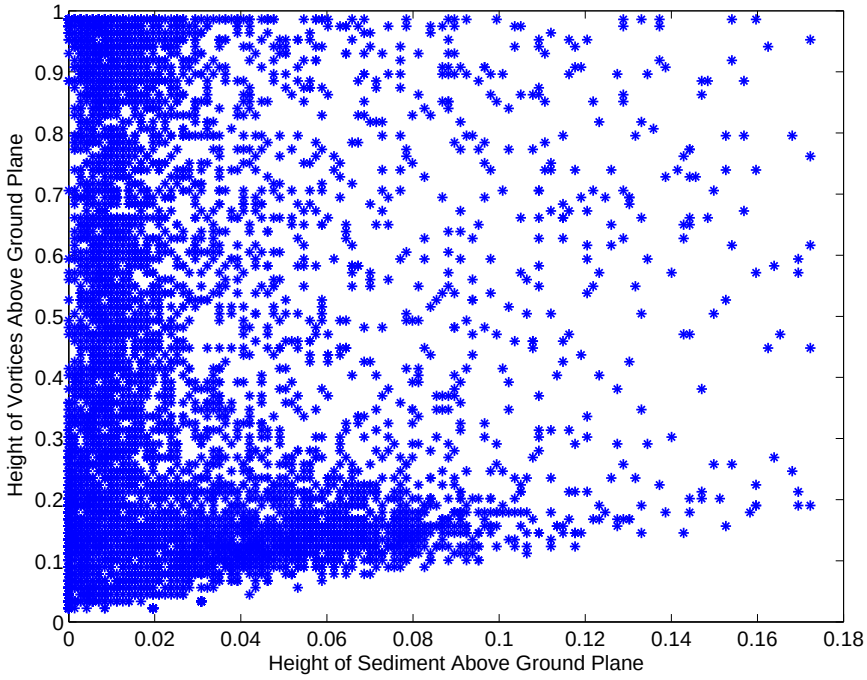

(b) Two-bladed rotor.

Figure 3.46: The relationship between the proximity of vortices to the ground and the height of uplifted sediment beneath each vortex.

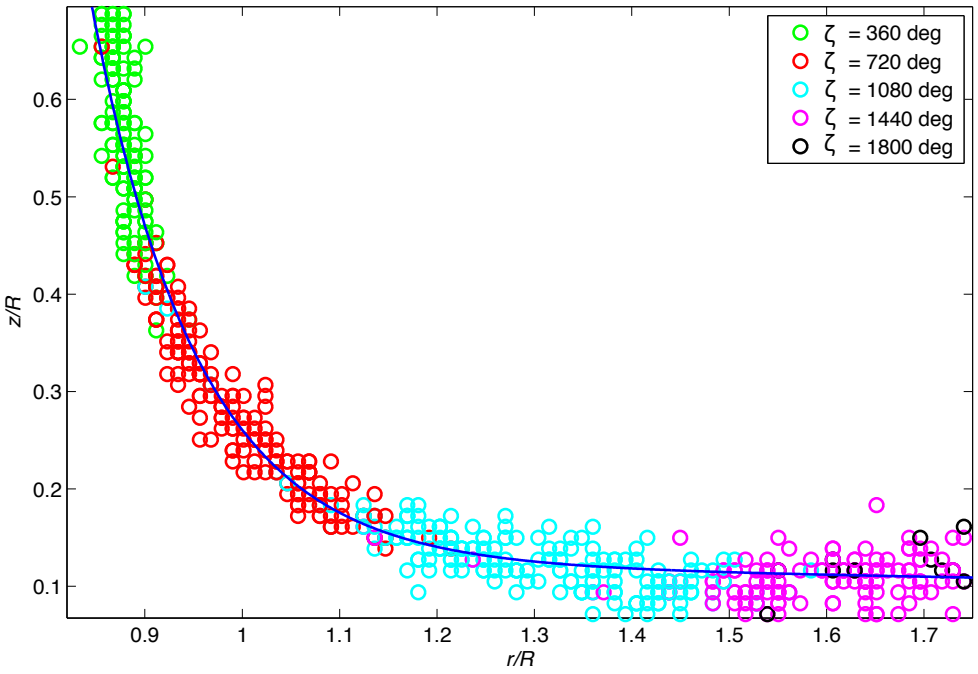

(a) One-bladed rotor.

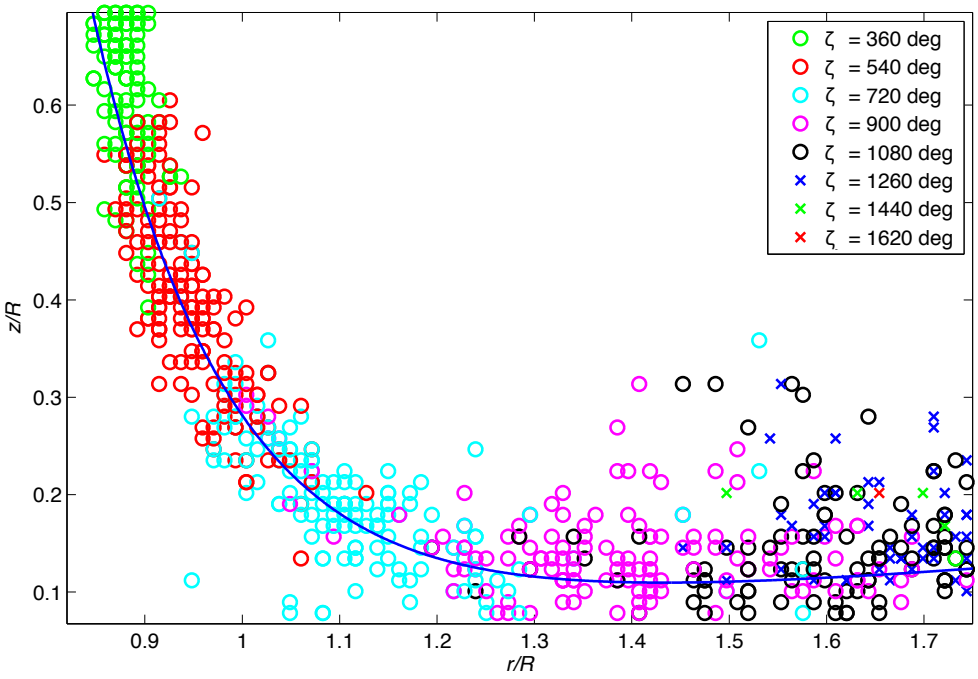

(b) Two-bladed rotor.

Figure 3.47: Instantaneous tip vortex locations grouped by wake age.

sediment particle heights found within their regions of influence, as shown in Fig. 3.45(b). It can be seen from Fig. 3.46 that there seems to exist a critical vortex height below which maximum height to which the sediment is uplifted increases abruptly and substantially. For the one-bladed rotor, this critical vortex height appears to be near 0.20 z/R; see Fig. 3.46(a). Identifying a vortex height below which uplift increases for the two-bladed rotor is more difficult because of the more dispersed particle concentrations, but the corresponding increase appears to occur at a vortex height of approximately 0.25 z/R; see Fig. 3.46(b).

The relative aperiodicity of the wakes is also apparent in Figs. 3.47(a) and 3.47(b). As previously mentioned, the wake of the two-bladed rotor contains more aperiodicity, which is because of the pairing, roll up, and merging of adjacent vortices, and which could also explain the more dispersed locations of the particles shown in Fig. 3.46(b). In contrast, the one-bladed rotor wake produces a tighter, more uniform band of vortex locations.

3.8.5 Particle/Flow Deviations

The results of both the PTV and PIV analysis were used to quantify the deviation of particle trajectory from the direction of the surrounding flow. For each particle location, the four nearest neighboring points for which flow velocity information was known were determined. The resolution of the PIV results was defined by the settings selected for the multipass data processing, such as final interrogation window size and the percentage of window overlap. The present PIV results contain velocity information at the intersection points of a 8×8 pixel grid, because an interrogation window size of 16×16 pixels and a 50% window overlap were used. The u-velocities

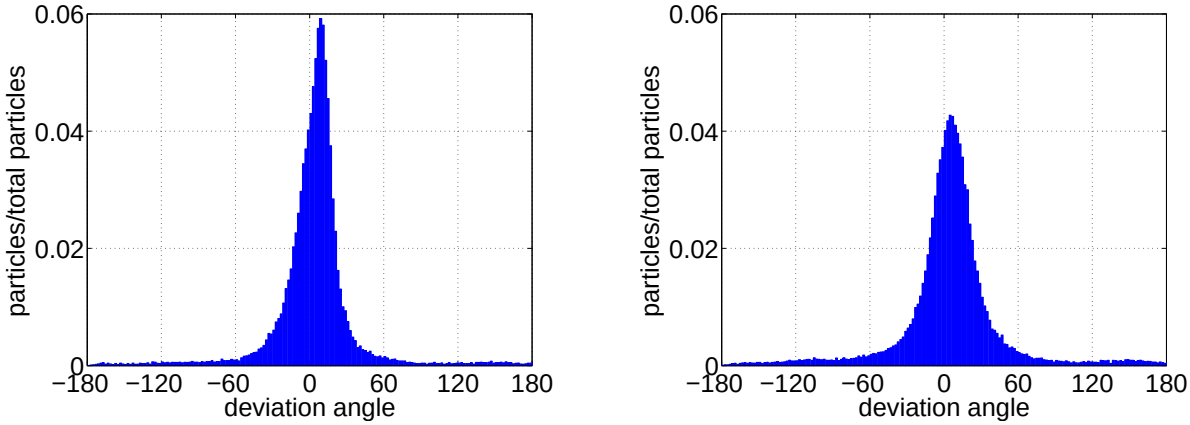

(a) One-bladed rotor.

(b) Two-bladed rotor.

Figure 3.48: Distribution of particles over the range of deviation angles for each rotor.

and v-velocities for both the particles and the carrier flow were used to calculate the angle of their respective trajectories.

The deviation angle was defined as the flow angle (i.e., the angle of a streamline) minus the particle trajectory angle (i.e., the angle made by the path of the particle), both with respect to the defined coordinate system. With this definition, negative deviation angles are possible and indicate the particle trajectory is considerably different to that of the flow. The distribution of particles for the entire range of deviation angles is shown in Fig. 3.48. Notice that most of the particle/flow deviation angles were calculated to be within the $\pm 60^\circ$ range for the flows generated by both rotors. The deviation distribution contains a tall, narrow peak for the one-bladed rotor with the bulk of the particle trajectories deviating very little from the direction of the flow. The two-bladed rotor produced a similar distribution, but its peak is lower and wider; c.f. Figs. 3.48(a) and 3.48(b).

Angles greater than -50° were considered to indicate significant particle/flow deviations. Figures 3.49 and 3.50 show examples of significant particle/flow deviations for the one-bladed rotor and the two-bladed rotor, respectively. For both rotors, there were clear instances where

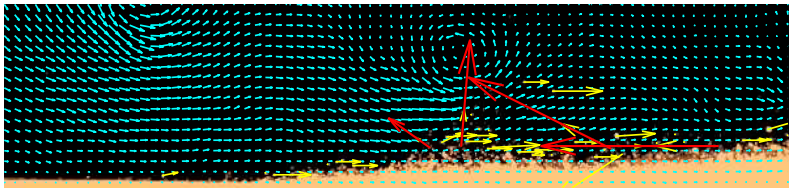

(a) $\zeta = 128°$

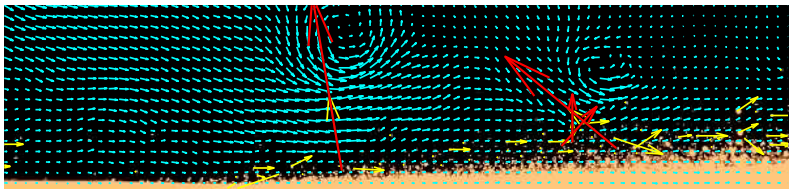

(b) $\zeta = 185°$

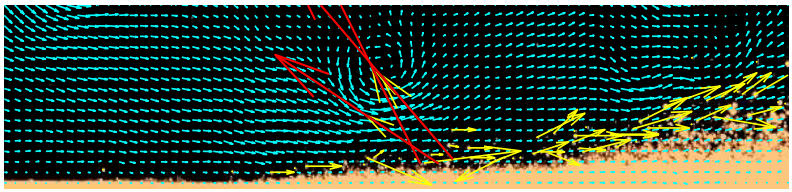

(c) $\zeta = 238°$

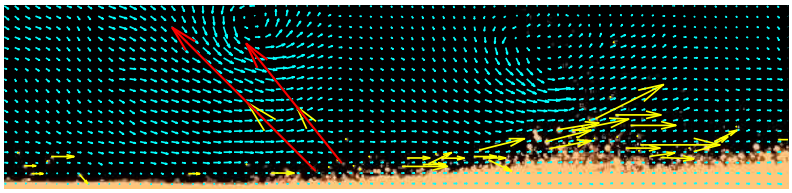

(d) $\zeta = 259°$

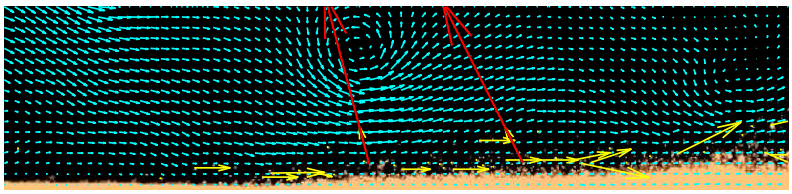

(e) $\zeta = 173°$

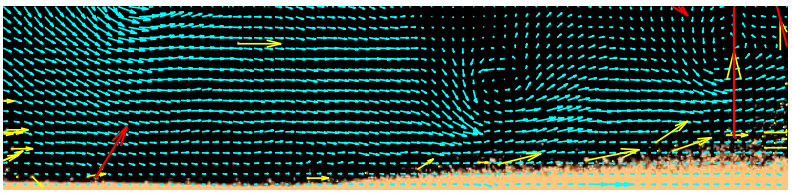

(f) $\zeta = 133°$

Figure 3.49: Examples of large particle/flow deviations for the one-bladed rotor.

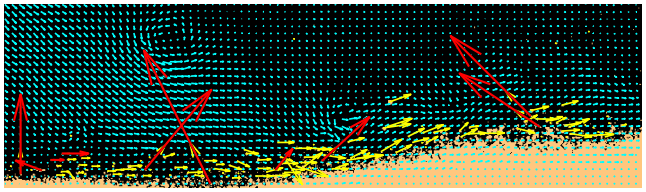

(a) $\zeta = 170^\circ$

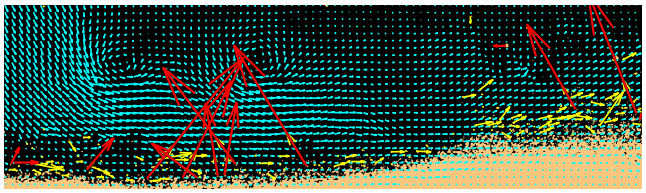

(b) $\zeta = 108^\circ$

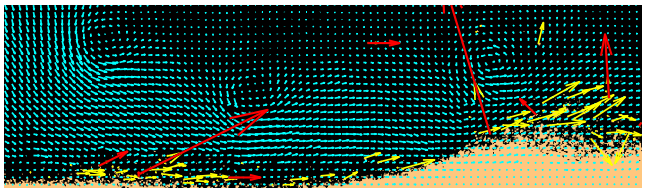

(c) $\zeta = 135^\circ$

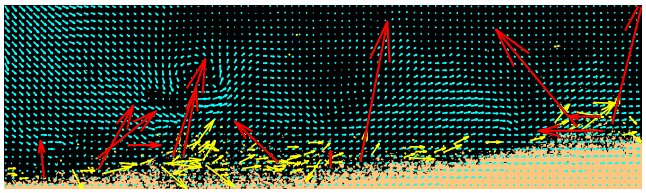

(d) $\zeta = 46^\circ$

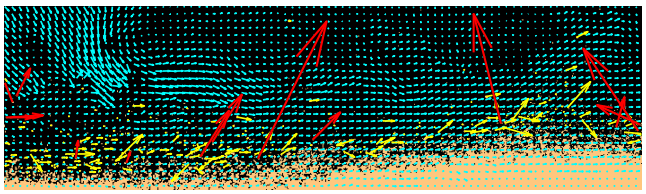

(e) $\zeta = 60^\circ$

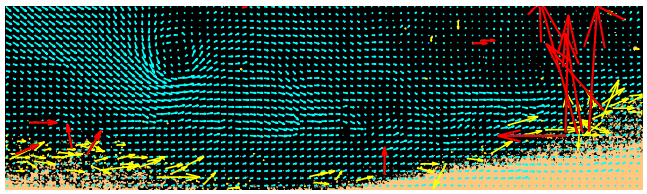

(f) $\zeta = 344^\circ$

Figure 3.50: Examples of large particle/flow deviations for the two-bladed rotor.

the uplifted particles were not following the course of the surrounding flow, but rather moving directly toward nearby vortices or to other regions of concentrated vorticity. This is an important observation because determining that particles can deviate significantly from the directions of the flow is not enough evidence alone to confirm causation. The spherical sediment particles have a time constant of 10 m sec, as calculated using [72]

$$\tau_p = \frac{\frac{4}{3}\pi {r_p}^3 \rho_p}{6\pi r_p \eta} \tag{3.14}$$

where η is the kinematic viscosity. Particles cannot be expected to instantly react to changes in velocity or to perfectly follow the non-uniform flow, and some deviations will be unavoidable. To determine the significance of these particle/flow deviations, the situation in which the deviation occurred must be examined for the presence of nearby vortices; see Fig. 3.50.

Before concluding that the particle deviations are evidence in support of vortex-induced pressure effects, all possible explanations of this behavior must be scrutinized. The various types of inter-particle forces cause the particles attract to each other, creating a cohesive effect that resists mobilization and uplift. Gravity acts as a restorative force, opposing the uplift of the particles and trying to pull the particles back down onto the bed. Inertial effects will also manifest as centrifugal forces, which would tend to cause the particles to move outward and away from the vortices.The fluid dynamic drag force retards particle motion, so the drag would pull the particles not in the direction of but rather away from the vortex that they are traveling toward. While Magnus forces created by particle spin could produce a lift force, these forces are unlikely to be high enough with spherical particles to produce these observed effects. Therefore, the measured deviations seen here

are more likely to be the consequences of body forces from the pressure gradients that are induced on the particle field when a vortex passes above the bed.

3.8.6 Scaling the Effects

While there are a variety of forces that can act on a particle, some of which cannot be easily measured, a simplified case can be considered. By neglecting all forces except the pressure lifting force and the gravitational force, the minimum differential pressure required to lift the weight of a particle can be determined. In the presence of all other forces, including inter-particle forces, dislodging a particle from the bed will likely take more than pressure forces alone. However, a simple calculation such as this can at least reveal if the measured pressures would indeed be enough to overcome the particle weight alone.

For this analysis, it was assumed that the top hemisphere of the particle was uniformly subjected to a lower than ambient (suction) pressure, while the bottom hemisphere experienced ambient pressure, as shown Fig. 3.51. In this case, the pressure force ($F_{\Delta P}$) becomes

$$F_{\Delta P} = (P_t - P_b) A_p \tag{3.15}$$

The weight of the particle, W_p, was calculated by assuming spherical particles of uniform density, i.e.,

$$W_p = \frac{4}{3} \pi {r_p}^3 \rho_p g \tag{3.16}$$

The minimum differential pressure required to lift a particle is the pressure difference that creates

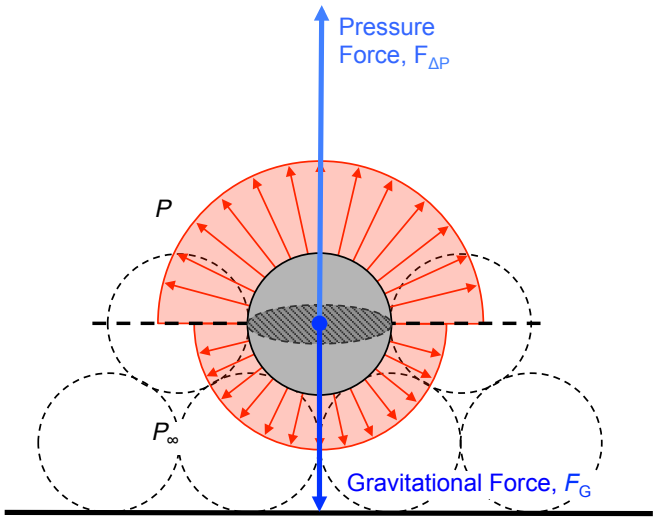

Figure 3.51: Schematic of a particle assuming constant pressure distributions over its top and bottom surfaces and considering only the effects of pressure and gravitation forces.

a lift force equal in magnitude to the weight of a particle. Therefore, using Eqs. 3.15 and 3.16, the value of ΔP_{min} was determined by using

$$\Delta P_{\text{min}} = \frac{\left(\frac{4}{3}\pi {r_p}^3 \rho_p\right) g}{A_p} = \frac{4\pi}{3A_p} {r_p}^3 \rho_p g \tag{3.17}$$

The potential flow model discussed in Section 3.6.3 was used to obtain the differential pressure induced on the ground with inputs for the small-scale one-bladed rotor, as well as inputs for a representative four-bladed full-scale helicopter; see Table 3.2. While the rotor dimensions and related parameters were scaled accordingly, the particles for both cases were considered to be those which were used in the experiments. Model inputs such as vortex height and vortex velocity were held to the same percentages of rotor radius and tip speed, respectively. The small-scale case resulted in a pressure force 34 times greater than the weight of a particle, and the full-scale case

	Small-Scale Rotor	Full-Scale Rotor
Particle Weight, W_p	8.35×10^{-10} N	8.35×10^{-10} N
Number of Blades, N_b	1	4
Rotor Radius, R	0.084 m	8.17 m
Tip Speed, V_{tip}	68.6 ms^{-1}	220.6 ms^{-1}
Vortex Height ($\%R$)	20	20
Vortex Velocity ($\%V_{\text{tip}}$)	5	5
Number of Vortices, N_v	3	3
Vortex Spacing ($\%R$)	31	156
Nondimensional Pressure Coefficient, $C_p{}'$	-0.50	-0.23
Differential Pressure, ΔP	-14.4 Pa	-69.2 Pa
Pressure Force, $F_{\Delta \text{P}}$	2.83×10^{-8} N	1.36×10^{-7} N
Pressure Force-to-Weight, $F_{\Delta \text{P}}/W_p$	34	163

Table 3.2: Table summarizing the inputs and results for the problem scaling analysis.

generated a pressure force-to-weight ($F_{\Delta \text{P}}/W_p$) of 163. With pressure forces that are potentially 2–3 orders of magnitude larger than the particle weight, not only could the pressure force overcome the weight of a particle and lift it from the bed, it seems reasonable that the effect of the pressure would also be sufficient to overcome the cohesive forces between the particles. These results suggest that pressure effects on the sediment particles could be very important in understanding and modeling the problem of brownout.

3.9 Summary

This chapter has described the results from the experiments that were conducted, including the behavior of the rotor wake as it developed in ground effect for a range of operating conditions. The measured unsteady pressure signatures on the ground plane were correlated to specific flow events occurring before, during, and after wake impingement on the ground plane. Flow visualization results were presented for both the single-phase and dual-phase flow experiments. An unsteady potential flow model was used as an explanatory aid to help interpret the pressure measurements. The methods by which this pressure data was synchronized with the flow data were discussed. Finally, the various types of analysis that was conducted on the measurements were explained, including the determination of particle concentrations, particle fluxes, and particle/flow deviation angles.

Chapter 4

Conclusions

4.1 Summary

The goal of the present research was to conduct experiments to better understand rotor-induced sediment particle mobilization from a underlying particle bed, and to search for evidence that rotor wake vortex-induced pressures on the bed affected particle uplift and motion. The idea was to explore the significance of any pressure effects on the particle motion as they might influence the more general problem of rotorcraft brownout. Both one-bladed and two-bladed laboratory-scale rotors were used, the rotors being operated at three rotor heights above the ground plane and at two rotational frequencies. The experiments involved time-resolved flow visualization and particle image velocimetry (PIV) measurements of the rotor wake, which were correlated to time-histories of the unsteady pressure field measured over a ground plane. Distinctive pressure signatures were identified that corresponded to three regimes on the ground plane as they were affected by the vortices in the rotor wake. Particle tracking velocimetry (PTV) was used to measure the motion of the sediment particles, and measurements of the particle displacements and their local concentrations were related to the location of the vortices and the corresponding unsteady pressures that were produced over the ground plane.

4.2 Specific Conclusions

The following conclusions have been drawn from the research:

1. Three characteristic pressure signatures on the ground plane were identified that corresponded to the sequence of the rotor wake vortices impinging on the ground. The first, called pre-impingement, exhibited a pressure responses with rounded peaks that occurred in phase with the rotor blade passage. The second was called peri-impingement because it included the actual impingement of the rotor wake and the radially expanding flow over the ground that followed, within which vortex cores could be seen to convect fairly steadily above the ground plane. These events created a low pressure signature whose shape could be described as a series of oblique, uneven troughs. Finally, the third region, which included any points beyond which the vortices had diffused and could no longer be observed, has been referred to as post-impingement. The measured pressure responses corresponding to this latter region of the flow contained some fluctuations, but they were more random and of much smaller magnitude compared to the other regimes.

2. The rotor operating conditions were found to influence the location of the rotor wake impingement upon the ground plane and the extent to which vortices persisted in the flow before diffusing their vorticity. As the height of the rotor plane above the ground was increased, the location of wake impingement on the ground plane moved radially outboard away from the rotor. Similarly, an increase in the rotational frequency of the rotor also resulted in a shift of the impingement zone on the ground to points that were farther away from the rotor. Both a decrease the rotor height above the ground or an increase in the rotational frequency of the

rotor were observed to cause the blade tip vortices to persist to later (older) wake ages before diffusing their vorticity.

3. The magnitude of the pressure responses on the ground were found to be dependent on parameters such as the height of the vortex above the ground, the speed at which a vortex was convecting near the ground, and the strength (circulation) of the vortex. For a passing vortex to induce a significant low pressure (suction) pressure on the ground, it was shown that it must be relatively close to the ground, moving relatively slowly, or have sufficiently high strength. The nearer to the ground, the slower the convection and the stronger a vortex is, the greater was the magnitude of the resulting pressure fluctuation at the ground plane.

4. From experimental observations and from predictions using an unsteady potential flow model for convecting vortices, it was determined that the spacing between the vortices and/or the frequency at which vortices convected parallel to the ground (which is related to the number of blades) can affect the magnitude and the shape of the unsteady pressure responses. The one-bladed rotor produced a distinct peak or valley in the pressure response with the passing of each individual vortex. The signatures induced by adjacent vortices that were trailed from the two-bladed rotor, however, were seen to blend together and also increase the amplitude of the unsteady pressure fluctuations.

5. It was noticed that sediment particles were uplifted in the absence of strong upwash velocities. At certain areas in the flow, particles were observed to be moving in a wall-normal direction despite the flow direction in these regions being predominantly in the wall-parallel direction. This behavior was seen in the presence of vortices as concentrations of particles

that amassed and convected toward the center of passing vortices. Particles were also observed convecting along directly below vortices, as opposed to being trapped just ahead of them in the vortex upwash region. Instantaneous correlations between the sediment height and the wall-normal velocity also showed that some of the highest instances of sediment uplift correspond to near-zero or negative wall-normal velocities.

6. As the rotor wake vortices approached the ground, there appeared to exist a critical vortex height above the ground at which the height of the uplifted sediment abruptly increased. This height was dependent on the rotor operating conditions. The vortices have a finite range of influence in the flow, so while they are relatively high above the ground plane they do not substantially affect the mobilization of sediment particles. However, once a vortex comes into closer proximity of the sediment bed, there was a rapid increase in the maximum height of the uplifted particles. In the present work, this critical vortex height was found to be in the range of 0.20–0.25 rotor radii off the ground.

7. There was evidence that the steep velocity and pressure gradients in the vicinity of the convecting vortices created a low pressure region above the sediment bed, which increased the propensity of particles to be entrained by the flow and also altered the trajectories of any mobilized particles. Examples of significant particle-flow deviations (i.e., angles $\geq 50^{\circ}$) were shown to occur near passing vortices. In these instances, uplifted particles were found to be traveling more toward the centers of the vortices rather than following the local flow velocities in that region. Considering all the contributions of the various forces acting on the particles, it seems likely that this behavior is the consequence of a body force created by the

vortex-induced pressures in the flow, i.e., a form of pressure lift force on the particles similar to a Saffman force.

8. Based on the evidence shown, it may be that pressure lift force effects of sediment particles will need to be included in brownout simulations. It has been shown in this work that the pressures induced on the ground plane by blade tip vortices are likely to be of sufficient magnitude in the flow to alter the particle trajectories away from the primary flow directions. For particles on the sediment bed, the lower pressures induced by the presence of the vortices could manifest as an effective reduction in the magnitude of inter-particle forces. This means that particles would then be more easily entrained via other sediment transport mechanisms, such as shear. The computational modeling of these effects may be necessary to accurately predict brownout conditions.

4.3 Suggestions for Future Work

The specific objectives of the present work were to investigate the relationship between the vortex-induced unsteady pressure field on the ground and its possible effects on the mobilization and uplift of the sediment there, while seeking to verify also the existence of a pressure lift force on uplifted particles. While the present work is by no means complete, it has provided new insight into the interaction of the vortical flow of the rotor wake with mobile sediment particles lying on the ground below a rotor, which drives the serious problem of rotorcraft brownout. But there are obviously still many issues that could be addressed in the future to better understand the effect of pressure effects in the flow on sediment mobilization and transport.

In the present work, pressure measurements on the ground plane were obtained separately from the flow experiments. Future experiments could be designed to measure simultaneously the flow and the pressures. The use of a trigger could be used to synchronize the initiation of sampling by both data acquisition systems. This arrangement would remove any uncertainties associated with the data synchronization that must otherwise be corrected for during the post-processing of the acquired data. However, dual-phase experiments may still not be feasible because the sediment particles are generally small enough that they could fall into the pressure sensor ports.

As discussed in the Introduction to this thesis, air flowing through a permeable sediment bed may affect affect the growth and detachment of the boundary layer and, thus, the quantity of particles that are mobilized or displaced. This situation could be simulated by forcing air down or up through a perforated ground plane covered with a sediment bed. A series of experiments in which the velocity of the permeating jets is varied while the flow field conditions are held constant could reveal the effect of bed permeability on the thresholds for sediment mobility.

The various mechanisms for sediment mobilization and transport are coupled in the complex, vortical rotor-induced flow field, which makes it difficult to attribute the observations to a single mechanism. To evaluate the individual contribution of the pressure mechanism to sediment mobilization, the experiment would have to be simplified to reduce or eliminate other known mechanisms. Varying the ambient pressure over the bed while subjecting it to more controlled wall-parallel flow could help isolate this effect. The experimental apparatus in this case may include a suitably designed plenum, which could be brought progressively into proximity of the flow that develops across the particle bed.

For better insight into the pressure field induced by passing vortices, the pressure should be measured in the flow itself rather than just along the ground plane. For a rotor flow, this goal would require the measurement of the out-of-plane velocity in addition to the in-plane velocities, and then the use of other assumptions and techniques to solve for the pressure field from the velocity measurements. To resolve all three components of the velocities, a stereoscopic PIV system would be necessary. The benefits of such an experiment would be the acquisition of simultaneous time-histories of flow velocity and pressure, which would help in further understanding the source of pressure effects on the particle phase.

A desirable measurement would be the pressure distribution over the surface of the particle itself. However, obtaining such a measurement poses many challenges. Perhaps in the future, a micro-spherical pressure transducer could be developed that is similar in weight to typical sediment particle. In the absence of this technology, steps could be taken to make inferences about which forces are influencing the particles based on other observations. For example, marking the sediment particles with an indicator, such as a ring of reflective paint, would reveal any particle spin and help to evaluate whether the uplift of a particle is more a consequence of Magnus forces or otherwise. However, even if such particles could be developed, this type of measurement would require very high camera resolutions and high imaging frame rates.

Appendix A: The Unsteady Flow Model

A.1 Derivation of Unsteady Flow Model

The analytical model developed to study the pressure distribution on the ground induced by a train of vortices was based on potential flow theory. Under the assumptions of inviscid and irrotational flow, the velocity field, $\mathbf{V}$, can be described as a gradient of a scalar velocity potential field, ϕ, and is given by

$$\mathbf{V} = \nabla\phi \tag{A.1}$$

If the flow is also assumed to be incompressible, the velocity potential satisfies Laplace's equation, and potential flow theory is applicable, as shown in Eq. A.2

$$\nabla^2\phi = 0 \tag{A.2}$$

Since the velocity potential satisfies Laplace equation, the principle of linear superposition is applicable and as a result, the net potential field is a superposition of the individual potential flow elements. The potential flow elements used to model the rotor flow near the ground is shown in Fig. A.1. The train of vortices are comprised of vortices of strength Γ each, convection at a height Z_v above the ground with a vortex convection velocity V_s. The system of vortices are superimposed with a uniform wall-parallel freestream of velocity V_∞. An image system is used to represent the ground by enforcing flow tangency at the ground plane.

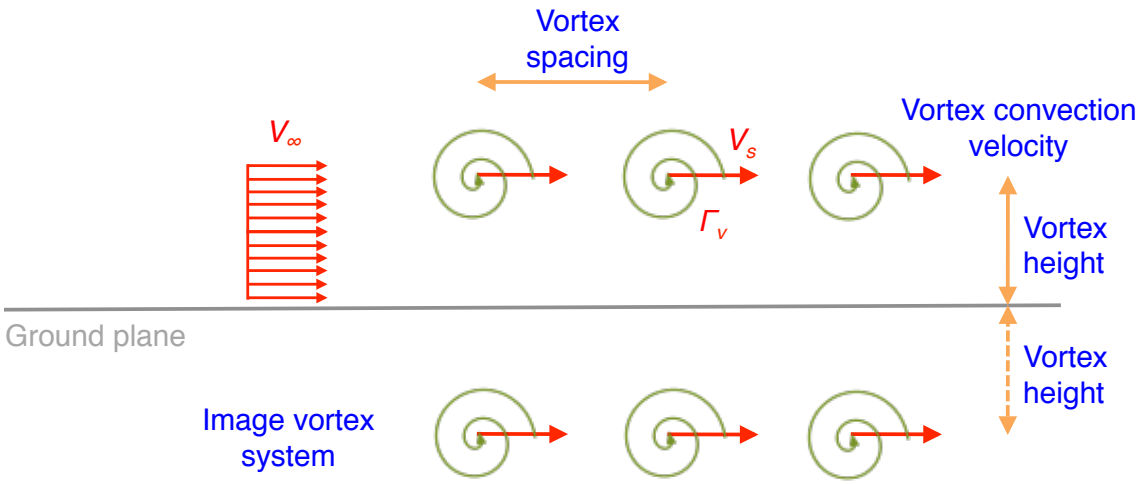

Figure A.1: Schematic depicting the potential flow model based on a train of vortices.

A.1.1 Potential Field – Uniform Velocity

The wall-parallel freestream velocity and the associated velocity potential in the cartesian system is given by

$$\begin{aligned} \mathbf{V} &= V_\infty \hat{\mathrm{i}} \\ \phi(x,y) &= V_\infty x \end{aligned} \tag{A.3}$$

where x is the distance along the x-coordinate from the reference coordinate axis.

A.1.2 Potential Field – Vortex

Figure A.2 shows a representative potential vortex of strength Γ located at coordinates (x_v, y_v). The induced velocity of the vortex at location (x,y) is given by

$$\begin{aligned} \mathbf{V}_x &= -\frac{\Gamma(y-y_v)}{2\pi r^2}\hat{\mathrm{i}} \\ \mathbf{V}_y &= \frac{\Gamma(x-x_v)}{2\pi r^2}\hat{\mathrm{j}} \end{aligned} \tag{A.4}$$

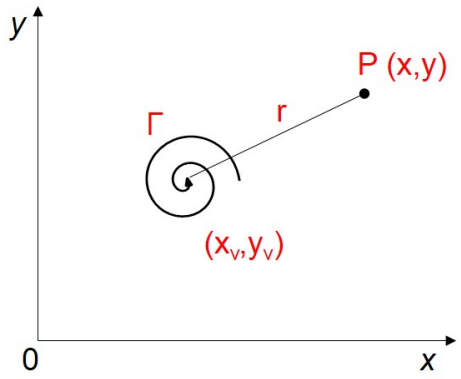

Figure A.2: Schematic depicting a vortex along with the reference coordinate system.

where $r^2 = (x - x_v)^2 + (y - y_v)^2$. The velocity potential for the vortex can be computed using Eq. A.1, and the resulting potential is given by

$$\phi(x,y) = \frac{\Gamma}{2\pi}\left[\tan^{-1}\left(\frac{y-y_v}{x-x_v}\right) - \tan^{-1}\left(\frac{x-x_v}{y-y_v}\right)\right] \tag{A.5}$$

The time-varying change of velocity potential can be evaluated by differentiating Eq. A.5 with respect to time, t. Assuming that vortices convect only in the wall-parallel direction, i.e., $\dot{y_v} = 0$, we obtain

$$\frac{\partial\phi(x,y)}{\partial t} = \frac{\Gamma\dot{x_v}(y-y_v)}{\pi[(x-x_v)^2 + (y-y_v)^2]} \tag{A.6}$$

where $\dot{x_v}$ is the vortex convection velocity in the wall-parallel direction. The combined potential of a vortex pair (real and image system) is obtained by noting that $\Gamma_{image} = -\Gamma_{real}$, and $y_{v_{\text{image}}} = -y_{v_{\text{real}}}$, is given by

$$\begin{aligned}\phi(x,y) &= \frac{\Gamma}{2\pi}\left[\tan^{-1}\left(\frac{y-y_v}{x-x_v}\right) - \tan^{-1}\left(\frac{x-x_v}{y-y_v}\right)\right] \\ &- \frac{\Gamma}{2\pi}\left[\tan^{-1}\left(\frac{y+y_v}{x-x_v}\right) - \tan^{-1}\left(\frac{x-x_v}{y+y_v}\right)\right]\end{aligned} \tag{A.7}$$

A.1.3 Net Velocity and Potential Field

Since the principle of linear superposition is applicable for the potential fields, the net velocity potential is the linear sum of the velocity potential for the real vortices, image vortices, and the freestream velocity. The net velocity field is given by the vector addition of the velocities of the contributing potential flow elements. From Eqs. A.3 and A.5, the net velocity and velocity potential at point (x,y) induced by the uniform freestream and the train of vortices is given by

$$\begin{aligned}
\mathbf{V} &= V_\infty \hat{\mathrm{i}} \\
&+ \sum_{i=1}^{N} \left[-\frac{\Gamma(y-y_v)}{2\pi r_{\text{real}}^2} \hat{\mathrm{i}} + \frac{\Gamma(\mathrm{x}-\mathrm{x_v})}{2\pi \mathrm{r}_{\text{real}}^2} \hat{\mathrm{j}} \right] \\
&- \sum_{i=1}^{N} \left[-\frac{\Gamma(y+y_v)}{2\pi r_{\text{image}}^2} \hat{\mathrm{i}} + \frac{\Gamma(\mathrm{x}-\mathrm{x_v})}{2\pi \mathrm{r}_{\text{image}}^2} \hat{\mathrm{j}} \right]
\end{aligned} \tag{A.8}$$

$$\begin{aligned}
\phi(x,y) &= V_\infty x \\
&+ \sum_{i=1}^{N} \frac{\Gamma_i}{2\pi} \left[\tan^{-1}\left(\frac{y-y_{v_i}}{x-x_{v_i}}\right) - \tan^{-1}\left(\frac{x-x_{v_i}}{y-y_{v_i}}\right) \right] \\
&- \sum_{i=1}^{N} \frac{\Gamma_i}{2\pi} \left[\tan^{-1}\left(\frac{y+y_{v_i}}{x-x_{v_i}}\right) - \tan^{-1}\left(\frac{x-x_{v_i}}{y+y_{v_i}}\right) \right]
\end{aligned} \tag{A.9}$$

where N is the total number of real vortices, $(x_v,y_v)_i$ is the location of the i^{th} vortex, $r_{\text{real}}^2 = (x-x_v)^2+(y-y_v)^2$, and $r_{\text{image}}^2 = (x-x_v)^2+(y+y_v)^2$. The time varying potential at a point (x,y) is given by

$$\begin{aligned}
\frac{\partial \phi(x,y)}{\partial t} &= \frac{\Gamma \dot{x_v}(y-y_v)}{\pi[(x-x_v)^2+(y-y_v)^2]} \\
&- \frac{\Gamma \dot{x_v}(y+y_v)}{\pi[(x-x_v)^2+(y+y_v)^2]}
\end{aligned} \tag{A.10}$$

A.1.4 Evaluation of Ground Pressure

The pressure on the ground can be evaluted through the unsteady Bernoulli equation (i.e., Kelvin equation), given by

$$p_\infty + \frac{1}{2}\rho \mathbf{V}_\infty^2 = p + \frac{1}{2}\rho \mathbf{V}^2 + \rho \frac{\partial \phi}{\partial t} \tag{A.11}$$

where ρ is the density of air. At a point on the ground, whose coordinates are $(x,0)$, Eqs. A.8 and A.10 are reduced to

$$\begin{aligned} \mathbf{V}(x,0) &= V_\infty \hat{\imath} + \sum_{i=1}^{N} \frac{\Gamma\, y_{v_i}}{2\pi[(x-x_{v_i})^2 + (y_{v_i})^2]}\, \hat{\imath} \\ \frac{\partial \phi(x,0)}{\partial t} &= \sum_{i=1}^{N} \frac{-2\Gamma\, \dot{x_{v_i}}\, y_{v_i}}{\pi[(x-x_{v_i})^2 + (y_{v_i})^2]} \end{aligned} \tag{A.12}$$

Using Eqs. A.11 and A.12 in conjunction, the pressure at any point on the ground arising from the passage of a train of vortices can be computed.

References

[1] Mapes, P., Kent, R., and Wood, R., "DoD Helicopter Mishaps FY85-05: Findings and Recommendations," U.S. Air Force, 2008.

[2] National Transportation Safety Board, "NTSB Accident Briefs: LAX01LA283, LAX01LA304, LAX04LA285, SEA05CA173,".

[3] Jansen, C., Wennemers, A., and Groen, E., "FlyTact: A Tactile Display Improves a Helicopter Pilots Landing Performance in Degraded Visual Environments," *Haptics: Perception, Devices and Scenarios*, Vol. 502, No. 4, 2008, pp. 867–875.

[4] Sandblaster 1: Support of See-Through Technologies for Particulate Brownout, "Task 1 Technical Report, MRI Project No. 110565," Sponsored by the Defense Advanced Research Projects Agency (DOD) Strategic Technology Office, Issued by U.S. Army Aviation and Missile Command under Contract No. W31P4Q-07-C-0215, October 31, 2007.

[5] Sandblaster 2: Support of See-Through Technologies for Particulate Brownout, "Task 5 Technical Report, MRI Project No. 110565," Sponsored by the Defense Advanced Research Projects Agency (DOD) Strategic Technology Office, Issued by U.S. Army Aviation and Missile Command under Contract No. W31P4Q-07-C-0215, October 31, 2007.

[6] Pickford, M., "Operating Helicopters Safely in a Degraded Visual Environment in Support of Military Operations," Proceedings of the Royal Aeronautical Society Rotorcraft Group

Conference, Operating Helicopters Safely in a Degraded Visual Environment, London, UK, June 16 & 17, 2010.

[7] Milluzzo, J., Sydney, A., Rauleder, J., and Leishman, J. G., "In-Ground-Effect Aerodynamics of Rotors with Different Blade Tips," 66th Annual Forum Proceedings of the American Helicopter Society, Phoenix, AZ, May 10–13, 2010.

[8] Sydney, A., Baharani, A., and Leishman, J. G., "Understanding Brownout Using Near-Wall Dual-Phase Flow Measurements," 67th Annual Forum Proceedings of the American Helicopter Society, Virginia Beach, VA, May 3–5, 2011.

[9] Cheeseman, I. C., and Bennett, W. E., "The Effect of the Ground on a Helicopter Rotor in Forward Flight," ARC R&M 3021, 1955.

[10] Fradenburgh, E. A., "The Helicopter and the Ground Effect Machine," *Journal of the American Helicopter Society*, Vol. 5, No. 4, 1960, pp. 26–28.

[11] Knight, M., and Hefner, R. A., "Analysis of Ground Effect on the Lifting Airscrew," NACA TN 835, 1941.

[12] Hayden, J.S., "The Effect of the Ground on Helicopter Hovering Power Required," American Helicopter Society 32th Annual National V/STOL Forum Proceedings, Washington D.C., May 10–12, 1976.

[13] Curtiss, H. C., Sun, M., Putman, W. F., and Hanker, E. J., "Rotor Aerodynamics in Ground Effect at Low Advance Ratios," *Journal of the American Helicopter Society*, Vol. 29, No. 1, 1984, pp. 48–55.

[14] Light, J. S., and Norman, T., "Tip Vortex Geometry of a Hovering Helicopter Rotor in Ground Effect," American Helicopter Society 45th Annual Forum Proceedings, Boston, MA, May 22–24, 1989.

[15] Prouty, R. W., "Ground Effect and the Helicopter," AIAA Paper 85-4034, AIAA/AHS/ASEE Aircraft Design Systems and Operations Meeting, Colorado Springs, CO, October 14–16, 1985.

[16] Lee, T. E., Leishman, J. G., and Ramasamy, M., "Fluid Dynamics of Interacting Blade Tip Vortices with a Ground Plane," *Journal of the American Helicopter Society*, Vol. 55, No. 2, April 2010, pp. 1–16.

[17] Johnson, B., Leishman, J. G., and Sydney, A., "Investigation of Sediment Entrainment Using Dual-Phase, High-Speed Particle Image Velocimetry," *Journal of the American Helicopter Society*, Vol. 55, No. 4, 2010, p. 42003.

[18] Nathan, N. D., and Green, R. B., "Measurements of a Rotor Flow in Ground Effect and Visualization of the Brownout Phenomenon," 64th Annual Forum Proceedings of the American Helicopter Society, Montreal, Canada, April 29–May 1, 2008.

[19] Phillips, C., and Brown, R.E., "Eulerian Simulation of the Fluid Dynamics of Helicopter Brownout," *AIAA Journal of Aircraft*, Vol. 46, No. 4, July 2009, pp. 1416–1429.

[20] Kok, J. F., Parteli, E. J. R., Michaels, T. I., and Bou, Karam D., "The Physics of Wind-Blown Sand and Dust," *Reports on Progress in Physics*, Vol. 75, No. 10, 2012, p. 106901.

[21] Saffman, P. G., "Lift on a Small Sphere in a Slow Shear Flow," *Journal of Fluid Mechanics*, Vol. 22, No. 385, 1965.

[22] Zou, X-Y., Cheng, H., Zhang, C-L., and Zhao, Y-Z. "Effects of the Magnus and Saffman Forces on the Saltation Trajectories of Sand Grain," *Geomorphology*, Vol. 90, 2007, pp. 11–22.

[23] Doligalski, T. L., Smith, C. R., and Walker, J. D. A., "Vortex Interactions with Walls," *Annual Review of Fluid Mechanics*, Vol. 26, 1994, pp. 573–616.

[24] Walker, J. D. A., Smith, C. R., Cerra, A. W., and Doligalski, T. L., "The Impact of a Vortex Ring on a Wall," *Journal of Fluid Mechanics*, Vol. 181, 1987, pp. 99–140.

[25] Bethke, and N., Dalziel, S. B., "Resuspension Onset and Crater Erosion by a Vortex Ring Interacting with a Particle Layer," *Physics of Fluids*, Vol. 24, No. 063301, 2012.

[26] Jaraiz, E., Kimura, S., and Levenspiel, O., "Vibrating Beds of Fine Particles: Estimation of Interparticle Forces from Expansion and Pressure Drop Experiments," *Powder Technology*, Vol. 72, No. 1, 1992, pp. 23–30.

[27] Bagnold, R. A., *The Physics of Blown Sand and Desert Dunes,* Dover Publications, Inc., Mineola, NY, 1941.

[28] Greeley, R., and J. D. Iversen, *Wind as a Geological Process on Earth, Mars, Venus and Titan,* Cambridge University Press, New York, NY, 1985.

[29] Shao Y., and Lu, H., "A Simple Expression for Wind Erosion Threshold Friction Velocity," *Journal of Geophysical Research*, Vol. 105, No. D17, 2000, pp. 22,437–22,443.

[30] Marticorena, B., and Bergametti, G., "Modeling the Atmospheric Dust Cycle: 1. Design of a Soil-Derived Dust Emission Scheme," *Journal of Geophysical Research*, Vol. 100, No. D8, August 1995, pp. 16,415–16,430.

[31] Lu, H., and Shao, Y., "A New Model for Dust Emission by Saltation Bombardment," *Journal of Geophysical Research*, Vol. 104, No. D14, July 1999, pp. 16,827–16,842.

[32] Shao, Y., "A Model for Mineral Dust Emission," *Journal of Geophysical Research*, Vol. 106, No. D17, September 2001, pp. 20,239–20,254.

[33] Sutherland, A. J., "Proposed Mechanism for Sediment Entrainment by Turbulent Flows," *Journal of Geophysical Research*, Vol. 72, No. 24, December 1967, pp. 6,183–6,194.

[34] Greeley, R., "Saltation Impact as a Means for Raising Dust on Mars," *Planetary and Space Sciences*, Vol. 50, No. 2, February 2002, pp. 151–155.

[35] Greeley, R., Balme, M. R., Iversen J. D., Metzger, S., Mickelson, R., Phoreman, J., and White, B., "Martian Dust Devils: Laboratory Simulations of Particle Threshold," *Journal of Geophysical Research*, Vol. 108, No. E5, 2003, pp. 7-1 to 7-12.

[36] Balme, M. R., Stephen, M., Towner, M., Ringrose, T., Greeley, R., and Iversen, J., "Dust Devils on Earth and Mars," *Geophysical Research Letters*, Vol. 30, No. 16, August 2003, pp. 1–4.

[37] Balme, M. R., and Greeley, R., "Dust Devils on Earth and Mars," *Reviews of Geophysics*, Vol. 44, No. RG3003, September 2006, pp. 1–22.

[38] Shao, Y., Raupach, M. R., and Findlater, P. A., "Effect of Saltation Bombardment on the Entrainment of Dust by the Wind," *Journal of Geophysical Research*, Vol. 98, No. D7, February 1993, pp. 12,719–12,726.

[39] Ryerson, C. C., Haehnel, R. B., Koenig, G. G., and Moulton, M. A., "Visibility Enhancement in Rotorwash Clouds," Paper AIAA-2005-263, 43rd AIAA Aerospace Sciences Meeting and Exhibit, Reno, NV, January 10–13, 2005.

[40] Haehnel, R. B., Moulton, M. A., Wenren, W., and Steinhoff, J., "A Model to Simulate Rotorcraft-Induced Brownout," 64th Annual Forum Proceedings of the American Helicopter Society, Montreal, Canada, April 29–May 1, 2008.

[41] Wenren, Y., Steinhoff, J., and Caradonna, F., "Application of Vorticity Confinement to Rotorcraft Flows," 31st European Rotorcraft Forum, Florence, Italy, September 12–16, 2005.

[42] Wenren, Y., Walter, J., Fan, M., and Steinhoff, J., "Vorticity Confinement and Advanced Rendering to Compute and Visualize Complex Flows," Paper AIAA-2006-945, 44th AIAA Aerospace Sciences Meeting and Exhibit, Reno, NV, January 9–12, 2006.

[43] Steinhoff, J., and Wenren, Y., "An Efficient Vorticity Confinement Based Lifting Surface Method for Rotor Wake Computations," 32nd European Rotorcraft Forum, Maastricht, Netherland, September 12–14, 2006.

[44] Wachspress, D., A., Whitehouse, G., R., Keller, J., D., and Yu, H., "A High Fidelity Brownout Model for Real-Time Flight Simulations and Trainers," 65th Annual Forum Proceedings of the American Helicopter Society, Grapevine, TX, May 27–29, 2009.

[45] Wachspress, D. A., Keller, J. D., Quackenbush, T. R., Whitehouse, G. R., and Yu, K., "High Fidelity Rotor Aerodynamic Module for Real-Time Rotorcraft Flight Simulation," 64th Annual Forum Proceedings of the American Helicopter Society, Montreal, Canada, April 29–May 1, 2008.

[46] Keller, J. D., Whitehouse, G. R., Wachspress, D. A., Teske, M. E., and Quackenbush, T. R., "A Physics-Based Model of Rotorcraft Brownout for Flight Simulation Applications," 62nd Annual Forum Proceedings of the American Helicopter Society International, Phoenix, AZ, May 9–11, 2006.

[47] D'Andrea, A., "Numerical Analysis of Unsteady Vortical Flows Generated by a Rotorcraft Operating on Ground: A First Assessment of Helicopter Brownout," 65th Annual Forum Proceedings of the American Helicopter Society, Grapevine, TX, May 27–29, 2009.

[48] D'Andrea, A., "Unsteady Numerical Simulations of Helicopters and Tiltrotors Operating in Sandy-Desert Environments," Proceedings of the American Helicopter Society Specialists Conference on Aeromechanics, San Francisco, CA, January 20–22, 2010.

[49] D'Andrea, A., "Enhanced Numerical Simulations of Helicopter Landing Maneuvers in Brownout Conditions," 66th Annual Forum Proceedings of the American Helicopter Society, Phoenix, AZ, May 11–13, 2010.

[50] D'Andrea, A., "Development and Application of a Physics-Based Computational Tool to Simulate Helicopter Brownout," Proceedings of the 37th European Rotorcraft Forum, Gallarate (VA), Italy, September 13–15, 2011.

[51] Morales, F., and Squires, K. D., "Numerical Analysis of Unsteady Vortical Flows Generated by a Rotorcraft Operating on Ground: A First Assessment of Helicopter Brownout," Proceedings of the 29th AIAA Applied Aerodynamics Conference, Honolulu, HI, June 27–30, 2011.

[52] Syal, M., "Understanding Brownout Using Dual-Phase Particle Image Velocimetry Measurements," Thesis, University of Maryland, 2011.

[53] Affes, H., and Conlisk, A., T., "Model Rotor Vortex-Airframe Interaction, Part 1: Theory," *AIAA Journal*, Vol. 31, No. 12, December 1993, pp. 2263–2273.

[54] Affes, H., and Conlisk, A., T., "Model Rotor Vortex-Airframe Interaction, Part 2: Comparison with Experiment," *AIAA Journal*, Vol. 31, No. 12, December 1993, pp. 2274–2282.

[55] Bi, Nai-pei, Leishman, J. G., and Crouse, G. L., "Investigation of Rotor Tip Vortex Interactions with a Body," *Journal of Aircraft*, Vol. 30, No. 6, Nov.–Dec. 1993, pp. 879–888.

[56] Brand, A., G., McMahon, H., M., and Komerath, N., M., "Surface Pressure Measurements on a Body Subject to Vortex Wake Interaction," *AIAA Journal*, Vol. 27, No. 5, 1989, pp. 569–574.

[57] Brand, A. G., McMahon, H. M., and Komerath, N. M., "Correlations of Rotor Wake/Airframe Interaction Measurements with Flow Visualization Data," 46th Annual Forum Proceedings of the American Helicopter Society, Washington, D.C., May 21–23, 1990.

[58] Crouse, G. L., Leishman, J. G., and Bi, Nai-pei, "Theoretical and Experimental Study of Unsteady Rotor/Body Aerodynamic Interactions," *Journal of the American Helicopter Society*, Vol. 37, No. 1, January 1992, pp. 55–65.

[59] Ramasamy, M., Johnson, B., and Leishman, J. G., "Understanding the Aerodynamic Efficiency of a Hovering Micro-Rotor," *Journal of American Helicopter Society*, Vol. 53, No. 4, October, 2008, pp. 412–428.

[60] CONCEPT ENGINEERING LTD, *Concept ViCount 180 Smoke System,* 7 Woodlands Business Park, Woodlands Park Avenue, Maidenhead, Berks., SL6 3UA, UK, May 2009.

[61] Dring, R. P., "Sizing Criteria for Laser Anemometry Particles," *Journal of Fluids Engineering*, Vol. 104, No. 1, 1982, pp. 15–17.

[62] TSI INCORPORATED, *Laser Diagnostics: Seed Particles for LDV and PIV,* 500 Cardigan Road, Shoreview, MN 55126 U.S.A., 2006.

[63] Leishman, J. G., "Seed Particle Dynamics in Tip Vortex Flows," *Journal of Aircraft*, Vol. 33, No. 4, 1996, pp. 823–825.

[64] Baharani, A., "Investigation into the Effects of Aeolian Scaling Parameters on Sediment Mobilization below a Hovering Rotor," M.S. Thesis, Department of Aerospace Engineering, University of Maryland, 2011.

[65] Raffel, R., Willert, C., Wereley, S., and Kompenhans, J., *Particle Image Velocimetry: A Practical Guide,* Second Edition, Springer, Berlin, Germany, 2007.

[66] Scarano, F., "Iterative Image Deformation Methods in PIV," *Measurement Science and Technology*, Vol. 13, 2002, pp. R1–R19.

[67] Ramasamy, M., and Leishman, J. G., "Benchmarking PIV with LDV for Rotor Wake Vortex Flows," *AIAA Journal*, Vol. 45, No. 11, November 2007, pp. 2622–2633.

[68] Leishman, J. G., *Principles of Helicopter Aerodynamics 2nd Edition,* Cambridge University Press, New York, NY, 2006, Chapter 3, pp. 139.

[69] Harris, J. R., "Investigation of Relative Importance of Some Error Sources in Particle Image Velocimetry," M.S. Thesis, Department of Mechanical Engineering, Utah State University, Logan, Utah, 2012.

[70] TSI Incorporated, *INSIGHT 3G™Data Acquisition, Analysis, and Display Software Platform Users Guide,* TSI Incorporated, USA, January 2008.

[71] Ramasamy, M., Johnson, B., Huismann, T., and Leishman, J. G., "Digital Particle Image Velocimetry Measurements of Tip Vortex Characteristics Using an Improved Aperiodicity Correction," *Journal of the American Helicopter Society*, Vol. 54, 2009, pp. 1–13.

[72] La Porta, A., "Deceleration of a Particle in a Resisting Fluid with Applications to Biological Physics," University of Maryland, September 2007, http://www2.physics.umd.edu/~alaporta/PHYS171_f12/lectures/ForceOfMotorProtein.pdf, Accessed 1/23/14.